Structure, Magnetic Ordering and Electrochemistry of $Li_{1+x}V_{1-x}O_2$

by

James Michael Gaudet

Submitted in partial fulfillment of the requirements
for the degree of Master of Science

at

Dalhousie University
Halifax, Nova Scotia
February 2011

DALHOUSIE UNIVERSITY

Department of Physics and Atmospheric Science

The undersigned hereby certify that they have read and recommend to the Faculty of Graduate Studies for acceptance a thesis entitled "Structure, Magnetic Ordering and Electrochemistry of $Li_{1+x}V_{1-x}O_2$" by James Michael Gaudet in partial fulfillment of the requirements for the degree of Master of Science.

Dated: 03 February 2011

Supervisor: _____

Readers: _____

_____

_____

Departmental Representative: _____

DALHOUSIE UNIVERSITY

DATE: 03 February 2011

AUTHOR: James Michael Gaudet

TITLE: Structure, Magnetic Ordering and Electrochemistry of $Li_{1+x}V_{1-x}O_2$

DEPARTMENT OR SCHOOL: Department of Physics and Atmospheric Science

DEGREE: MSc CONVOCATION: May YEAR: 2011

_____

Signature of Author

TABLE OF CONTENTS

LIST OF TABLES

LIST OF FIGURES

ABSTRACT

The $R\bar{3}m$ layered transition metal oxide composition series of $Li_{1+x}V_{1-x}O_2$ was synthesized using the solid state synthesis technique. X-ray diffraction was used to determine the dependence of structure on composition and clearly indicated a structural anomaly at x = 0 caused by the unusual magnetic ordering on the triangular lattice of the V^{3+} layer. To prevent magnetic frustration V^{3+} cations undergo orbital ordering and subsequent periodic displacent to form "trimers". The periodicity of this phenomena results in a superlattice structure that can be observed as a faint peak in XRD spectra. The relationship between composition, superlattice peak intensity and lattice parameters was clearly documented for the first time.

$Li/Li_{1+x}V_{1-x}O_2$ cells were made and tested. Recent literature has shown that the transformation to 1T Li_2VO_2 upon lithiation is dependant on a nonzero x (ideally x = 0.07 for maximum capacity) to make a small number of tetrahedrally coordinated Li sites accessible. These sites then act as a trigger for shearing into the 1T phase. The cells described within this work intercalated significant amounts of lithium at a higher potential than the $R\bar{3}m$ to 1T transition, possibly signifying occupation of a large number of the tetrahedral sites.

$LiVO_2$ is known to undergo delithiation even in ambient conditons and this can lead to cationic disorder. Cationic disorder is an inhibitor of anion sheet shearing and this suggests that sample handling could be a cause of the observed electrochemical behaviour. The effects of air and water exposure were investigated.

LIST OF SYMBOLS AND ABBREVIATIONS USED

$R\bar{3}m$	Space Group of Layered $LiVO_2$
P-3m1	Space Group of Layered Li_2VO_2
A-A-A	Stacking Sequence in Layered Crystal Structure
A-B-C	Stacking Sequence in Layered Crystal Structure
1T	Phase of the layered Li_2VO_2 Compound
a	Lattice Parameter or Axis in Hexagonal Representation of $LiVO_2$
c	Lattice Parameter or Axis in Hexagonal Representation of $LiVO_2$
a*	Superlattice Parameter
R	Separation Radius Between Vanadium Cations
R_c	Critical Separation Radius
x	Compositional Variable
y	Compositional Variable
y_c	Critical Value of Compositional Variable
T	Temperature
T_t	Transition Temperature
T_c	Critical Temperature
[Ar]	Closed Shell Electron Configuration Identical to Argon
t_{2g}	Triply Degenerate d-electron Orbital
e_g	Doubly Degenerate d-electron Orbital
a_1	Non Degenerate Symmetric d-electron Orbital
e_π	d-electron Orbital Directed out of Plane
S	Spin
i	Electric Current Due to Either Electrons or Lithium Cations
V	Electric Potential in Volts
K	Kelvin
Å	Angstrom
ppm	Parts Per Million
f	Weighting of Lorentzian Component in Pseudo-Voight Peak Shape
g/cm^3	Density in Grams Per Cubic Centimeter
mAh/g	Gravimetric Capacity in Milliamp Hours Per Gram
mAh/cm^3	Volumetric Capacity in Milliamp Hours per Cubic Centimeter
H_2	Hydrogen Gas
PTFE	Polytetrafluoroethylene Binder Material
Li-PAA	Lithium Polyacrylic Acid Binder Material
PVDF	Polyvinyldiene Fluoride Binder Material
NMP	N-methyl Pyrrolidinone
EC	Ethylene Carbonate
DEC	Diethyl Carbonate
SEI	Surface Electrolyte Interphase
C	Charging Rate of Corresponding to Full Charge in One Hour
CC	Constant Current
CV	Constant Voltage

XRD	X-Ray Diffraction
DSC	Differential Scanning Calorimetry
TGA	Thermogravimetric Analysis
EPR	Electron Paramagnetic Resonance
NMR	Nuclear Magnetic Resonance
XAS	X-Ray Absorption Spectroscopy
TEM	Transmission Electron Microscope
ICP	Inductively Coupled Plasma Spectroscopy

ACKNOWLEDGEMENTS

The following people have provided some *substantial* degree of help in this project. That is not to say that have all contributed a great deal. I merely use the term substantial as a counterpoint to the *insubstantial* support I have also received. I also don't intend to imply that the insubstantial is insignificant. It has the potential to be very influential and motivating when it comes in the form of emotional and moral support. However it is difficult, perhaps impossible, to quantify. And this is what you must do if you wish to establish a threshold to determine who is included and who is excluded. Furthermore, I despise the notion that a person's performance should be dependant on their emotional state. Substantial help comes in the form of a solution or approach to a particular problem. It is based on similar experience, subject matter knowledge, physical insight or a mechanical skill, etc.

These people are listed roughly in order of importance because a systematic approach reduces the probability that someone will be forgotten. However it should not be thought of as a strict ordinal scale of their value as a person, co worker or teacher. It is probable that the list is disordered and/or incomplete but is:

Fu Zhou, Xuemei Zhao, Aaron Smith, Aaron Rowe, Jock Smith, Simon Trussler, Andy George, Tim Hatchard, Jing Li, John Thorne, Vincent Chevrier, Lee Moshurchak, Peng Liao, Andrew Todd, Pierre Ferguson, David Stevens, Ted Monchesky, Andrew van Bommel, Robbie Sanderson, Patrick Bonnick, Xin Xia, Deijun Xiong, Jonathan Franklin, Chris Burns, Mark McArthur, Thomas Marks, Kevin Borgel, Robbie Archibald, Adil Kassam

CHAPTER 1 INTRODUCTION

MOTIVATION

The lithium ion battery as an energy storage device has become ubiquitous among users of portable electronic devices. Their high energy density has made them the battery of choice for laptop computers, cellular phones and other such consumer products. On a smaller scale, they have been widely adopted as a power source for critical electronic components in medical, transport, emergency and military applications where both performance and reliability are paramount. Their utility warrants continuing research into performance and tolerance to adverse conditions.

Recently there has also been tremendous interest in developing Li ion batteries for all-electric and hybrid-electric automobiles. This is motivated by urban pollution as well as uncertainty regarding such things as commodity prices, the effect of human activity on climatological behaviour and geopolitical stability. The challenge of designing batteries for all-electric automobiles to compete against gasoline engines has led to great effort and expenditure directed toward the discovery and patenting of newer materials with ever greater gravimetric capacity, volumetric capacity, rate capability, cycle life and safety characteristics.

While the desire to improve performance is obvious, there is also reason to develop new materials with similar overall performance characteristics. The first is the fact that different applications require different characteristics, or at least rank them differently. This means that the Li ion battery – and Li ion battery material – market is segmented

into niches which may favour different materials. It is also true that different proven compositions and synthesis techniques fluctuate in viability as the costs of their inputs fluctuate. A market with substitutes is more resilient to exogenous shocks. Furthermore, patent law ensures the inventor maintains control over the production of an inventive material. This makes large development costs viable but can lead to the undesirable monopoly situation. The existence of substitutes spurs competition which drives down current prices (relative to the monopoly price) and increases the incentive to bring further innovations to market.

$LiVO_2$ has recently been discovered as a lithium ion battery negative electrode material that promises to offer superior volumetric capacity relative to graphite. The remainder of chapter one will introduce the general operation of the Li ion battery and briefly introduce some commonly studied and utilized negative electrode materials. Chapter two will give a history of research conducted on the material $LiVO_2$. Chapter three will explain experimental methods used in the research described in this thesis. Chapter four will conclude by presenting and discussing the experimental results.

THE LITHIUM ION BATTERY

The lithium ion battery is an energy storage device that operates by taking advantage of the difference in energy required to store a lithium atom in two different materials which are referred to as electrodes (after some preparation) in this context. Figure 1 shows that these materials are connected in two separate and very different ways. They are physically separated by only a very short distance and in this intervening space there

resides a liquid electrolyte which is usually impregnated with a lithium salt. This liquid is necessarily a very poor conductor of electrons but readily accommodates the passage of lithium cations.

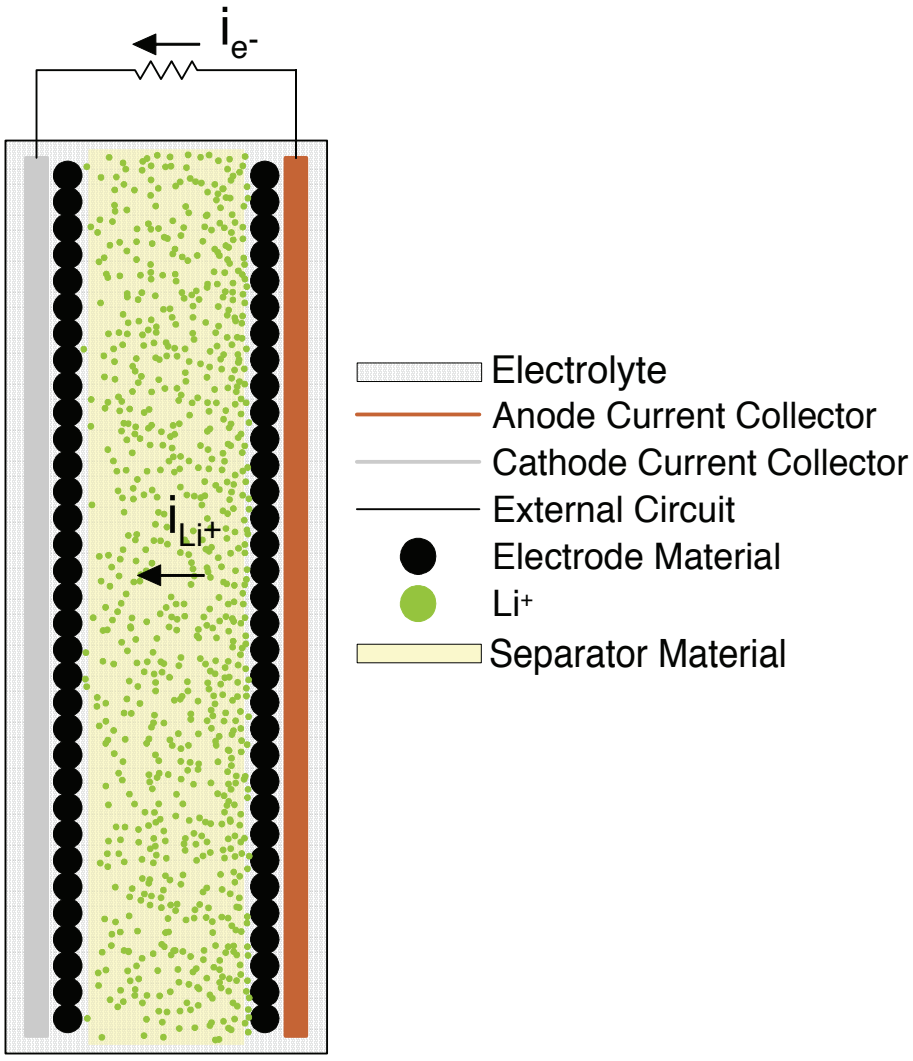

Figure 1
Schematic of a Li ion battery in the state of discharge. Here the thickness of the separator and current collectors has been greatly exaggerated to reveal details of the cells operation. The anions in the electrolyte are not shown.

It is essential that this liquid maintain extensive surface contact with both electrode materials lest some quantity of electrode material become excluded from the storage process. Each electrode is usually comprised of many small particles but the electrode is ensured to be physically contiguous and electrically connected by being prepared in a mixture with a polymeric binder and some conductive constituent, usually a form of carbon. This mixture adheres to a current collector which is usually a metal foil. When the two electrodes are connected through an external circuit, the electrons flow through the external circuit, while the ions are ejected from one electrode material into the electrolyte, which is already rich in Li ions due to the salt. The other electrode depletes the nearby electrolyte of Li ions. This drives the flow of ions between the electrodes. The direction of flow is opposite that of the Li^+ density gradient in the electrolyte. With only one of these transport mechanisms available there would be a buildup of charge and the process would soon stop. As energy density is of prime importance in practical batteries the electrodes are packed together tightly. This necessitates the use of a porous separator material to prevent the electrical contact of the electrodes. It must have sufficient porosity to allow saturation by electrolyte and permit passage of Li^+ cations.

The actual method of lithium storage at each of the electrodes is some form of chemical reaction. Li ion batteries are known as secondary batteries, meaning that though they are a source of energy they must acquire that energy from another source through a process known as charging before they can release it to do work. This latter process is called discharge. A secondary battery is expected to function for many cycles of charge and discharge in its lifetime. This means that the reaction must be reversible in the sense that

the charging and discharging process doesn't alter the nature of the electrode in a manner that precludes future charge and discharge. This often takes the form of a reaction where the Li ions enter the crystal structure of the host without drastically changing it. Intercalation (insertion between layers) is a common realization of this idea. It can also be a displacement, or decomposition, reaction where the basic structure is broken down and reformed on every cycle so long as there is not so much agglomeration or swelling that the material loses electrical or ionic conductivity [1]. Figure 2 shows a diagram of layered graphite with intercalated lithium.

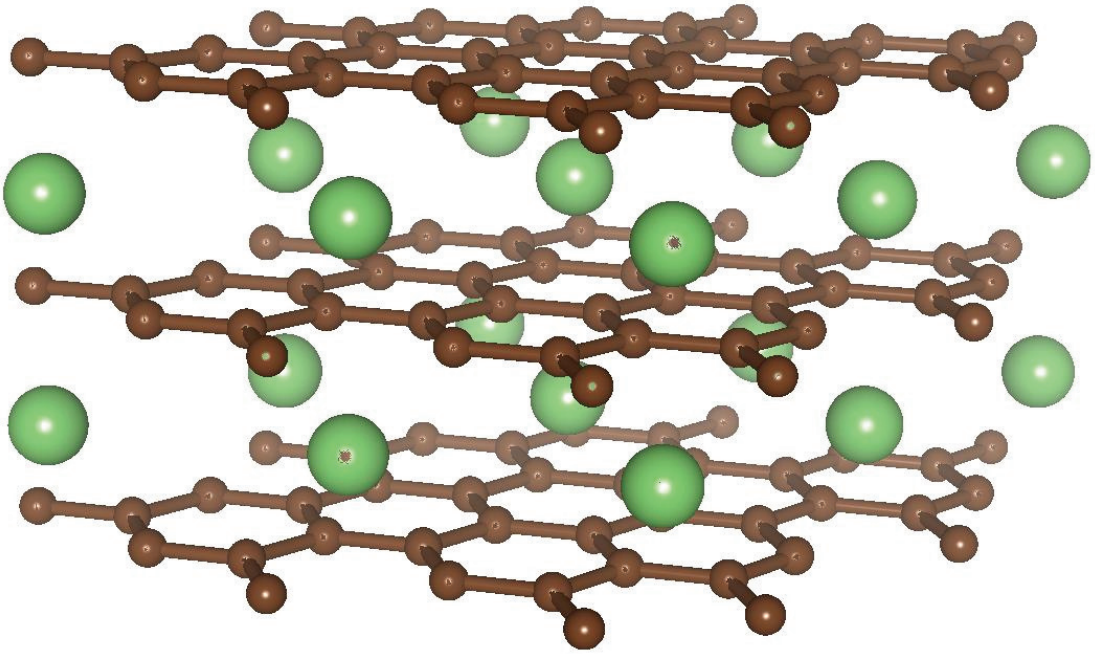

Figure 2
The layered hexagonal structure of LiC_6 is seen here. Lithium (large spheres) intercalate between the layers without significantly altering them. Figure made using VESTA [2].

Li is at different chemical potentials in the two different electrodes materials and the associated energy difference is available to do work through the external circuit. Since

the work done by batteries is electrical, it is often more convenient to speak of potential in Joules per Coulomb, i.e. Volts. During discharge, the electrons and ions flow from the electrode in which they reside in shallower potential wells, known as the anode or negative electrode, to the electrode in which they reside in deeper potential wells, called the cathode or positive electrode. The fact that the electrical connection occurs externally has two advantages. The first being that it can be used to make the cell do work on an external system. The second is that the charge or discharge can be made to commence or cease by closing or opening the electrical connection.

POPULAR NEGATIVE ELECTRODES FOR LITHIUM ION BATTERIES

	Crystalline Density g/cm^3	Theoretical Capacity mAh/g	Achieved Capacity mAh/g	Achieved Volumetric Capacity†† mAh/cm^3	Average Potential V	Volume Change %	Cycles to 80% Capacity
Graphite	2.12 [3]	372 [4]	360 [4]	700	0.2 [4]	10	>1500
$Li_{1.1}V_{0.9}O_2$	4.333 [3]	314 [3]	350 [5]	1200	0.22 [3]	26.8 [3]	unknown
$Sn_{30}Co_{30}C_{40}$	6.5*	701 [6]	497 [6]	1200	0.5 [6]	160**	>100†
Si	2.33 [8]	3579 [9]	3550 [10]	2200	0.4 [10]	280 [9]	>120 [11]
$Li_{4/3}Ti_{5/3}O_4$	3.472 [12]	175 [13]	225 [13]	780	1.6 [12]	nil [13]	>2500 4]

*$(Sn_{50}Co_{50})_{60}C_{40}$ (Figure 4.26 in [6])
**$Sn_{33}Co_{36}C_{31}$ [7]
†after first three cycles [6]
††based on fully lithiated volume

Table 1
Performance characteristics for commonly studied and marketed negative electrode materials.

Table 1 shows some of the relevant characteristics of lithium ion negative electrode materials for five commonly studied and/or marketed materials. Citations are given by

the reported value, material name or footnote. The discrepancy between theoretical and achieved capacity is indicative of how complete the reaction is. This can be related to things such as kinetics and the stability of the lithiated/delithiated state. The average discharge potential is important as it is the difference in electrode potentials along with capacity that determines the energy density that can be delivered upon discharging. Cycle life, the number of times the electrode can undergo the charge/discharge process, determines the longevity and lifecycle cost of any battery system when considered in conjunction with its inherent stability. Cycle life is represented here by the number of cycles that can be achieved before capacity is reduced to 80% of its original value. Volumetric capacity is calculated from the crystalline density and gravimetric capacity. The relative merits of volumetric and gravimetric capacity depend on the application, thus there is scope to strive for materials that optimize one at the expense of the other and vice-versa.

The ubiquitous lithium ion negative electrode material today is graphite [14]. This has a capacity of 360 mAh/g at an average potential of around 0.2 V. The cycle life of graphite has proven exceptionally good. Graphite consists of carbon atoms arrayed in hexagonal sheets. These sheets accommodate the intercalation of Li layers in their intervening spaces (similar to $LiVO_2$) as seen in Figure 2. The locations at which the Li layers form are periodic and the periodicity alters with the amount of intercalated Li, this is called staged intercalation [15]. These properties of graphite along with its low cost make it an extremely common and successful choice; however it is not without problems. Lithiated graphite tends to react with the electrolyte at low voltages such that a certain quantity of

lithium is lost as irreversible capacity to form a passivating solid electrolyte interphase (SEI) [14]. This slows the reaction with the electrolyte. The SEI is coats the graphite surface and, as seen in Table 1, graphite experiences a 10% volume expansion upon intercalation. Thus the SEI is a dynamic thing: expanding, cracking and reforming on a frequent basis. It can thus consume a significant quantity of lithium and electrolyte over the life of the cell. The low voltage of lithium intercalation into graphite implies a certain risk of lithium plating which carries with it safety concerns due to high surface area dendritic Li formation.

Si reacts with Li. This results in a first cycle capacity as large as 3580 mAh/g [9]. This naturally leads to tremendous swelling of the electrode that repeats with every cycle. As this occurs there is fracturing and swelling. The network of conductive carbon particles and polymeric fibres that ensure the electrical connectivity of the system degrades and a large proportion of the material becomes excluded from the reaction. Methods to combat this problem include sputtering thin films [10] and improvement of binder materials [11]. These avenues are either expensive to implement on an industrial scale or remain in their infancy. So, while Si remains the preferred objective in the Li-ion negatives field, it is not yet ready for universal adoption. The reader should take note that, while Table 1 shows that theoretical capacity and excellent capacity retention have been achieved for Si, these values correspond to different synthesis and cell fabrication techniques which may be incompatible or independently infeasible on a large scale. This makes it clear that there is a need for materials which represent an improvement upon graphite but which can be brought to market before Si.

Sn and Sn-transition metal alloys will also alloy with lithium but they have a similar problems to Si [6]. This can be offset by preparing the material with a small particle size in the first place and allowing room for expansion in the surrounding volume. Nanostructured $Sn_{30}Co_{40}C_{40}$ prepared in a carbon matrix achieves this goal but performance is strongly influenced by synthesis technique [6]. Particularly, vacuum sputtered thin films conform to the theoretical capacity of about 700 mAh/g, while those produced by mechanical milling have somewhat less capacity. Despite these difficulties, lithium ion batteries incorporating Sn-Co-C negative electrode materials are currently available commercially.

Another well studied material is $Li_{4/3}Ti_{5/3}O_4$. This material is in many ways closest to $LiVO_2$ due to the fact that they are both transition metal oxides – a class of material more commonly associated with positive electrodes. It differs however in structure. It is defined as a spinel structure where the Li are inserted into a network of tunnels instead of in layers. $Li_{4/3}Ti_{5/3}O_4$ has a high crystalline density and does not suffer from volume change but it has a low capacity, low tap density and a high voltage compared to graphite [12]. Its greatest advantage is the fact that the negligible volume change prevents the occurrence of capacity fade [4]. This allows it to be cycled repeatedly and at a high rate without any cracking or "shrugging off" of the binder and conductive constituent. This material does not consume any lithium in the formation of a SEI. These advantages set $Li_{4/3}Ti_{5/3}O_4$ apart as the preferred material in certain applications where numerous cycles of charge/discharge are expected and physical space constraints do not put bulkier battery

systems at a disadvantage. Currently, some electrical utilities are planning to use $Li_{4/3}Ti_{5/3}O_4$ batteries as a buffer to smooth fluctuations in electricity demand and production.

When looking for an alternative to graphite as a negative electrode material, Si offers an order of magnitude greater gravimetric capacity while Sn-Co-C still offers twice the gravimetric capacity. If volume is the main concern then Sn-Co-C nanocomposites are competitive with Si. These two options are plagued by a problematic degree of swelling upon intercalation: both over 100% compared to 10% in graphite. $Li_{4/3}Ti_{5/3}O_4$ has a gravimetric capacity lower than that of graphite and a comparable volumetric capacity while a higher voltage and low tap density reduces the overall energy density. It has excellent capacity retention compared to graphite. Thus there is a seeming tradeoff between longevity and capacity.

$Li_{1.1}V_{0.9}O_2$ is claimed [16] to have a potential and gravimetric capacity similar to graphite but with a higher density leading to superior volumetric capacity. This volumetric capacity is inferior to Si but equal to that of Sn-Co-C materials and has a much reduced swelling upon intercalation at less than 30%. Thus it represents an intermediate and may be a viable option for improvement on graphite while the cycle life properties of the high capacity Si materials are being improved. Even with significant improvement to Si there may still be a niche for graphite, $Li_{1.1}V_{0.9}O_2$ and Sn-Co-C analogous to applications where $Li_{4/3}Ti_{5/3}O_4$ is preferred to graphite today.

The original purpose of the research presented in this volume on $Li_{1.1}V_{0.9}O_2$ was to explain the features of its voltage curve, the off-stoichiometric composition choice and the effects of including MoO_3 in the synthesis procedure. The first two goals have since been fulfilled by references [5] and [3]. However, unexpected results have led to further insight into the effects of composition and sample history upon structure and electrochemical properties. These insights, presented herein, augment as well as complement those from [5], [3] and others.

CHAPTER 2 BACKGROUND

STRUCTURAL, ELECTRIC, MAGNETIC AND THERMAL PROPERTIES

The paper published by Kobayashi et. al. [17] in 1969 describes the compound $LiVO_2$ with trivalent vanadium cations that is isostructural to $NaFeO_2$. Figure 3 shows several unit cells, each containing three formula units of $LiVO_2$, in hexagonal representation, constructed using powder XRD data.

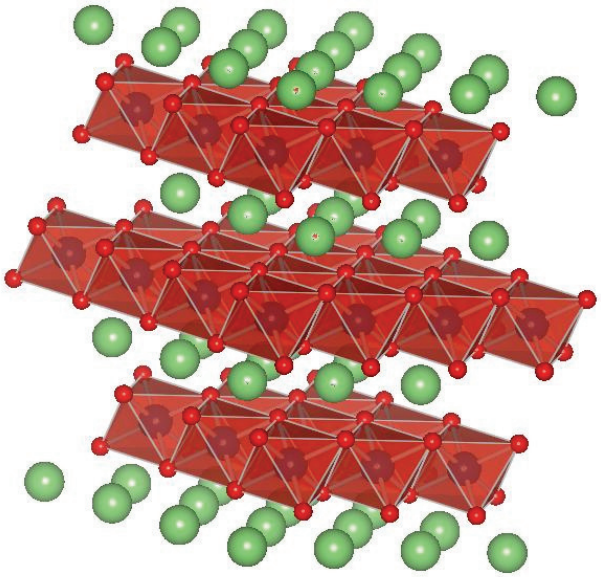

Figure 3
Layered transition metal oxide $LiVO_2$. Oxygen anions (smallest) surround the octahedrally coordinated vanadium cations (medium). The lithium (largest) are shown without octahedra. The "c" axis is perpendicular to the layers [2].

Parallel sheets of oxygen anions are arrayed perpendicular to the "c" axis with alternating layers of Li^+ and V^{3+} cations between them in the A-B-C stacking sequence of the lattice sites of an ordered rock-salt structure along the cubic (111) direction which corresponds

to the “c” axis. Both cations are octahedrally coordinated by the anions and these octahedra are edge-sharing. To emphasize their mobility, Li octahedra are not shown. Figure 4 shows the vanadium layer plane within which the “a” axis points.

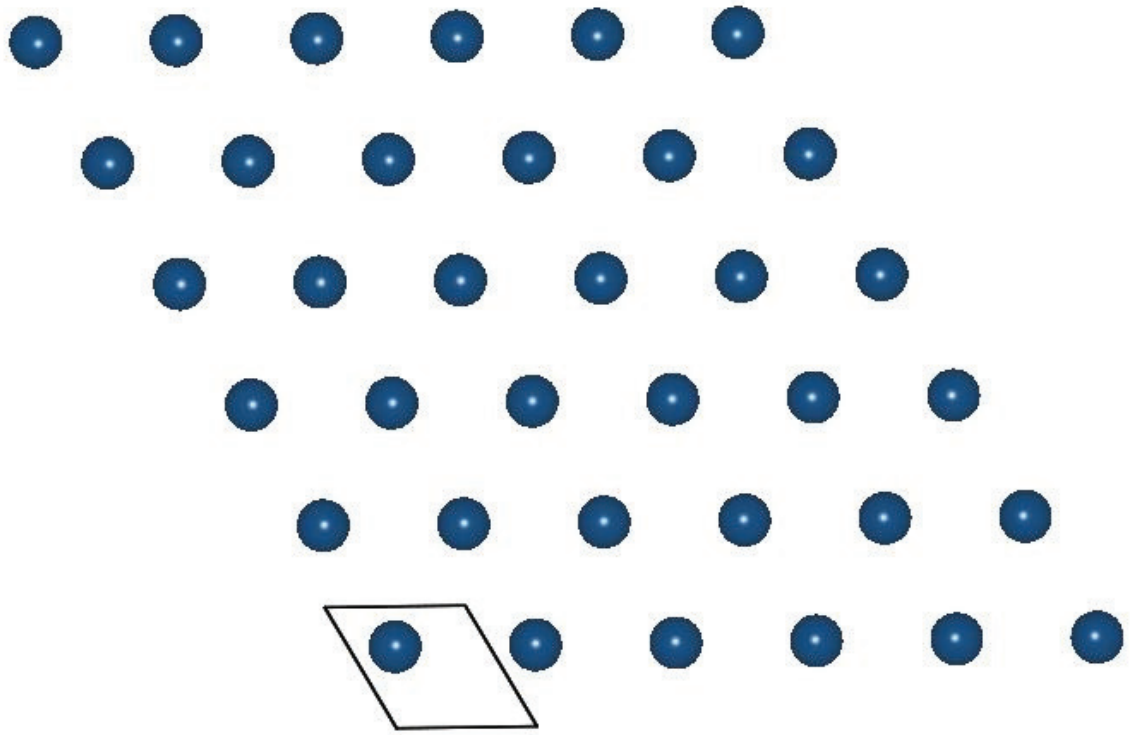

Figure 4
Vanadium plane of $LiVO_2$ observed along the “c” axis (pointing out of the page). As the value of the “a” axis (between atoms, in the page) decreases the spacing between vanadium cations is reduced and overlap between valence orbitals increases. The projection of the unit cell in the plane is seen in the lower left [2].

Kobayashi et al [17]. produced the series of compositions $Li_xV_{2-x}O_2$ with $0.8<x<1.2$ (i.e. $Li_xV_{1-x}O_2$, $-0.2<x<0.2$) and reported no variation in lattice parameters from a = 2.83 Å and c = 14.87 Å. These measurements were repeated over a temperature range from 300K to 600K, and lattice parameters showed a very weak and smooth variation until a discontinuity at $T_t \approx 460K$. Above this temperature a = 2.89 Å and c = 14.48 Å.

Anomalies were also seen at this temperature in differential scanning calorimetry (DSC), magnetic susceptibility and electrical resistivity measurements. DSC revealed an exotherm at about T_t with no discernable composition dependence. Electrical resistivity decreased with increasing temperature, indicating the semiconducting nature of the material, but showed a large jump at T_t. This behaviour was the same for all compositions. Magnetic susceptibility showed a sharp increase on passing through T_t and, when cooled, this transition exhibited hysteresis. The authors explained this transition as driven by clustering of vanadium ions in the plane (Figure 4) of the "a" axis. As the temperature passes through T_t, the cations separate and d orbital overlap decreases. This leads to a reduction in d-electron pairing thus making them more susceptible to paramagnetic effects. The composition dependence of susceptibility is different below and above T_t. Above, there is little d-electron pairing and the susceptibility decreases with increasing x because both the number of vanadium cations and their d-electrons decrease (when Li^+ is substituted for V^{3+}, an additional two V^{3+} must be oxidized to V^{4+}). Below the transition temperature, susceptibility is at a minimum for $x = 0$. This is because the highly ordered structure facilitates d-electron pairing making them unavailable for paramagnetic behaviour. When x deviates from 0 there is mixing of the cations as one invades the other layer and some vanadium atoms become isolated from other vanadium atoms by Li^+ cations. One can easily imagine this by replacing some of the V in Figure 4 with Li. This inhibits d orbital overlap and makes these orbitals available for paramagnetism.

In 1985 Hewston and Chamberland reported [18] the production of single crystals and powders of $LiVO_2$. Structural X-ray studies essentially confirmed earlier reports. The one difference was the detection, in single crystal samples, of a superlattice in the plane of the "a" parameter. DSC of the powder samples indicated heats of transition that were between six and 12 times larger than those reported in [17] while the oxidation of $LiVO_2$ to $LiVO_3$ during thermogravimetric analysis (TGA) suggested the presence of the V^{4+} ion corresponding to an initial composition of Li_xVO_2 with $0.6<x<0.7$. This estimate of composition is later supported [19] by electron paramagnetic resonance (EPR). Further DSC studies [19] suggested that the transition is dependant on heating rate. Decreasing the rate by an order of magnitude made it barely detectable. Infrared absorption spectra were collected over a range of temperatures and seemed to indicate covalent bonding at low temperature by the presence of two large absorption peaks at 715 and 605 inverse cm, which disappeared above the transition temperature. Powder XRD on $LiVO_2$ at various temperatures revealed [20] a superlattice peak just below a scattering angle of 21° that decreases in integrated intensity as the temperature is increased and disappears above the transition temperature. Only solid state solutions in the $LiCr_yV_{1-y}O_2$ series with y = 0.0, 0.1 and 0.2 yielded a single phase product [21]. Interestingly, the volume of the unit cell increased when y, the proportion of Cr^{3+} cations, increased despite the smaller predicted radius for Cr^{3+} cations relative to V^{3+}.

An independent attempt to produce single crystals of $LiVO_2$ was made [22] by Takei et al. Their results yielded hexagonal platelets of a composition around $Li_{0.8}VO_2$. XRD studies again suggested a superlattice with dimension $a^* = \sqrt{3}a = 4.92$ Å. This work also

reported resistivity measurements along both “a” and “c” axes. Resistivity values were an order of magnitude higher along the “c” axis and temperature dependant behaviour suggested a variable range hopping mechanism at low temperatures. It has been shown [23] that cationic disorder in $LiVO_2$ contributes to this form of resistivity and one expects $Li_{0.8}VO_2$ to be disordered since 1/5 of the Li cations are missing relative to the stoichiometric composition. However, single crystals of $LiVO_2$ that are near stoichiometric also show this electrical behaviour, at least in the "a" plane [24]. Reference [24] showed electron micrograph pictures of $LiVO_2$ single crystals. These samples were extremely cracked. The authors proposed that this occurs during cooling after sample synthesis when the temperature passes through T_t and the lattice parameters change. In light of this possibility, it may be important to consider what effects could result from repeated lithium insertion/removal.

CRITICAL SEPARATION RADIUS

In a 1960 paper Goodenough proposed a model [25] of direct cation - cation interaction in octahedrally coordinated transition metal oxides to explain the great variety of electrical and magnetic properties they can exhibit. This mechanism was in contrast to a previously established cation-anion-cation interaction (superexchange). Figure 5 shows two edge sharing V octahedra from $LiVO_2$. The cation-cation interaction is expected where unpaired d-electrons overlap through shared faces or edges of adjacent octahedra, whereas the latter is associated with cation-anion-cation angles of 180 or 135 degrees.

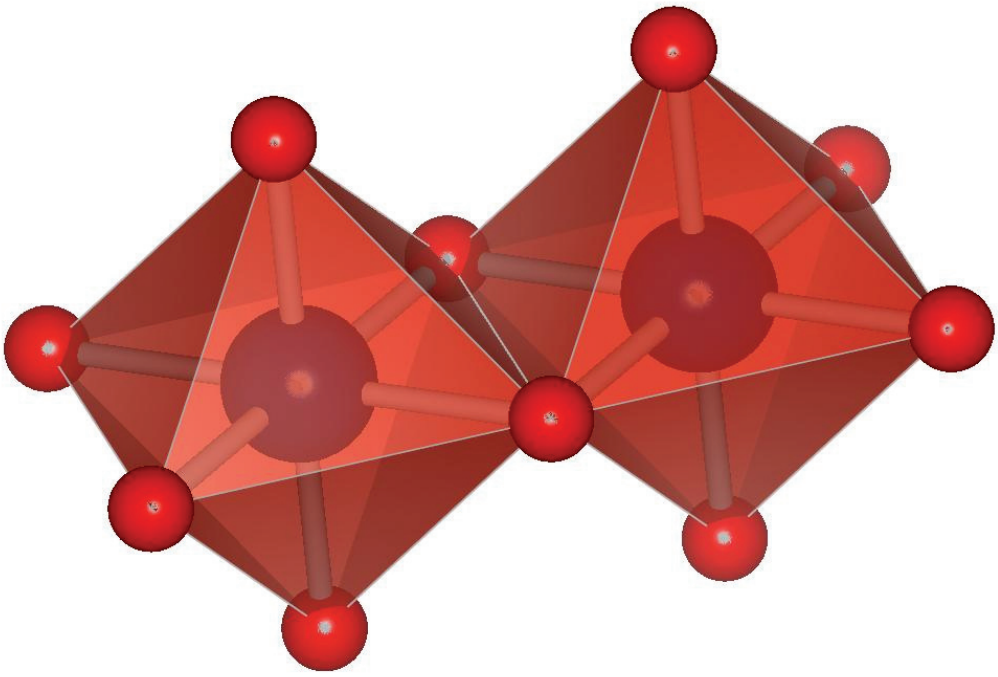

Figure 5

Two vanadium atoms in edge-sharing octahedral coordination from $R\bar{3}m$ $LiVO_2$ [2].

The d-orbitals fall into two categories. Three are triply degenerate t_{2g} orbitals which are directed towards the neighbouring vanadium cations, the other two are doubly degenerate e_g orbitals which are directed towards the oxygen anions and thus filled after the t_{2g} orbitals. The cation-cation interactions are classified as either weak or strong depending on the degree of overlap between orbitals. Weak cation-cation interactions yield semiconducting or insulating behaviour and are antiferromagnetic if there are three or fewer d-electrons. If there are more than three electrons and the t_{2g} levels maintain their degeneracy, the material will exhibit low temperature ferromagnetism. Compounds with strong cation-cation interaction show completely different behaviour depending on the occupancy of the d-orbitals and whether the t_{2g} orbitals (which tend to overlap whereas

the e_g orbitals don't) maintain their degeneracy. As electrons are subject to the exclusion principle the tendency is for the interaction between overlapping orbitals to be antiferromagnetic. This is feasible if there are three or fewer d electrons occupying t_{2g} orbitals. In this case the cations will pair up into a covalent-type bond with a total spin of S=0 for each pair. Thus the susceptibility will be determined by Pauli paramagnetism (or that of isolated cations at high T). If there are four or five d-electrons, the e_g orbitals will fill and can interact with each other ferromagnetically, unless the degeneracy of the t_{2g} orbitals is lifted through bonding.

Goodenough applied [26] this model to $LiVO_2$ based on early literature not covered in this review. As V^{3+} ions in $LiVO_2$ have two valence d-electrons each and share edges, we expect an antiferromagnetic cation-cation interaction. The susceptibility data, with its sudden jump at T_t, suggests the formation of S = 0 metallic "molecules" below T_t and paramagnetic behaviour of individual V^{3+} ions above. It is also suggested at this point that such bonding occurs in a triangular fashion which appears to make it unique among materials described by this theory. Reference [26] also introduces the notion of a critical separation radius, R_c, between interacting cations. For $R>R_c$ the valence electrons of the interacting cations behave in a localized manner whereas when $R< R_c$ collective electron behaviour becomes dominant. It is noted that $R< R_c$ if $T< T_t$, while it is not clear what transpires if $T> T_t$.

Hewston and Chamberland extend upon this idea by proposing [19] that the transition seen at T_t is due to a semiconducting to metallic transition driven by a change in the V^{3+}

plane bonding. They envisioned a low temperature phase with a single covalent bond of infinite extent (within two dimensions) and delocalized electrons that cause a contraction within the plane of the "a" lattice parameter. This arrangement is consistent with a cation-cation separation distance less than Goodenough's R_c. The high temperature phase is metallic and has an expanded "a" lattice parameter. The metallicity of this phase is consistent with conductivity [17,19] as well as spectroscopic data [19], but is inconsistent with the model put forth in [25] where localized (insulating) electron behaviour appears outside the $R< R_c$ (covalent bonding) region. This could perhaps be accounted for if $R\approx R_c$ above T_t as Hewston and Chamberland state that a narrowband metallic state is possible in the vicinity of this point. The authors also propose that the transition at T_t is noncoopertive and independent of the Li content (thus independent of the relative abundance of V^{3+} and V^{4+}). This last point is justified by the claim that R_c is equal for the two vanadium cations. Later, the authors seem to go further and say [21] "the driving force for the transition is a critical distance phenomenon involving a change in the V^{3+}-V^{3+} bond type from covalent to metallic". While the existence of the low temperature phase was always mentioned in relation to the critical radius of Goodenough, this statement seems to suggest for the first time that the transition is a consequence of changing inter-cation radius despite the fact that the $R> R_c$ phase is expected to have lower conductivity.

Goodenough et al. later described [27] the vanadium ion clusters observed below T_t as trimers held together by valence d-electrons in molecular orbitals. The crystal field lifts the t_{2g} degeneracy and forms an empty a_1 orbital and two e_π orbitals which are directed

towards neighbouring V^{3+} cations. Figure 6 shows how the cations involved in this trimer formation are drawn towards the centre of the bond and thus are displaced from their original location.

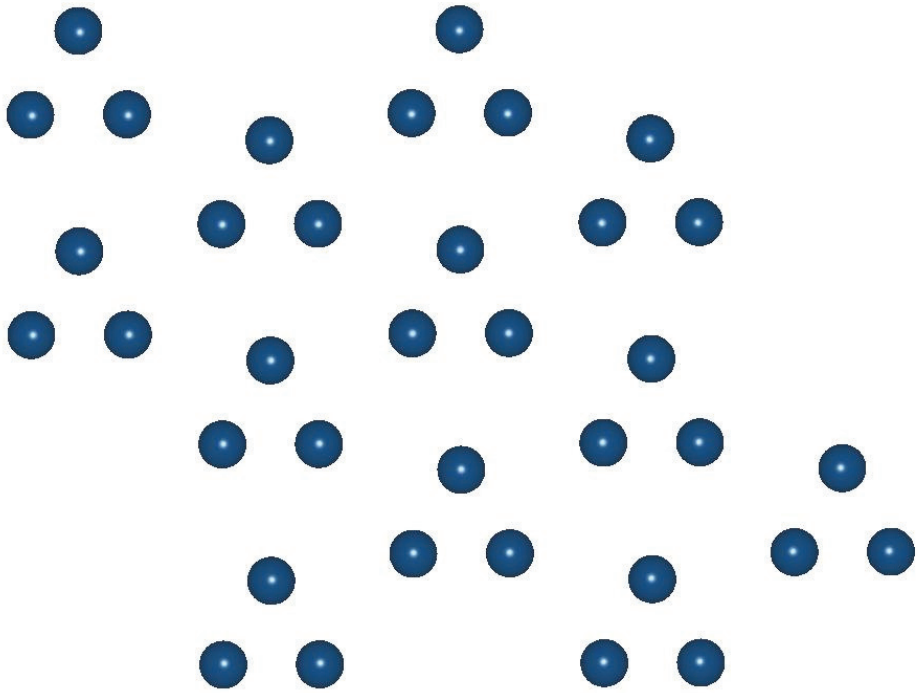

Figure 6
Intercationic interactions cause displacement of vanadium cations into trimer configuration [2]. Due to this displacement the cation-cation interaction is much stronger within trimers than between.

Within a trimer $R < R_c$ whereas between trimers $R > R_c$. This would account for the lower conductivity in the low temperature phase while still allowing strong cation-cation bonding. The intercationic separation in the high temperature phase is described as $R \leq R_c$ rather than $R > R_c$. This paper postulates that the dimensions of $LiVO_2$ are such that $R \approx R_c$ and the resulting trimer formation represents instability in a system that cannot decide if $R < R_c$ or $R > R_c$. In an attempt to determine the value of R_c, the series of

compositions $LiCr_yV_{1-y}O_2$ was attempted by Goodenough et. al. This was achieved, despite enormous difficulty to obtain a single phase sample for y = 0.3. For interactions between Cr cations in $LiCrO_2$, $R > R_c$, and this holds true for V-Cr interactions in the $LiCr_yV_{1-y}O_2$ series. Thus as y is increased there is a decrease in trimer formation and also a decrease in T_t. The latter was borne out by DSC data. Lattice parameters were presented over the composition range for $T < T_t$ and $T > T_t$. For $y > 0.3$ there was little difference between high and low temperature data. The "a" axis remained constant with composition while the "c" axis and volume decreased slightly as Cr^{3+} has a smaller radius than V^{3+}. This was consistent with Vegard's law. For $y < 0.3$ there was a tremendous difference between the high and low temperature data. The "a" axis dimension increased rapidly with increasing y below T_t but slowly decreased above. This caused them to converge at $y = y_c \approx 0.25$ and this convergence can be thought of as a lowering of T_t to room temperature at $y \approx 0.25$.

The difference between high and low temperature "a" parameter was described as due to a combination of molecular orbital formation and volume discontinuity at the transition temperature. The unit cell volume increased rapidly below T_t and decreased rapidly above, for both phenomena at rates larger than those attributed to Vegard's law and at higher values of y. These converged at $y = y_c \approx 0.25$ in the same manner as "a". The high temperature volume, however, shows a sharp jump at about y = 0.3. The temperature is too high for trimer formation anywhere in the composition range and this discontinuity is claimed as evidence of a first order transition between $R < R_c$ and $R > R_c$ phases (not to be confused with the transition associated with crossing T_t where $R < R_c$ on both sides).

The particular difficulty of forming the y = 0.3 sample is also purported as evidence of this claim as was a discontinuous drop in the transition temperature at $y \approx 0.25$. It is important to understand that the authors' explanation of the $LiCr_yV_{1-y}O_2$ system hinges on the variation of R_c with y due to electronic properties rather than changes in R directly related to structure. Figure 7 illustrates this schematically in the T-y phase diagram.

For y = 0.0, $R < R_c$ at both high and low temperature. Increasing y causes R_c to drop until it crosses R (which drops at a slower rate) at $y \approx 0.25$. At the same time, T_t decreases with y approaching room temperature close to y = 0.2 and vanishing at $y \approx 0.25$ since $R > R_c$ at that point. As the y > 0.3 lattice parameters represent $R > R_c$ behaviour in a series where R_c varies with y and, furthermore, the parameters appear to conform to Vegard's law, the authors extrapolated to determine an $R > R_c$ value of 2.905 Å for $LiVO_2$. Since the actual ($R < R_c$) value for $LiVO_2$ is 2.89 Å, the authors conclude: R_c =2.90 +/- 0.01Å for the interaction between octahedrally coordinated, edge sharing V^{3+}-V^{3+} pairs with six like neighbors in an oxide.

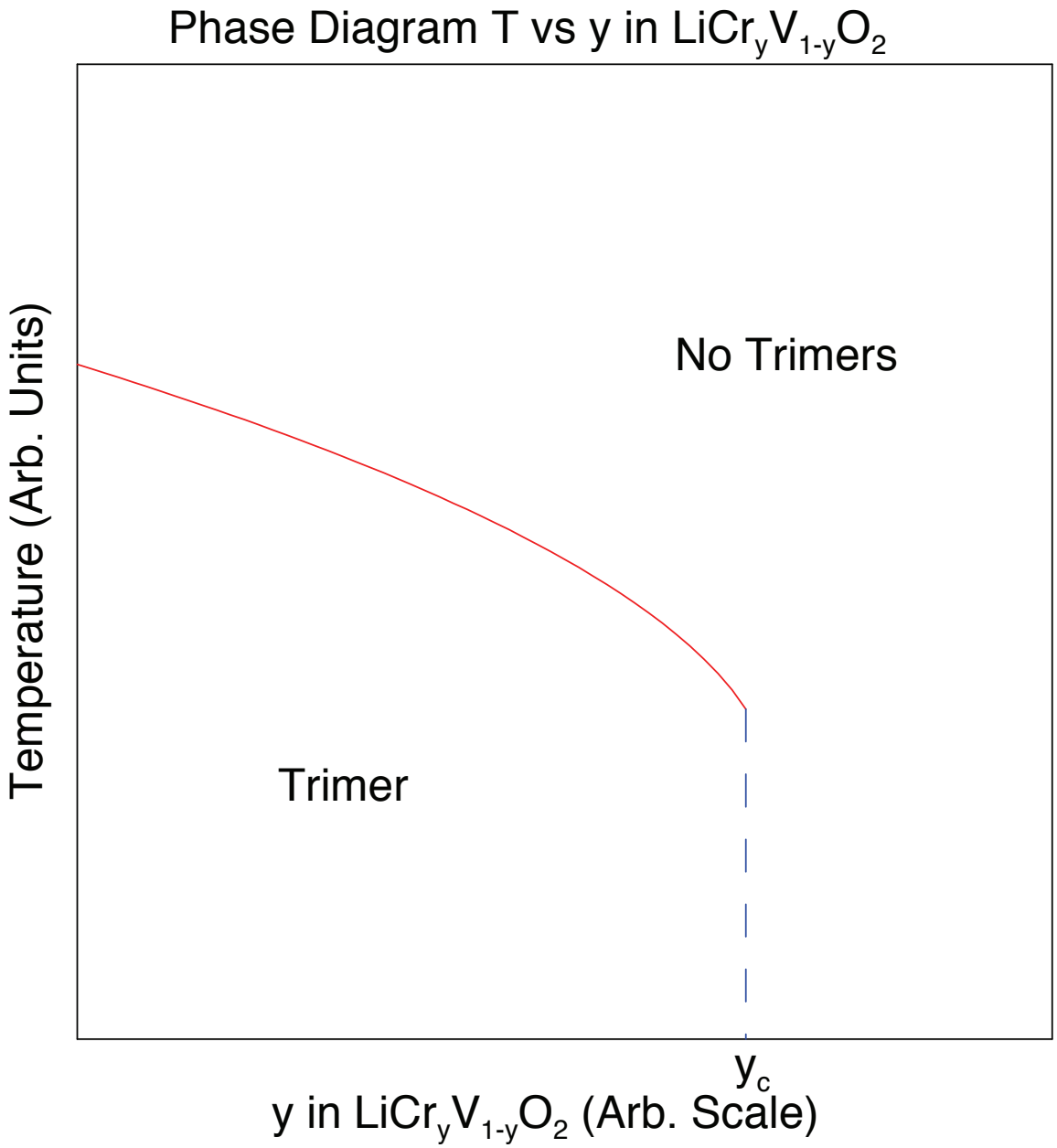

Figure 7
Representative phase diagram for $LiCr_yV_{1-y}O_2$ showing the presence or lack of trimer formation for T and y. The solid line represents the temperature driven transition. The dashed line represents the composition driven transition at critical $y = y_c$. Note that in Goodenough's model it is R_c that changes with y while R is relatively constant. The composition at which $R = R_c$ is denoted by y_c.

The explanation given in reference [27] seems to reconcile the problems associated with Hewston and Chamberland's explanation of the phase transition in $LiVO_2$ based on references [25, 26] and explains the potential effect of a critical separation radius, R_c, but it cannot fully account for the transition at T_t in $LiVO_2$ as $R < R_c$ on both sides of the transition. It seems this phenomenon is determined by temperature through some other property than lattice parameter. Above R_c (associated with $y > 0.25$ in the $LiCr_yV_{1-y}O_2$ system) there is behaviour associated with a localized electron model and no chance of trimer formation. As Cr^{3+} content decreases (move left in Figure 7), the difference in electronic nature of $LiVO_2$ and $LiCrO_2$ causes R_c to increase. As the two compounds are very similar, structurally, R remains constant. When R_c increases past the value of R (as V^{3+} is added at the expense of Cr^{3+}, such that y becomes less than y_c) the system will adopt one of two possible electronic states (above or below the solid line in Figure 7) depending on it's temperature relative to T_t. The discontinuity in volume between the $R_c < R$ state and the $R_c > R$ state suggests a first order phase change. It seems that the critical radius determines in which situations ($R > R_c$) trimer formation cannot occur. However when $R < R_c$ it is not immediately clear why there exists a transition at T_t. If the critical radius does exist it is not the full story behind trimer formation.

A nuclear magnetic resonance (NMR) study [28] on low temperature $LiVO_2$ confirmed that there is no contribution to magnetic susceptibility from $S = 1$ V^{3+} cations. It also found that the Li^+ sites had high symmetry in contrast to the V^{3+}. Further NMR and XRD studies [29, 30] by another group noted a large quadrupole moment at the site of vanadium nuclei. As the quadrupole moment is the result of an electric field gradient at

the nucleus [31], this gives evidence of some sort of preferential bonding between some of the V^{3+} cations, such as trimer formation. Reference [30] found that the V^{3+} atomic positions were displaced by about 0.1 Å in the trimerized lattice of Figure 6 (another reference [32] put the value at 0.160 Å) and showed that this structure was unstable relative to the high temperature, untrimerized, structure. This suggests the idea of trimerization as a trade off between lattice and magnetic energy. The authors also gave voice to the idea that in the low temperature phase there can be magnetic excitations above the S=0 ground state. This was also observed experimentally in [33].

A study [34] was conducted on $Li_{1-x}Mg_xVO_2$ and found similar results to [27]. Unfortunately, x was limited to $x \leq 0.10$ so it may not be informative as it otherwise could have been. Mg cations are in the 2+ oxidation state so this composition series contains 1-x V^{3+} as well as x V^{2+} cations. V^{2+} has the same number of d-electrons as Cr^{3+} so may exhibit the same bonding and have an R_c value small as that of Cr^{3+}. The "a" lattice parameter and low temperature susceptibility increased with increasing x while the "c" lattice parameter, T_t and magnitude of the superlattice peak all decreased. This was interpreted as being due to the presence of S = 1/2 trimers which suggests the authors believed the V^{2+} bonding behaviour to be similar to that of V^{3+} as opposed to that of Cr^{3+}.

ORBITAL ORDERING

In 1997 Pen et. al. proposed and performed calculations for a model of orbital ordering in two dimensional magnetic systems [35]. The model seems designed to explain trimer formation in $LiVO_2$, for it describes a triangular lattice of cations with two d electrons. In

contrast to the notion that the trigonal crystal field raises the threefold degeneracy of the t_{2g} [27], orbitals it is proposed that the degeneracy remains and causes the potential for magnetic frustration in the ground state. To obviate this frustration the orbitals become ordered in the low temperature phase. Figure 8 shows one of the orbital ordering patterns for which calculations were performed using both ferromagnetic and antiferromagnetic interactions. It shows the familiar trimer pattern embellished with d-orbitals. The other was a crosshatched pattern of infinite orbital chains. It was found that both patterns had the same energy with the antiferromagnetic interaction. However it was suggested that the trimer model can lower its energy even further through d-d orbital hybridization and, more importantly, this is what is observed in experiment.

These interactions between the orbitals are all in plane in contrast to the e_π bonding suggested in [27]. To test their explanation this group performed [36] x-ray absorption spectroscopy (XAS) on $LiVO_2$ at various temperatures above and below T_t. Spectra were captured on the V 2p and O 1s bands. Results showed that there was very little difference between vanadium d-electrons above and below T_t and thus no change in bonding. In both these situations the d-electrons are localized and do not participate in molecular orbital formation. The O 1s spectra indicated that O 2p/V 3d hybridization was minimal and did not change upon passing through T_t. While the latter observation concurs with the critical separation model of trimer formation, the former certainly does not. References [25, 26, 27] state that trimer formation requires the onset of d electron delocalization and molecular orbital formation.

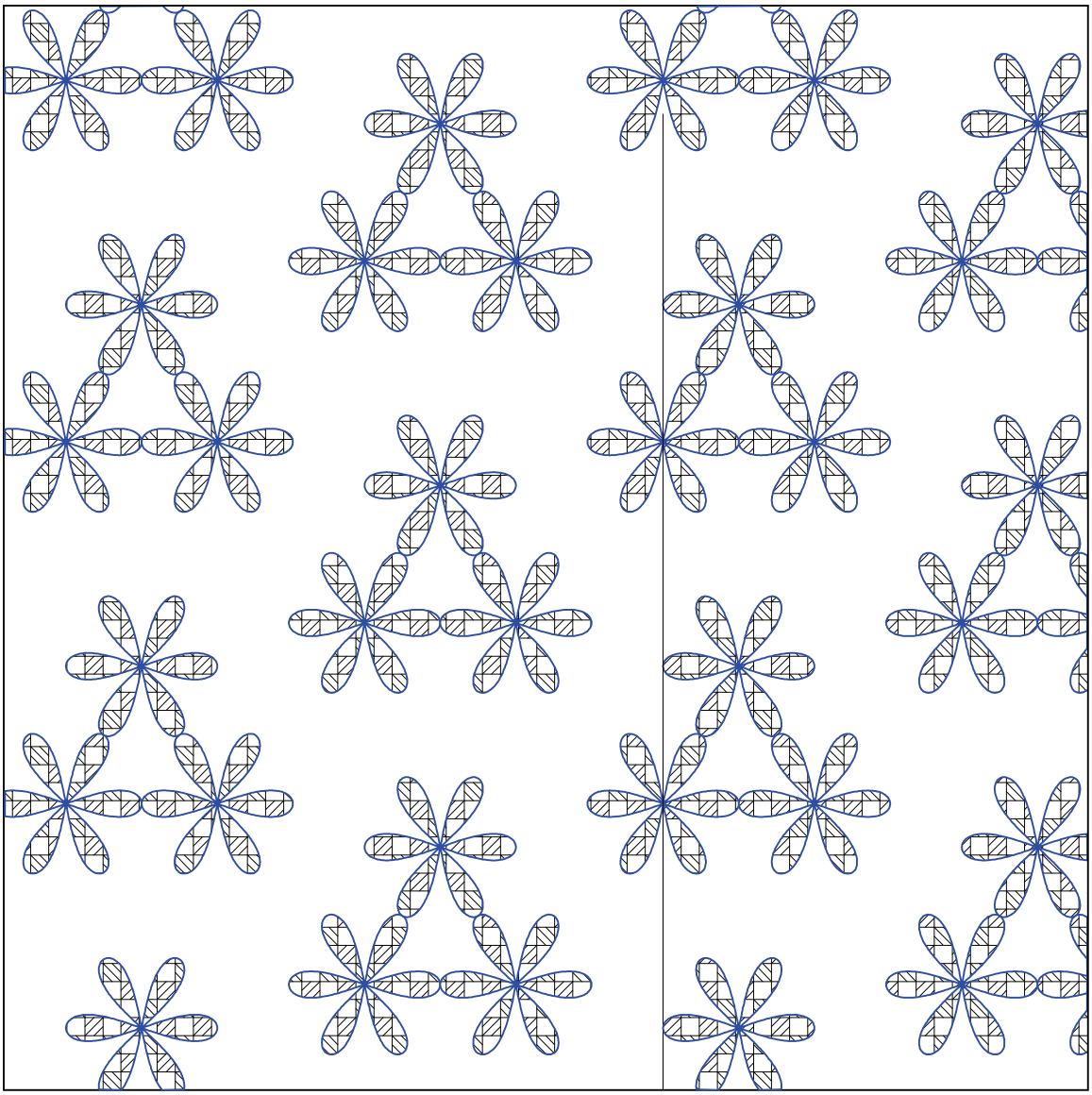

Figure 8
Ordering of t_{2g} orbitals in the V-layer of $LiVO_2$. Only lobes located in the plane of the V-layer are shown. Orbitals that are directed toward each other interact antiferromagnetically. Those not in contact are unoccupied. Occupied orbitals directed toward other trimers are out of range of the interaction.

In this view of things T_t is the temperature at which magnetic order is overcome by magnetic fluctuations and does not instigate a transition through thermal expansion of lattice parameters. Now the first order transition through T_t that was not explained in [27]

is accounted for. The two models, in some sense, complement each other with orbital ordering explaining the transition at T_t and that presented in [27] possibly accounting for the transition at y_c. These transitions are represented as solid and dashed lines in Figure 7. The orbital ordering model, since it is dependant on the V^{3+} oxidation state, should also predict a reduction in trimer formation with Cr^{3+} substitution. The value for which Cr^{3+}, with it's $[Ar]3d^3$ electronic configuration, suppresses all trimer formation could be anywhere from $y = 0.33$ if the Cr^{3+} cations repel each other strongly to $y = 1.0$ if they show a strong tendency to cluster. The fact that lattice parameters coincide for $y \geq 0.25 \approx 1/3$ suggests that orbital ordering can account for the $LiCr_yV_{1-y}O_2$ system.

$Li_{1-x}VO_2$ STRUCTURE AND ELECTROCHEMICAL STUDIES

During the 1980s much work was done on the effects of chemical extraction of Li from the $LiVO_2$ system. It was found [39] that $Li_{1-x}VO_2$ maintained its VO_2 sublattice for delithiation up to $x = 0.3$. Further extraction between $0.33 < x < 0.85$ led to a disordered rocksalt structure as V^{4+} cations migrated to the Li^+ layer. This was observed primarily through a decrease in intensity of the 003 peak during x-ray analysis. The highly delithiated structure contained about 0.66 V in the V layer and about 0.33 of each of Li and V in the Li layer. The diffusion of V from their initial layer to the Li layer appears to happen on a longer time scale than the removal of Li from the structure. This causes the appearance of a two phase substance for $0.33 < x < 0.85$, though another contributor to this may be preferential delithiation of small particles. Figure 9 shows how V^{4+} cations must first pass through a connecting tetrahedral site to enter the octahedral sites of the Li layer.

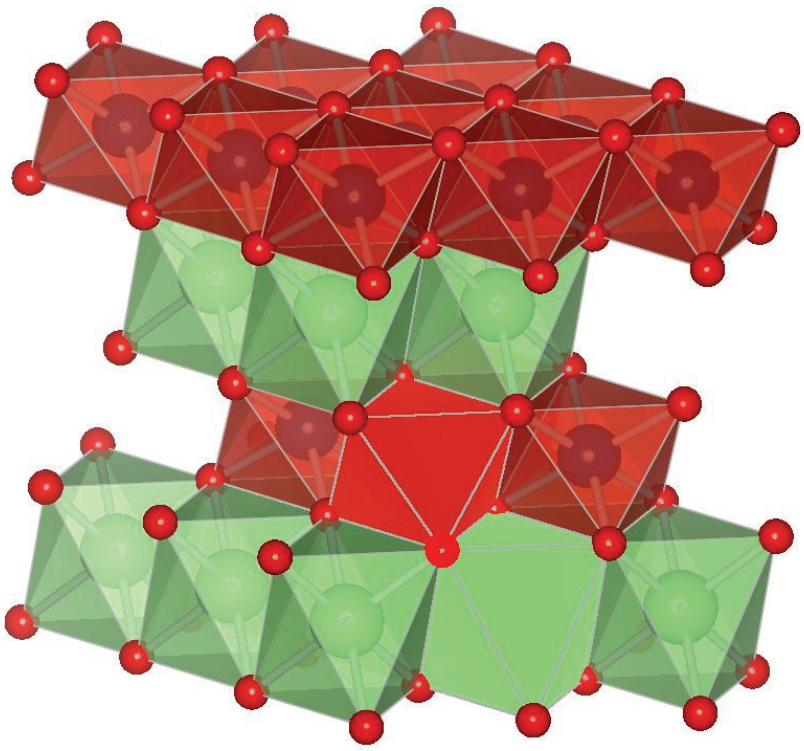

Figure 9

$LiVO_2$ $R\bar{3}m$ structure shown with all Li (light green) and V (dark red) octahedra. An example of a Li-layer tetrahedral site can be seen in the hollow above the highlighted V octahedron between two Li octahedra. An example of a V-layer octahedron is seen to its right above the highlighted Li octahedron. Figure made using VESTA [2].

It is believed that the Li deficient compositions of $x > 0.33$ allow for a significant probability of a tetrahedral site with three adjacent unoccupied octahedral Li sites. It is feasible for such a location to be occupied by the vanadium cation on its passage to the Li layer. It may be favourable for the vanadium cation to further oxidize to V^{5+} while entering the tetrahedral site, temporarily leaving that electron with another V^{4+} until it reaches the other side.

It was noted that the delithiated structure approaches that of a disordered rocksalt. If the composition $Li_{0.5}VO_2$ is prepared and heated to 523 K it is seen to form a closely related

cubic spinel structure [37, 38]. Further investigation [39] into the spinel structure found that lithium could be both extracted from and inserted into it. In fact, enough lithium could be inserted to regain the stoichiometry of $LiVO_2$ but the structure was disordered rocksalt, not the ordered form seen in $LiVO_2$.

X-ray diffraction was used to determine the location of vanadium in layered $Li_{1-x}VO_2$. However, as this technique is not sensitive to Li, studies relied on assumptions to fit the data. The lack of information on where the Li are located was corrected in 1987 with neutron diffraction [40]. It was discovered that the Li^+ did not enter the V layer although the study did not exclude the possibility that they entered tetrahedrally coordinated sites in the Li-layer. It was also revealed at this time that delithiation had the effect of reducing $Li_{1-x}VO_2$ particle size. An electrochemical cell was made using $LiVO_2$ and it was found that Li could be reversibly delithiated to a potential of 2.88 V vs. metallic Li [41]. Further charging of the cell was irreversible. This occurred around 3.09 V.

It was found that the mobility of Li in $LiVO_2$ is sufficient that lithium tended to be extracted by and reacted with air. This was observed [42] in several effects. $LiVO_2$ ground for 10 minutes had an increased weight of about 1%. Samples left in air for three days had a decreased "c" lattice parameter corresponding to $Li_{1-x}VO_2$ and an average V oxidation state of 3.25. These samples also yielded DSC curves identical to delithiated samples of $LiVO_2$. If these samples were heated in dry H_2 they lost about 5% of their weight and reverted to the V oxidation state and crystal structure of stoichiometric $LiVO_2$. Finally, when immersed in water $LiVO_2$ lost about 0.2 Li. Reference [42] pointed

out that the studies conducted by Hewston and Chamberland [18-21] involved washing their samples in acid prior to characterization. This likely guaranteed a composition of $Li_{0.67}VO_2$. Upon heating, this would form $LiVO_2$ and LiV_2O_4 spinel. Hewston and Chamberland reported a first cycle transition temperature that was different from subsequent cycles when a sample was cycled repeatedly through the transition temperature T_t during DSC, susceptibility measurements, etc. The first transition temperature corresponds to the formation of stoichiometric $LiVO_2$ and LiV_2O_4. Reference [42] performed DSC on various members of the $Li_{1-x}VO_2$ series and confirmed this. Interestingly, it was found that the first cycle T_t increases with x in the limited range $x \leq 0.1$.

$LiVO_2$ BATTERIES

Ozawa et. al. attempted [43, 44] production of polycrystalline $LiVO_2$ powder using two different synthesis techniques. With solid state synthesis they were able to attain the composition $Li_{0.96}VO_2$ in an ordered rocksalt structure. This is essentially the process used in all papers considered in this review. A second sample was produced in solution using a hydrothermal method. Transmission electron microscopy (TEM) indicated that both sample powders had a grain size of about 200 nm. The hydrothermal powder was reported as having the composition $Li_{0.86}V_{0.8}O_2$ through inductively coupled plasma (ICP) spectroscopy.

This unusual composition would be expected to have an average vanadium oxidation state of 3.925. Weight gain during TGA stated in reference [43] is consistent with the

oxidation of the vanadium in this sample from an average of 3.925 to V^{5+}. Rietveld refinement of $Li_{0.86}V_{0.8}O_2$ also confirms the composition. Thus, strange as it seems, the evidence is consistent with the claimed stoichiometry. The XRD appears similar to that of stoichiometric, layered $LiVO_2$ with the obvious exception of a much diminished 003 peak, as well as others representing lattice plane separations in the "c" direction, indicating cationic disorder between the layers. This took the form of up to 0.33 vanadium cations being present in the Li layer similar to samples of chemically or electrochemically delithiated $LiVO_2$ seen in [37, 41, and 42]. In the latter case, however, it was shown [40] with neutron diffraction that there was no Li occupancy in the octahedral sites of the V layer while Rietveld refinement on XRD of $Li_{0.86}V_{0.8}O_2$ suggested that one layer was occupied 0.36/0.56/0.08 by V/Li/vacancy and the other 0.44/0.30/0.26. It is odd to have a layered oxide of this type with an imbalance in the number of cations and anions. It has already been established [37] that $LiVO_2$ can lose up to ≈0.33 Li without destabilizing the structure but any further loss will permanently damage it, causing vanadium cation migration in stoichiometric $LiVO_2$ (see Figure 3). This is approximately the number of vacancies present in the hydrothermal sample.

Figure 10 shows how $LiVO_2$ was delithiated to form $Li_{1-x}VO_2$ in an electrochemical cell. A flat plateau was seen at ≈ 3V from x = 0 to x = 0.33.

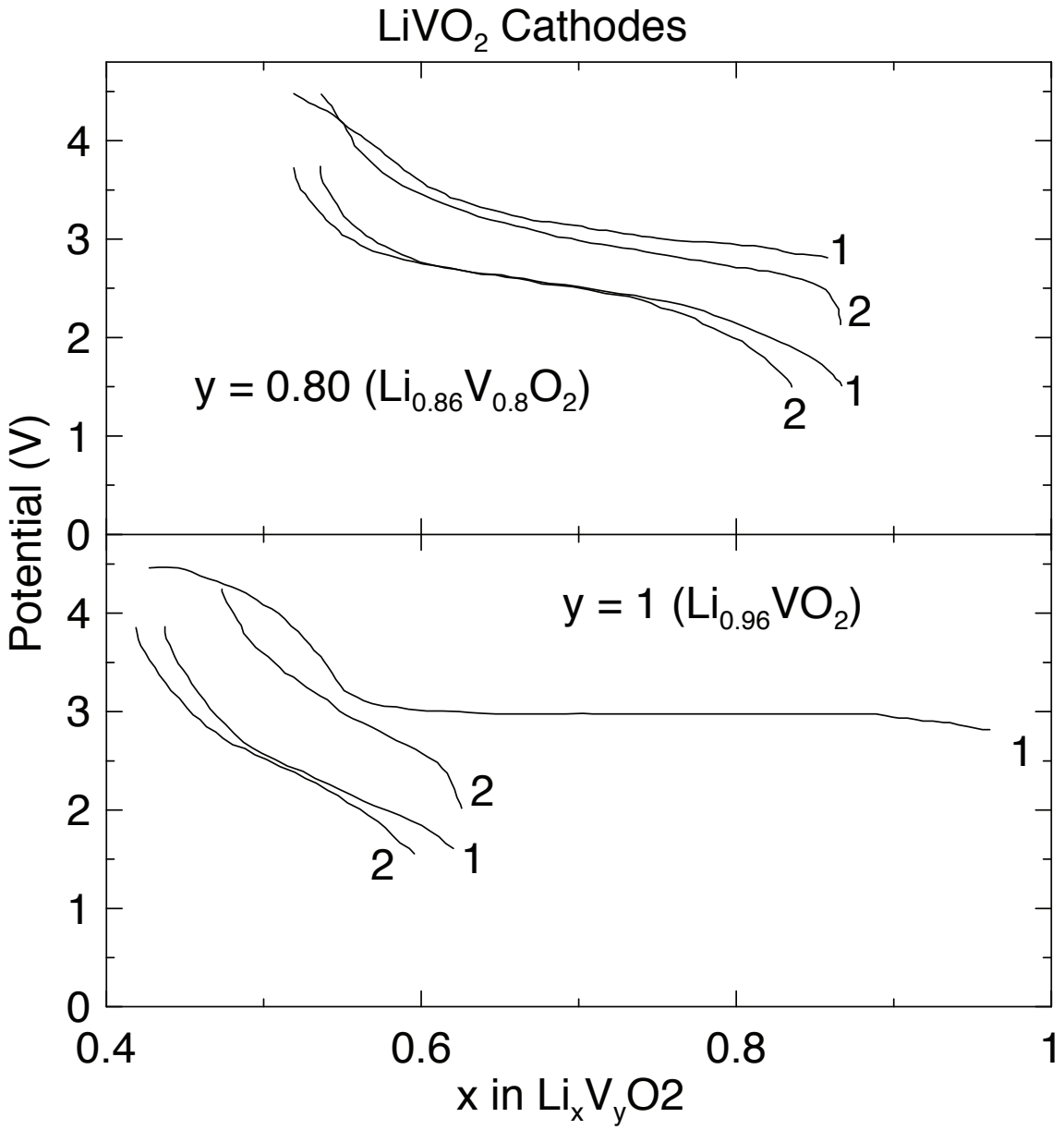

Figure 10
Electrochemical performance of $Li_{0.86}V_{0.8}O_2$ produced by hydrothermal reaction (top) and $Li_{0.96}VO_2$ produced by solid state reaction from Ozawa et al. [43]. Two cycles are shown.

This is again around the limit of Li extraction without destroying the VO_2 framework. Li was further extracted to about x = 0.45 during which the potential rose to ≈ 4.5V (total specific capacity at this point was ≈ 150 mAh/g). Subsequent cycles had a reversible

capacity of only about 0.18 Li (≈ 50 mAh/g) over this sloping region. Ex situ XRD scans on these cells determined that the initial $LiVO_2$ did not regain its layered structure during discharge. The hydrothermal sample cycled reversibly between $Li_{0.86}V_{0.8}O_2$ and about $Li_{0.55}V_{0.8}O_2$. This corresponds to about 100 mAh/g. The potential ranged from about 1.5 to 4.5V and was sloping throughout the curve with steeper slope at the ends.

The fact that there is irreversible capacity is not surprising for $LiVO_2$ since it is known to transfer up to one third of its V to the Li layer if around a third of its Li are themselves missing, and also since it is known that Li do not occupy the V layer. When Li was extracted from $Li_{0.96}VO_2$ some of the vanadium cations occupied Li sites. This would prevent them from being reoccupied by Li. It is tempting to wonder if the initial charge would be reversible if the amount of removed Li were limited to less than 0.30. The behaviour of the hydrothermal sample contrasts strongly with the stoichiometric $LiVO_2$. Perhaps this is because it already has a large degree of cationic disorder and is consequently able to reintercalate essentially all Li that is removed.

While research such as that by Ozawa et al. demonstrate the ability of layered transition metal oxides such as $LiVO_2$ to maintain their structure after a significant proportion of Li have been removed there is also research showing that several of these compositions can accommodate the insertion of large quantities of additional lithium by electrochemical means (I am not referring to “excess lithiated” layered metal oxides which are synthesized with some Li occupying transition metal sites, although some of those fit in this class). This was noticed [45] in $LiNiO_2$. This material has an open circuit voltage of

about 3.4 V and upon lithiation there is a rapid drop in voltage to about 2.0V. At this potential close to 0.55 lithium can be intercalated. Charging back to 3.4V shows that the voltage curve is path dependant. There is a plateau at about 2.5V corresponding to the removal of the last 0.2 Li to be intercalated and about 0.15 of the additional Li is still in the material at 3.4V. This reaction is largely reversible with less than 20% capacity loss after 100 cycles. When Li is intercalated past the composition $LiNiO_2$ a new phase is formed as evidenced by the appearance of new XRD peaks. XRD results indicate that for $Li_{1.66}NiO_2$ there is about 29% of the original phase remaining.

Figure 11 shows the exact structure of the new phase that was elucidated [46] using neutron diffraction (which is much more sensitive to Li than x-rays) and described as identical to the $Ni(OH)_2$ structure. It has a layered structure similar to the original phase except that each unit cell holds two Li^+ in tetrahedral sites of the Li layer instead of one in an octahedral site and the stacking of the planes is altered. The space group of the new Li_2NiO_2 phase is P-3m1.

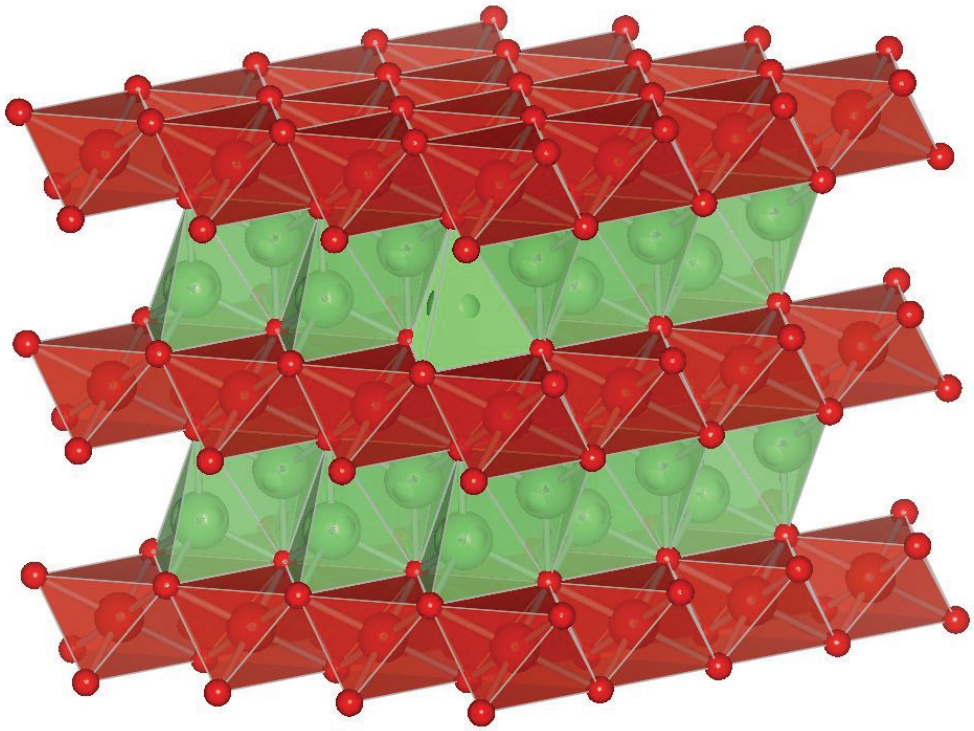

Figure 11

The V-layers of $R\bar{3}m$ $LiVO_2$ (or $LiNiO_2$) shear to A-A-A stacking to form 1T Li_2VO_2. The Li-layer of this structure contains Li in the two tetrahedral sites and no Li in the octahedral site. This allows for twice the Li content. One of these tetrahedra is highlighted in the centre of the top Li-layer.

The ability to electrochemically intercalate lithium in Li-metal oxides has also been observed for the so called "excess lithiated" cathode materials $Li_{1+x}(Ni_{0.5}Mn_{0.5})_{1-x}O_2$ [1, 47]. These materials are complicated by the presence of two concurrent transition metal oxidation states for Ni and Mn as well as the tendency of excess lithium in the transition metal layer to want to form Li_2MnO_3 as a distinct phase [47]. The consequence of the first of these facts is that there is a quantity of Ni (i.e. x) that has been oxidized to Ni^{3+} from Ni^{2+}. The consequence of the second point is that the cationic ordering in the metal layer increases with x and there is a peak observed in the XRD pattern indicative of this.

Increasing x also has the effect of reducing both lattice parameters and decreasing the amount of Ni found in the Li layer after synthesis. The amount of lithium that could be inserted in the 1.3 V – 2.0 V range was found [47] to increase with x. At x = 0 there was no capacity in this range and this was attributed to an overpotential caused by Ni in the Li layer. By x=0.15 the capacity had grown to 100 mAh/g. This capacity was associated with an expansion in the c axis of about 20% and, since we can expect a concomitant amount of swelling and cracking, is likely to blame for a capacity loss of 25% after 20 cycles in the x = 0.15 sample.

In 2005 an application was filed with the European patent office describing a "negative active material for non-aqueous electrolyte battery, method of preparing same, and non-aqueous electrolyte battery comprising same" [16]. The patent claimed a range of compositions based on $Li_{1.1}V_{0.9}O_2$. This patent served as motivation for the research in this thesis and several examples from within will be described.

Figure 12 shows electrochemical properties of the composition $Li_{1.1}V_{0.89}Mo_{0.01}O_2$ prepared from Li_2CO_3, MoO_3 and VO_2 powders. These were mixed and heated at 1100C in a nitrogen atmosphere. This composition has the structure of $R\bar{3}m$ $LiVO_2$. The average particle size of two similar (both $Li_{1.08}V_{0.9}Mo_{0.02}O_2$) samples was 35 and 80 micrometers. This was mixed with a graphite conductive agent and polytetrafluoroethylene (PTFE) binder in a mass ratio of 80/10/10. This powder mixture had a density of 1.6 g/cm^3. A slurry was made of this mixture in n-methyl pyrrolidinone (NMP) and electrodes were made on copper foil.

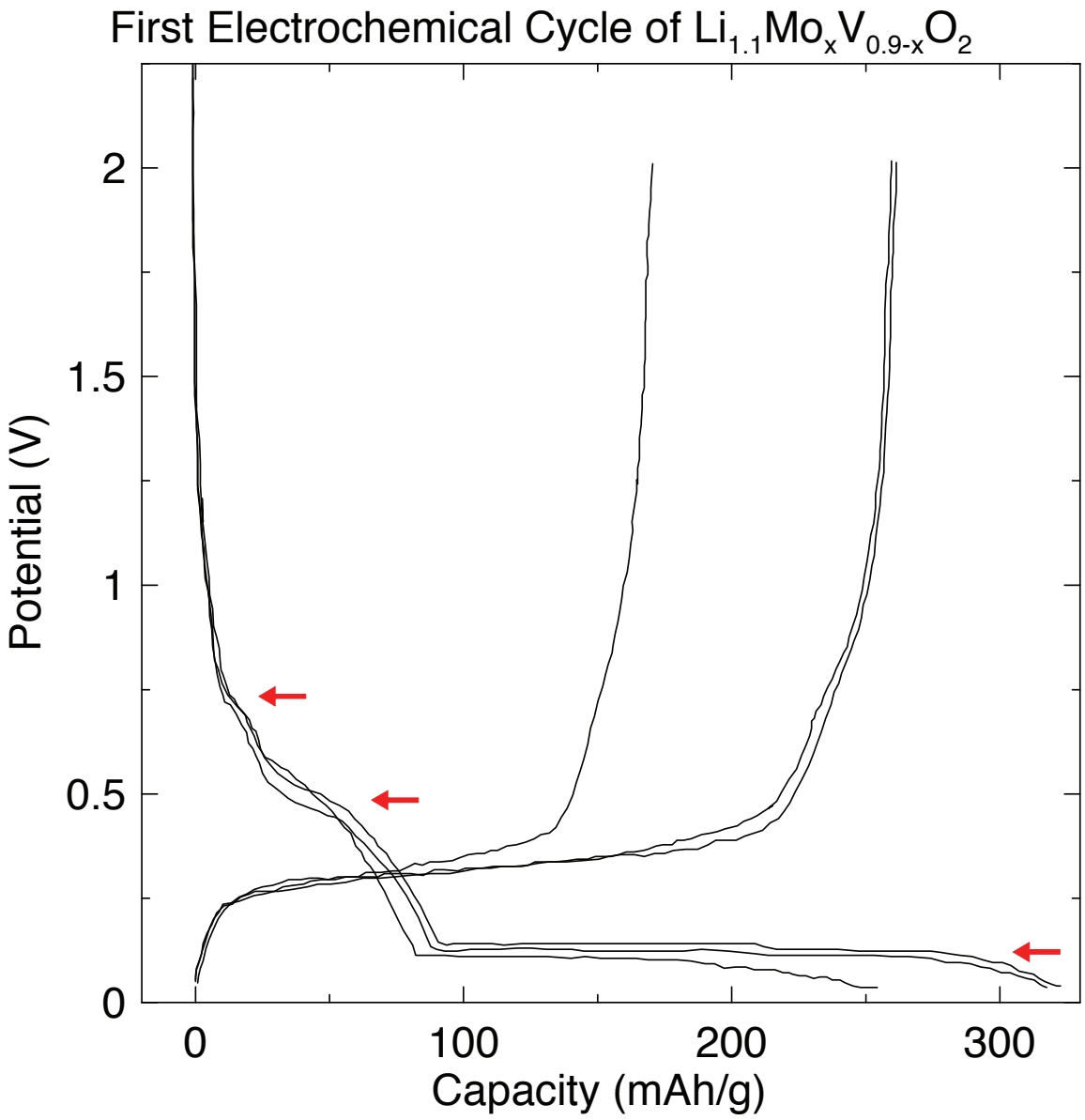

Figure 12
First discharge/charge cycle for three members of the series $Li_{1.1}Mo_xV_{0.9-x}O_2$. Due to the quality of the original image in the patent [16] the values of x can only be narrowed down to three of the four: 0, 0.01, 0.03, and 0.05. Arrows indicate plateaux on discharge.

The resulting half-cells had an initial discharge capacity of about 325 mAh/g. The curve consisted of a sloping region from about 1.0V to nearly 0.1 V at about 90 mAh/g and then a long flat plateau of about 230 mAh/g. The sloping region had two short plateaux at

about 0.75 V and 0.5 V. This behaviour was shown for the $Li_{1.1}M_xV_{0.9-x}O_2$ system with $x \leq 0.05$ and M = Ti, Mo. There was a small increase of capacity with x.

Figure 13 shows the results of $Li_{1.1}V_{0.89}Ti_{0.01}O_2$ [16] mixed with an equal mass of graphite conductive agent after which the resulting mixture was combined with PTFE in 90/10 mass ratio. This material displayed the same capacity as the previously mentioned sample but the sloping region was reduced to less than 25 mAh/g and had no apparent inflection points. Samples of this composition charged at the normal (unstated) rate had an initial capacity of 240 mAh/g in constant current (CC), constant voltage (CV) mode or 220 mAh/g in CC. This reduced to 160 (CC/CV) or 140 (CC) mAh/g in a linear manner. The density of the active material in this example was "increased" to 2.4 g/cm^3 and cells were made in the same manner. These had an initial capacity of 300 mAh/g (both) and 300 (CC/CV) or 250 (CC) mAh/g after nine cycles.

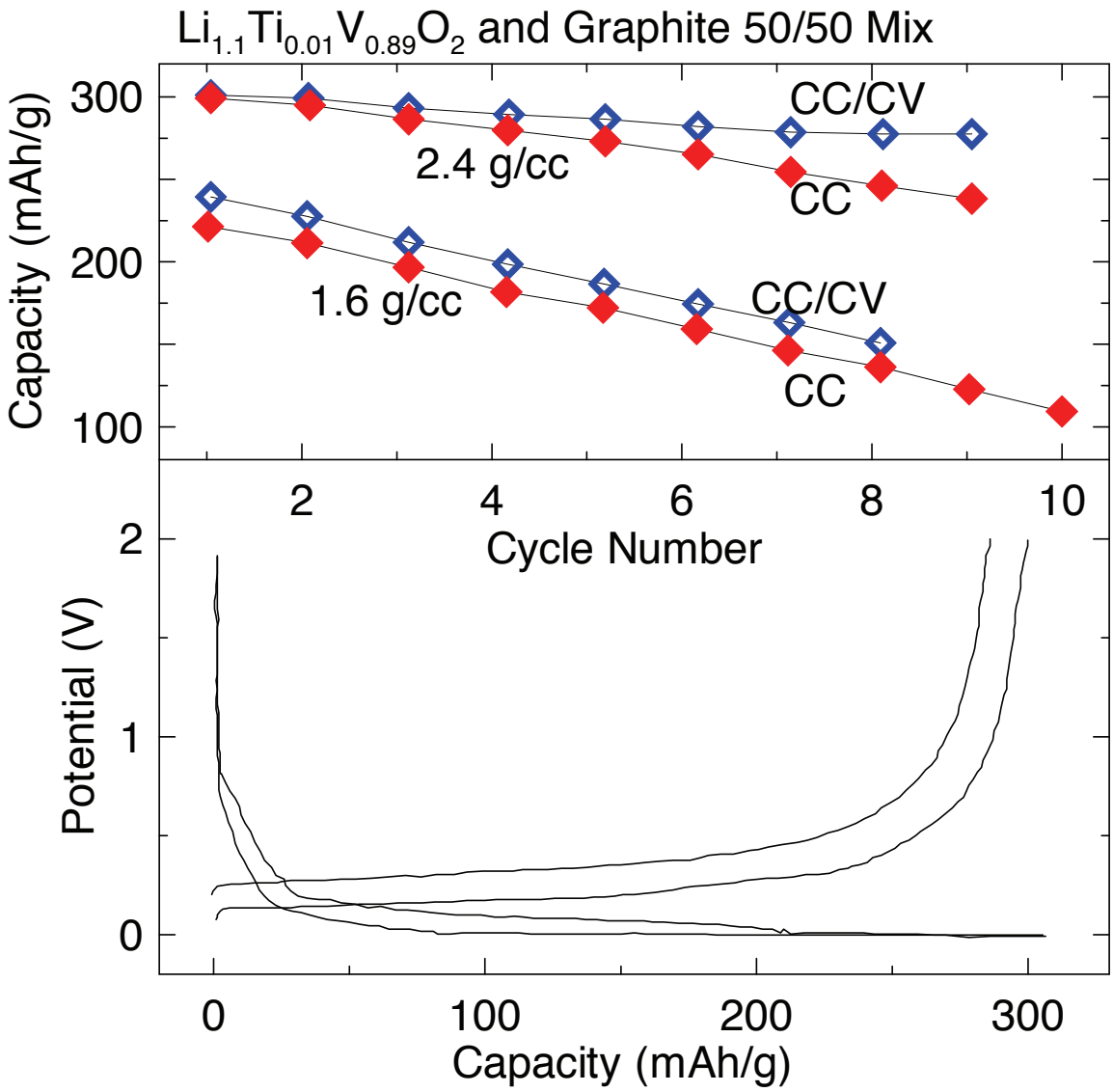

Figure 13
Electrochemical characteristics of $Li_{1.1}Ti_{0.01}V_{0.89}O_2$/graphite 50/50 (by mass) half-cells [16]. Two different densities were tested using constant current, constant voltage (CC/CV) mode and constant current (CC) mode.

Figure 14 shows that the voltage curves were very different between $Li_{1.08}V_{0.9}M_{0.02}O_2$ (M = Ti, Mo) and $Li_{1.1}M_xV_{0.9-x}O_2$ ($x \leq 0.05$, M = Ti, Mo), both from [16]. All these compositions were made with active mass/conductive graphite/binder mass ratio of 80/10/10. The former had a sloping region shortened to about 60 mAh/g if M = Ti, otherwise it was larger (150 mAh/g) and concave upward if M = Mo. In both cases total

capacity was unchanged. Capacity retention was shown for $Li_{1.08}V_{0.9}M_{0.02}O_2$ cells made with 80/10/10 formula. The initial capacity was about 325 mAh/g and was still greater than 250 mAh/g after 20 cycles.

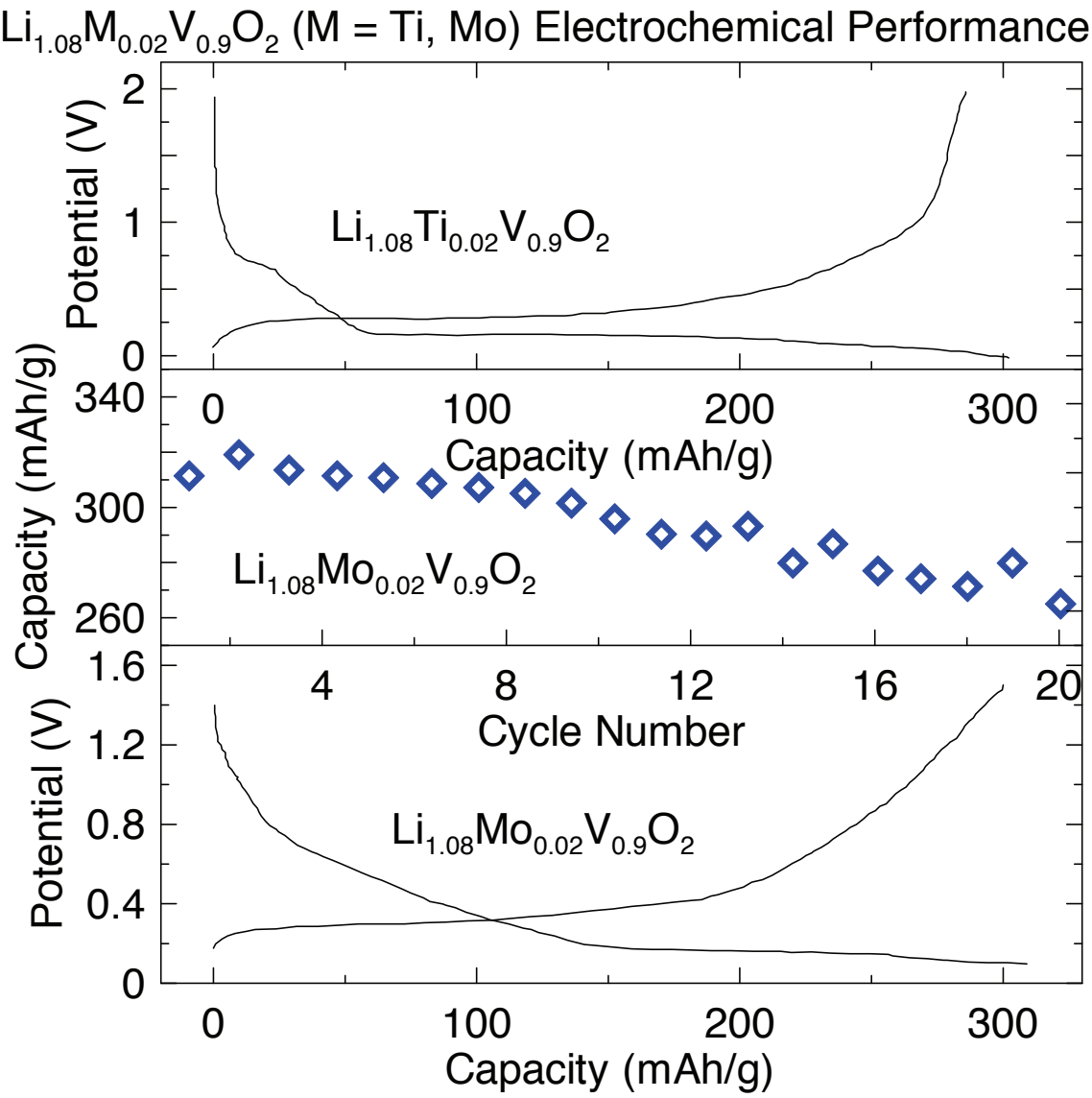

Figure 14
$Li_{1.08}M_{0.02}V_{0.9}O_2$ (M = Ti, Mo) [16] shows considerable difference in behaviour from $Li_{1.1}M_xV_{1-x}O_2$ (M = Ti, Mo; $x \leq 0.05$) and variability between samples with different M. Capacity of $Li_{1.08}Mo_{0.02}V_{0.9}O_2$ mixed 80/10/10 with PTFE and graphite shows capacity retention comparable to the 50/50 graphite mix.

A paper [5] published by some of the authors of the patent investigated the cycle life characteristics of $Li_{1.1}V_{0.9}O_2$. It is claimed therein that the theoretical capacity is 313.6 mAh/g or 1064 mAh/cm^3 compared to graphite with 372 mAh/g or 780 mAh/cm^3. These values are somewhat less than those given by the reference in Table 1, but reiterate the point that $Li_{1.1}V_{0.9}O_2$ is competitive with graphite on a volumetric basis. After solid state synthesis yielding particles with an average size of 25 micrometers, cells were made using an electrode of 89/6/5 weight ratio of active material, super-p carbon and PVDF in NMP. This cell had an voltage curve very similar to that shown in the patent except that the sloping region was much more of a single plateau at 0.4V with no plateau visible at 0.75V and slightly larger capacity. Figure 15 shows this data and should be compared to Figure 12.

The low voltage plateau declined gently from 0.15V for about 150 mAh/g and then with increasing slope to about 0.01V. There was about 20-30 mAh/g at this potential – something not seen in the patent. The plateau at 0.4V disappeared after the first cycle contributing to an irreversible capacity of about 80 mAh/g which was associated with solid electrolyte interface formation and retention of the intercalated phase.

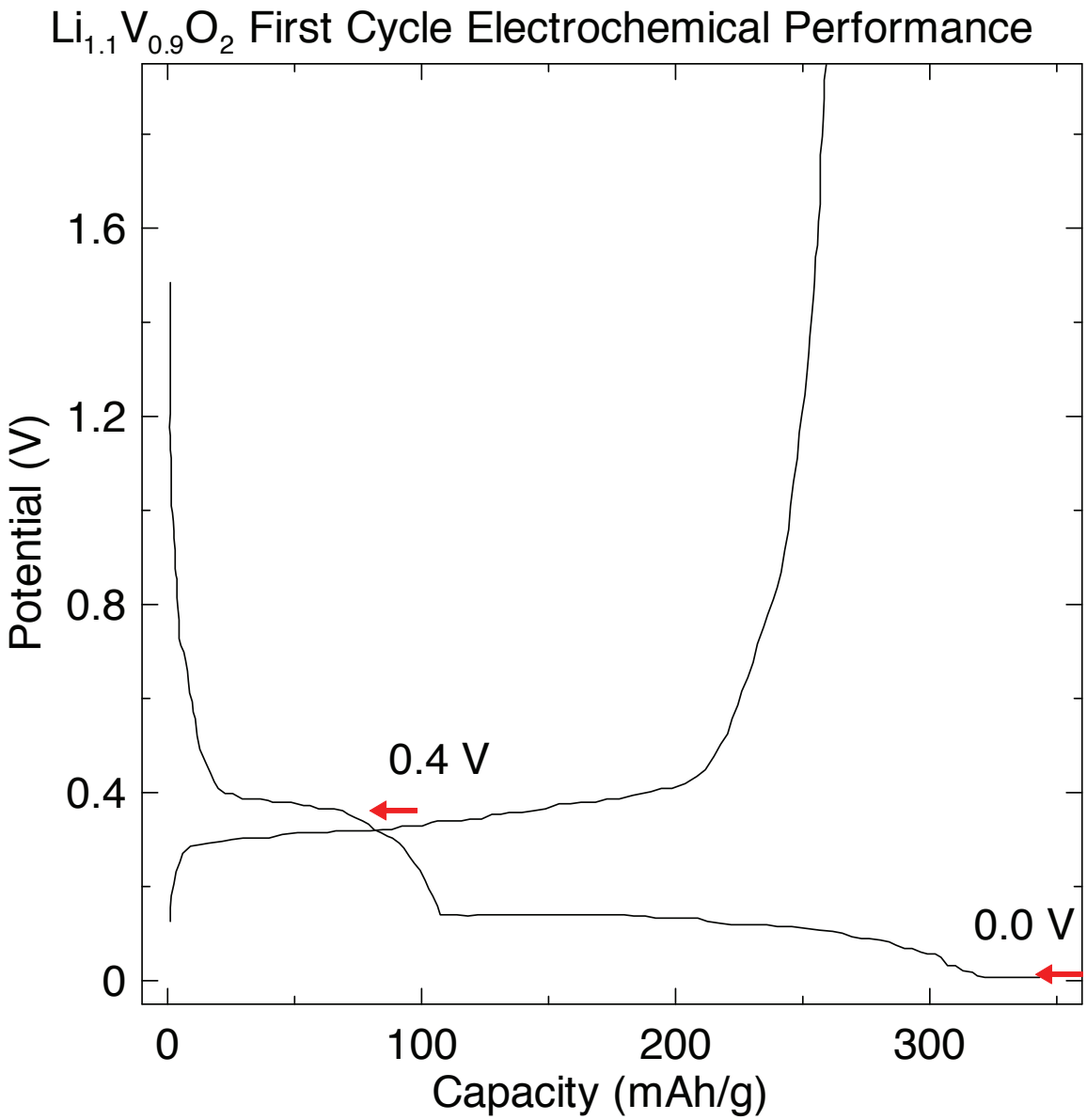

Figure 15
$Li_{1.1}V_{0.9}O_2$ from reference [5]. The features at 0.4 V and 0.0 V differ from other samples of this composition as discussed in the text.

Cells were cycled 20 times over two different ranges of potential. Between 0.01V and 2.0V capacity was nearly constant at 250 mAh/g after the initial drop from 350 mAh/g. When cycled between 0.01V and 1.0V the capacity declined from 250 mAh/g to 150 mAh/g. This suggests that $Li_{1.1}V_{0.9}O_2$ is more stable when cycled in a restricted voltage range.

The fact that negative electrode compositions related to $LiVO_2$ have only been reported for excess lithiated compositions of the form $Li_{1+x}V_{1-x}O_2$ attracted enough attention to warrant a study [3] on that topic. Samples were made via solid state reaction from this series and found to have a particle size of 100 nm to 200 nm. Making a cell with the recipe 75/18/7 active material, super-S and PVDF, electrochemical behaviour very similar to that seen in the patent was found for excess lithiated materials where capacity increased with x up to x = 0.07. For x = 0 the low voltage plateau was very short, situated at 0 V and thus more likely to represent lithium plating than intercalation. Larger low voltage plateaus started at 0.1-0.2V for $x > 0$. Ex-Situ x-ray and neutron diffraction was conducted on the material in various states of discharge and the 1T Li_2VO_2 phase (Figure 11) reported for Li_2NiO_2 [45, 46] was seen to grow in proportion to the distance along the low voltage plateau. Interestingly, quantification of the phases tended to understate the actual amount of charge that had been passed suggesting that formation of the Li_2VO_2 phase coexisted with some sort of irreversible consumption of the Li.

To shift from one phase to the other requires a shearing of the O^{2-} layers from cubic to hexagonal stacking. It is unlikely that this is prevented in $LiVO_2$ by V in the Li layer as cationic disorder was found to be energetically unfavourable in this material and XRD found no such disorder to be present. It was found that the presence of Li in the V layer made adjacent Li layer tetrahedral sites energetically available, allowing them to be occupied at a potential of 0.58V. Once these sites are occupied, Li^+-Li^+ repulsions from all four nearest neighbors (see Figure 9) help to induce shearing of the O^{2-} plane leading

to the Li_2VO_2 structure. This might suggest that the sloping region of the electrochemical data could be associated with tetrahedral site occupation even though the plateaux at 0.75-0.8V and 0.4-0.5V are slightly off from the predicted voltage of 0.58V [3]. There is in fact a small increase in both lattice parameters here but the near complete disappearance of these plateaux after the first cycle suggests they are largely accounted for by electrolyte reduction or SEI formation. Li introduced into the V layer has a tendency to cluster with the two V^{4+} it creates. This has lead to an unfortunate second introduction of the word "trimer" in the $LiVO_2$ literature.

CHAPTER 3 EXPERIMENTAL TECHNIQUES

SAMPLE SYNTHESIS

All samples were produced using solid state synthesis. Precursors came in the form of metal oxide powders: V_2O_3 (Aldrich, 98%) and Li_2CO_3 (Alfa Aesar, 99.0%). These were ground by hand with an agate mortar and pestle in air. The ground powders were placed in graphite crucibles for heating. Earlier attempts to use alumina crucibles showed that the $LiVO_2$ had a strong tendency to stick to alumina. The crucibles were inserted into a high purity alumina tube. The tube was capped to make it airtight and argon was flushed through the system while heating occurred. At temperatures above 800° C $LiVO_2$ will oxidize to $LiVO_3$ in the presence of air [18]. The flow of argon was maintained throughout the duration of the heating time. Most samples were treated for seven or eight hours at 1000° C. It is necessary for the temperature to exceed at least 800° C for $LiVO_2$ to be more stable than LiV_2O_4 and LiV_2O_5 [48].

Table 2 shows the timings at which various stages of investigation were carried out for each sample considered as well the conditions under which they were produced. Each was prepared in the same way with the same reactants and only one heating. The exception is that the heating time of the samples produced in 2010 was reduced to seven hours. Samples produced in the intervening period (not reported here) showed that one hour difference had little effect.

Sample	Stoichiometry	Heating Time (Hours)	Heating Temperature (°C)	Synthesis Date	Days Until XRD	Days Until Superlattice Scan	Days Until Anode
JG17	Li1.1V0.9O2	8	1000	14-May-09	13	121	65
JG132	Li0.9V1.1O2	8	1000	3-Jun-09	0	101	42
JG133A	Li0.95V1.05O2	8	1000	4-Jun-09	0	101	41
JG133B	LiVO2	8	1000	4-Jun-09	1	100	42
JG137A	Li1.05V0.95O2	8	1000	5-Jun-09	0	104	41
JG137B	Li1.15V0.85O2	8	1000	6-Jun-09	2	98	41
JG137C	Li1.2V0.8O2	8	1000	7-Jun-09	1	102	44
JG1103A	Li0.875V1.125O2	8	1000	18-Jul-09	3	79	-
JG1103B	Li0.925V1.075O2	8	1000	19-Jul-09	3	78	-
JG1103C	Li0.975V1.025O2	8	1000	20-Jul-09	2	67	-
JG1104A	Li1.025V0.975O2	8	1000	21-Jul-09	2	66	-
JG1104B	Li1.075V0.925O2	8	1000	3-Aug-09	1	63	-
JG1104C	Li1.125V0.875O2	8	1000	5-Aug-09	1	61	-
JG275A	Li1.1V0.9O2	7	1000	2-May-10	0	-	14
JG275B	Li1.1V0.9O2	7	1000	2-May-10	0	-	14
JG298B	LiVO2	7	1000	9-Jul-10	2	-	17
JG298C	Li1.1V0.9O2	7	1000	9-Jul-10	2	-	4

Table 2
Synthesis conditions and timings for samples of the $Li_{1+x}V_{1-x}O_2$ series considered in this work. Day number is relative to synthesis date.

X-RAY DIFFRACTION

X-ray diffraction was used to characterize the crystallographic structure of the prepared powders. The powders were placed in a depression in an aluminum slide with dimension of approximately 2.0 cm x 1.5 cm x 0.4 cm. The surface of the powder was made level by dragging the edge of a glass plate across the top of the slide. The slide was place at the focus of a Bragg – Brentano goniometer arrangement. The source was a water-cooled copper x-ray tube. The apparatus contained a crystal monochrometer as well as divergence, anti-scatter and receiving slits. These were set at 0.75 mm, 0.75 mm and 0.2 mm, respectively. The apparatus collected intensity at intervals in the scattering angle of 0.05°. For most scans this apparatus was stepped through a range of scattering angles between 10° and 80° with a count time of eight seconds at each angle. In actuality, the

goniometer moved continuously in “locked-coupled” mode and the counts were binned in 0.05° intervals.

Diffraction patterns of the superlattice structure in $LiVO_2$ were acquired in essentially the same manner. The scan was conducted over a range of scattering angle from 19.3° to 22.3°. Due to the very low intensity of the superlattice peak, the count time was set at 200 seconds. The long count time made it impossible to use the “locked-coupled” mode so all counts were from stationary positions at 0.05° intervals.

Lattice parameters were extracted from the regular XRD spectra using the in-house HEXOFF software. HEXOFF uses peak locations from diffraction patterns of hexagonal systems to determine lattice constants using least-squares refinement of the lattice constants to minimize the differences between the measured and calculated diffraction angles .

Superlattice peaks were analyzed by visual comparison and more in depth analysis was conducted using non-linear fits from the Fityk [49] software package. (See results section for more depth.)

ELECTROCHEMICAL TESTS

Electrodes were formed from powdered samples. This was accomplished by mixing the active (prepared powder) material with a conductive constituent and polymeric binder in the presence of a solvent. The two binders used were lithium polyacrylic acid (Li-PAA),

which was dissolved using water as the solvent, and polyvinyldiene fluoride (PVDF) which used n-methyl pyrrolidinone (NMP) as a solvent. The mixing was accomplished with one of two methods. The first involved placing four stainless steel balls with the powders and solvent inside an egg shaped cavity of a stainless steel ball mill vial. This was shaken in a low energy ball mill for approximately 20 minutes. The other method used zirconia beads in a plastic vial shaken by a Kurabo Mazerustar mixer for 600 seconds (see reference [50] Figure 4c).

The resulting slurry was spread on copper foil that had been roughened on both sides using Scotchbrite. This improves adhesion by increasing surface area and removing the oxide layer. This foil was forced to adhere to a smooth glass pane by the surface tension of a thin layer of ethyl alcohol between the two surfaces. The slurry was spread at a specified thickness using a notch bar which had a finely machined edge that was held a specified distance above the foil when its ends rested on the surface of the glass. A notch bar and its effect can be seen in Figure 2 and Figure 3 of reference [50]. The 0.0015" notch bar was used for slurries mixed with Li-PAA and the 0.006" notch bar was used for those with PVDF. The choice of notch bar for Li-PAA slurries was motivated by their poor adherence to the copper foil. Spread slurries were placed in an oven set at approximately 90° C until the solvent had evaporated. This generally was about three hours. Excessively slow drying should be avoided to prevent sedimentation in the mixed slurry. Slurries containing NMP were dried in an oven placed in a fumehood as it is known that concentrations as low 0.7 ppm can produce severe eye irritation and headache

after 30 minutes of exposure while occupational exposure has been documented as leading to stillbirth [50] (and references therein).

Round electrodes with a surface area of approximately 1.3 cm^2 were removed from the dry slurry coated copper foil by means of a mechanical punch ([50] Figure 4f). These were weighed and assembled into coin cells in an argon filled glove box. The coin cell casing consisted of a stainless steel cap and can sealed with a plastic gasket by way of a pneumatic press. The internal components of the cell consisted of the dry slurry electrode, two layers of Celgard separator and a lithium foil counter electrode followed by a stainless steel spacer and spring which maintained pressure and thus good contact within the cell. A small quantity of electrolyte was added between the layers of separator as well as between the separator and each electrode. This electrolyte was a 1.0 mol/l solution of $LiPF_6$ in a 1:2 weight ratio of ethylene carbonate (EC) and diethyl carbonate (DEC). Coin cell assembly is well described in reference [52]. In light of of the effects of air exposure, described within, it is an unfortunate fact the the amount of time which samples sat in air awaiting electrode synthesis and the amount of time electrodes sat in air prior to cell assembly were not carefully controlled.

By convention, the potential of reaction mechanisms in Li-ion batteries are measured relative to the potential of elemental Li. Cells made using Li foil as one of the electrodes are referred to as “half cells” as they simply measure the potential of a battery electrode relative to Li (i.e. it is referenced to zero). Those which measure the effect of using two types of electrode material (other than elemental Li) in the same cell are referred to as

"full cells". Due to the very low potential of elemental Li, all materials assume the role of cathode or positive electrode when assembled in a half cell, even those traditionally used as anodes such as graphite. All electrochemical results reported in this work are for Li half cells. In this work, discharge refers to the process whereby Li^+ and e^- are transferred from the Li counter electrode to the $LiVO_2$ electrode. The potential measured across the cell decreases during discharge. Charge refers to the process where Li^+ and e^- are removed from the $LiVO_2$ electrode and find their way back to the electrode of elemental Li. The $Li_{1.1}V_{0.9}O_2$ potential increases during this process and work must be done on the cell if it is to occur.

$Li/LiVO_2$ half-cells were tested in a continuous cycle of discharge and charge between the potential limits of 0.005 V and 2.0 V. This cycling was done at constant current. Cell potential was read every 150 seconds and a new data point was only recorded if the potential had changed by more than a preset precision value of 0.005 V. This process occurred over the duration of several days and was controlled by computer software. As the materials under consideration are far from the point of being considered a well understood and marketable product, it is more important at this time to elucidate a reaction mechanism and explain the features of the charge and discharge curves than to study the rate behaviour of the material. As a result, the consistency of charge rates was not monitored with extreme precision but they were kept sufficiently low to preclude the influence of rate characteristics on electrochemical results. The rate of C/20 is representative, where a rate of C/*n* indicates full discharge in 1/*n* hours.

CHAPTER 4 RESULTS

$Li_{1+x}V_{1-x}O_2$ STRUCTURE

The $Li_{1+x}V_{1-x}O_2$ series was created by solid state synthesis at a temperature of 1000°C for eight hours. Figure 16 shows the XRD patterns of the resulting black powders. This series is actually comprised of two subsets. The first consists of the compositions corresponding to values of x between -0.10 and 0.30, inclusive. These were prepared in steps of $\Delta x = 0.05$. The second series of compositions corresponds to values between -0.125 and 0.125, with the same spacing, and was made at a later date to confirm and augment the results of the first series. For values of $-0.125 \leq x \leq 0.10$ these samples are single phase $R\bar{3}m$ $LiVO_2$ (see Figure 3) except for the possibility of a small amount of graphite from the boat in which they were reacted. This is seen as a small peak at 26°. The relative intensities of the 003 and 104 peaks at 18° and 44°, respectively, are seen to fluctuate. This is used as an indication of cationic disorder in many references [37, 43, 44] however it can also indicate preferential orientation during XRD analysis and is thus of little value without a more complete refinement or additional information about the series. For $x \geq 0.125$ the emergence of the Li_3VO_4 phase makes itself apparent in the three sharp peaks at scattering angles just greater than 20°.

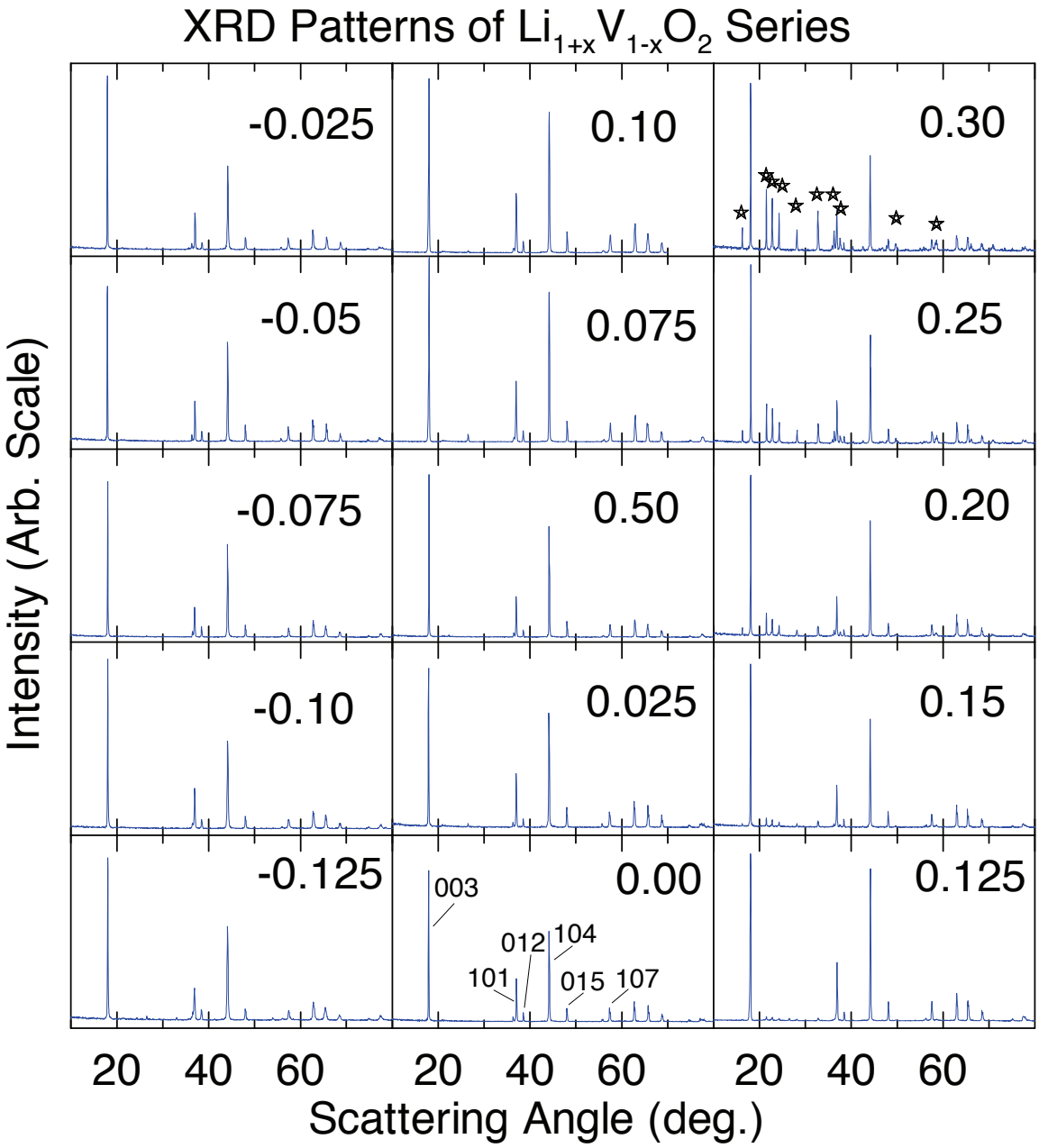

Figure 16
XRD patterns of the $Li_{1+x}V_{1-X}O_2$ series. Each scan is labeled by the value of "x" that corresponds to it's composition. The emergence of Li_3VO_4 for $x \geq 0.15$ is observed as the three sharp peaks at angles just above 20 degrees. $LiVO_2$ peaks are labeled in the x = 0.00 panel. Li_3VO_4 peaks are indicated by stars in the x = 0.30 panel.

Lattice parameters were determined from these spectra using the HEXOFF program which refines lattice parameters for crystals of hexagonal symmetry from peak locations

in the XRD spectra. Figure 17 shows plotted Lattice parameters for the $Li_{1+x}V_{1-x}O_2$ series.

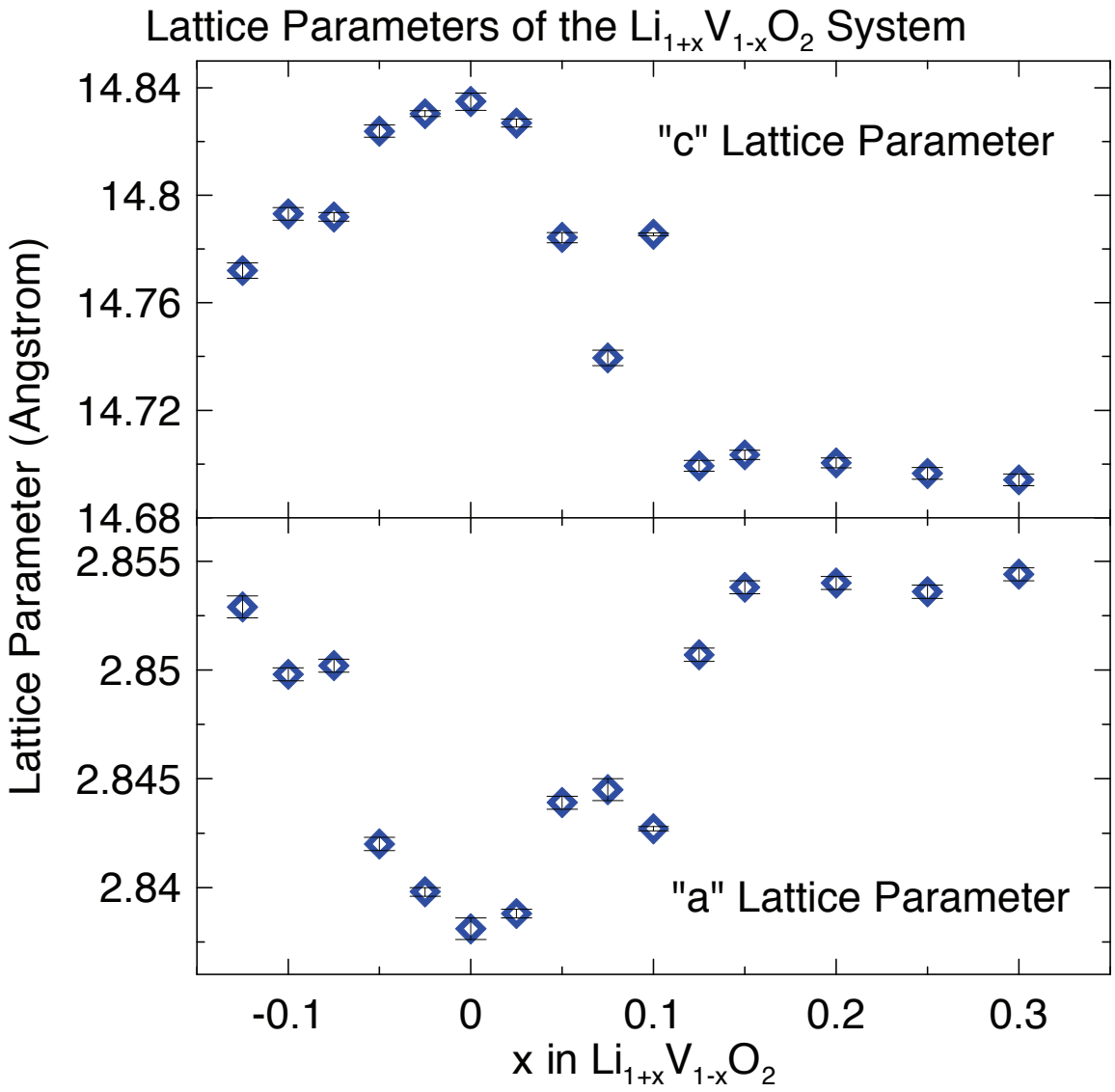

Figure 17
Lattice parameters determined from XRD data using HEXOFF lab software. The extrema at x = 0.00 correspond to the distorted lattice caused by V^{3+} orbital ordering. The $x \geq 0.15$ region contains significant amounts of Li_3VO_4.

The plots show a region of strong variation with x that is centered around x = 0. At that point the "c" lattice parameter is at a maximum and the "a" lattice parameter is at a minimum. This corresponds to the oxygen layers in Figure 3 being furthest apart at this

composition while the ions within these sheets are drawn together. This is apparently what happens in the orbitally ordered state where V^{3+} trimers form in $LiVO_2$. As x strays from 0 in either direction "c" decreases while "a" increases. Trimer formation is believed to be very sensitive to the concentration of V^{3+} in the vanadium layer. The presence of any different ion in this site prevents two neighbouring V^{3+} from participating in orbital ordering. Figure 18 shows how, as the relative abundance of V and Li are changed, the number of electrons submitted by the V to the oxygen anions varies and the abundances of V^{2+}, V^{3+} and V^{4+} vary. Thus the lattice parameters of $Li_{1+x}V_{1-x}O_2$ should vary with x in the region around x = 0. This is essentially the same behaviour as was observed in the $LiCr_yV_{1-y}O_2$ system in Figure 7. As V was replaced by Cr, the number of lattice sites in the plane with two d-electrons decreased. At y_c a transition is observed between the trimerized and non-trimerized states. This corresponds to the kink in the lattice parameters seen in Figure 17 at about x = 0.125 or 0.15 in the $Li_{1+x}V_{1-x}O_2$ system.

The presence of orbital ordering causes a distortion of the lattice in the V plane in a periodic fashion to form trimers and the resulting superlattice peak, corresponding to the trimer-trimer separation distance at a scattering angle of 20.9° that has been reported in the literature [20]. The superlattice structure has also been reported several times [18, 22, 30, 32] for single crystals. In stoichiometric $LiVO_2$ powder the integrated intensity of this superlattice peak declined rapidly on heating between 200°C and $T_t \approx 260$°C where it disappeared [25]. This observation meshes nicely with the idea of a superlattice peak caused by a lattice distortion which, in turn, is the result of magnetic ordering. As the transition temperature is passed, this order is destroyed. As the value of x affects the

average vanadium oxidation state, and this is believed to drive the magnetic ordering of $LiVO_2$, it seems reasonable to expect the superlattice peak to vary in response to x. XRD scans for the superlattice peak of $Li_{1+x}V_{1-x}O_2$ were collected from 19.3° to 22.3° with the count time set to 200 seconds. Figure 19 shows these scans plotted and labeled by composition.

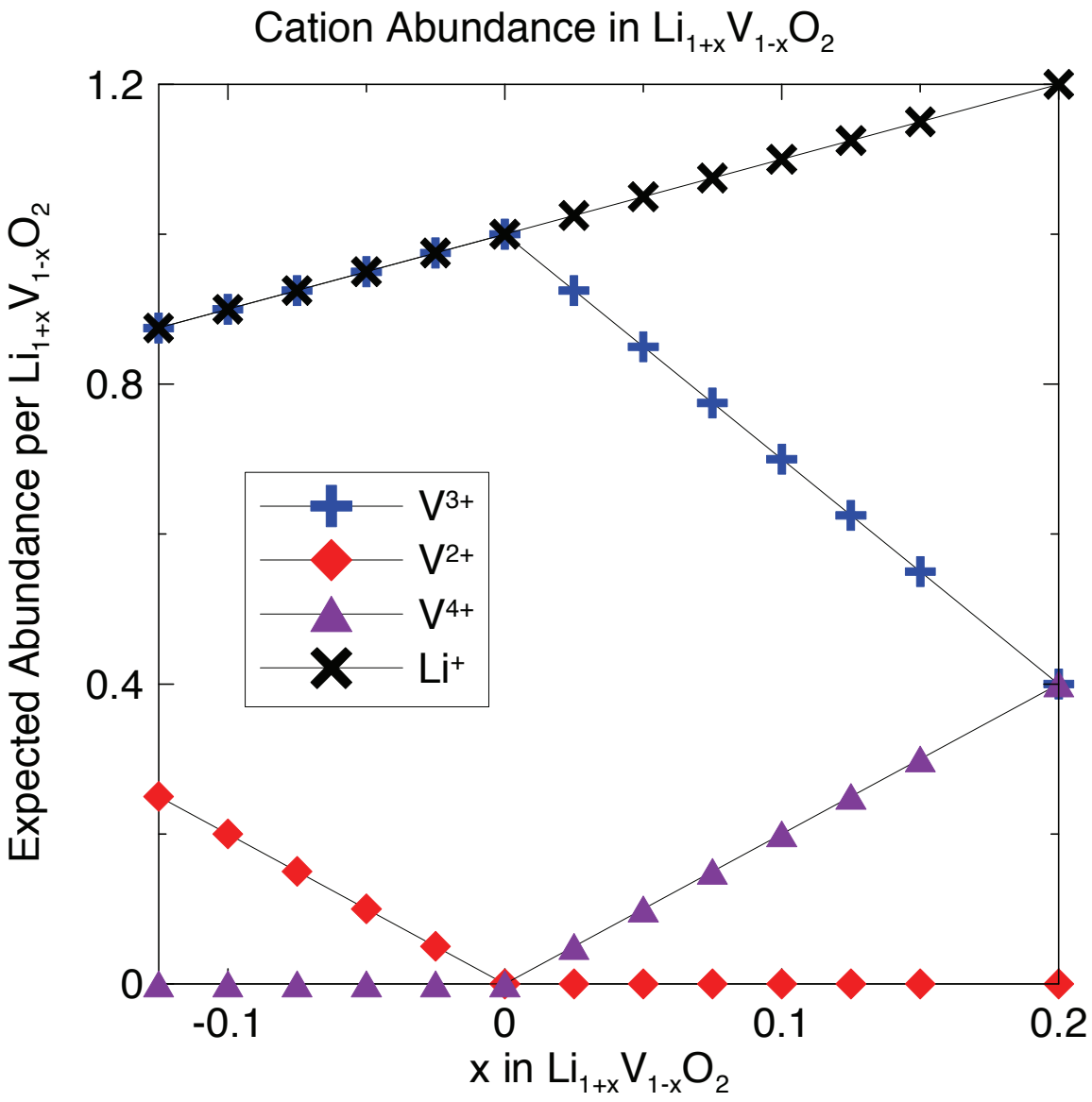

Figure 18
The calculated absolute abundance of the V^{2+}, V^{3+} and V^{4+} cations varies with x. At x = 0.00 only the 3+ state is present. For all other x there are either V^{2+} or V^{4+} present.

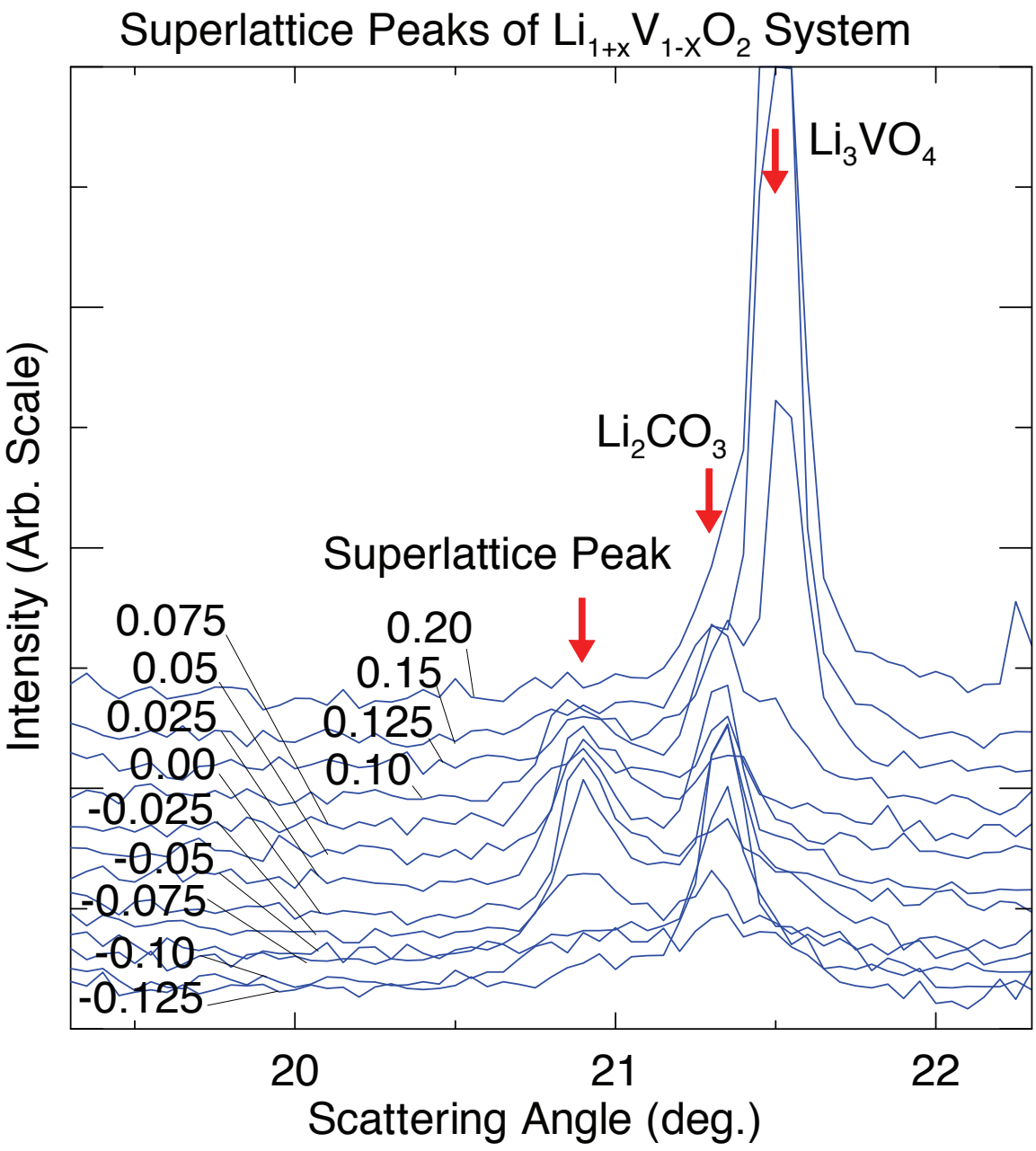

Figure 19
Superlattice peak at a scattering angle of 20.9° in orbitally ordered $Li_{1+x}V_{1-x}O_2$. Scans are labeled with their value of x.

The most obvious feature is the Li_3VO_4 peak at 21.5° that becomes apparent for $x \geq 0.10$. For small values of x this is not present. At 21.3° there is a peak due to Li_2CO_3. This appears as a low shoulder of Li_3VO_4 for large x and is much diminished for $x \leq -0.10$. The superlattice peak of orbitally ordered $Li_{1+x}V_{1-x}O_2$ is visible at 20.9°. It is most obvious in the range $-0.05 \leq x \leq 0.125$. It seems to be highest and sharpest for x = -0.025, 0.00, 0.025 and becomes more diffuse outside of this range.

To further analyze the superlattice data, the nonlinear fitting program Fityk [49] was used to extract peak information. Scans were fit to a linear background and three pseudovoigt functions representing the $LiVO_2$ superlattice peak, the Li_2CO_3 peak and the Li_3VO_4 peak. The pseudovoigt function is a linear combination of the Gaussian and Lorentzian functions with the respective weights 1-*f* and *f*. In most cases the weighting parameter was restricted to either 0 (Gaussian) or 1 (Lorentzian) to keep it from adopting unreasonable values. All other parameters were allowed to vary freely during the fitting process. In all cases the fitted peaks were centered very close to the expected angle suggesting the validity of this model. For some low values of x the addition of a Li_3VO_4 peak did little to improve the fit and was omitted. Figure 20 shows the fit of the superlattice peaks for $Li_{1.025}V_{0.975}O_2$. There is no measure of goodness of fit presented with this data.

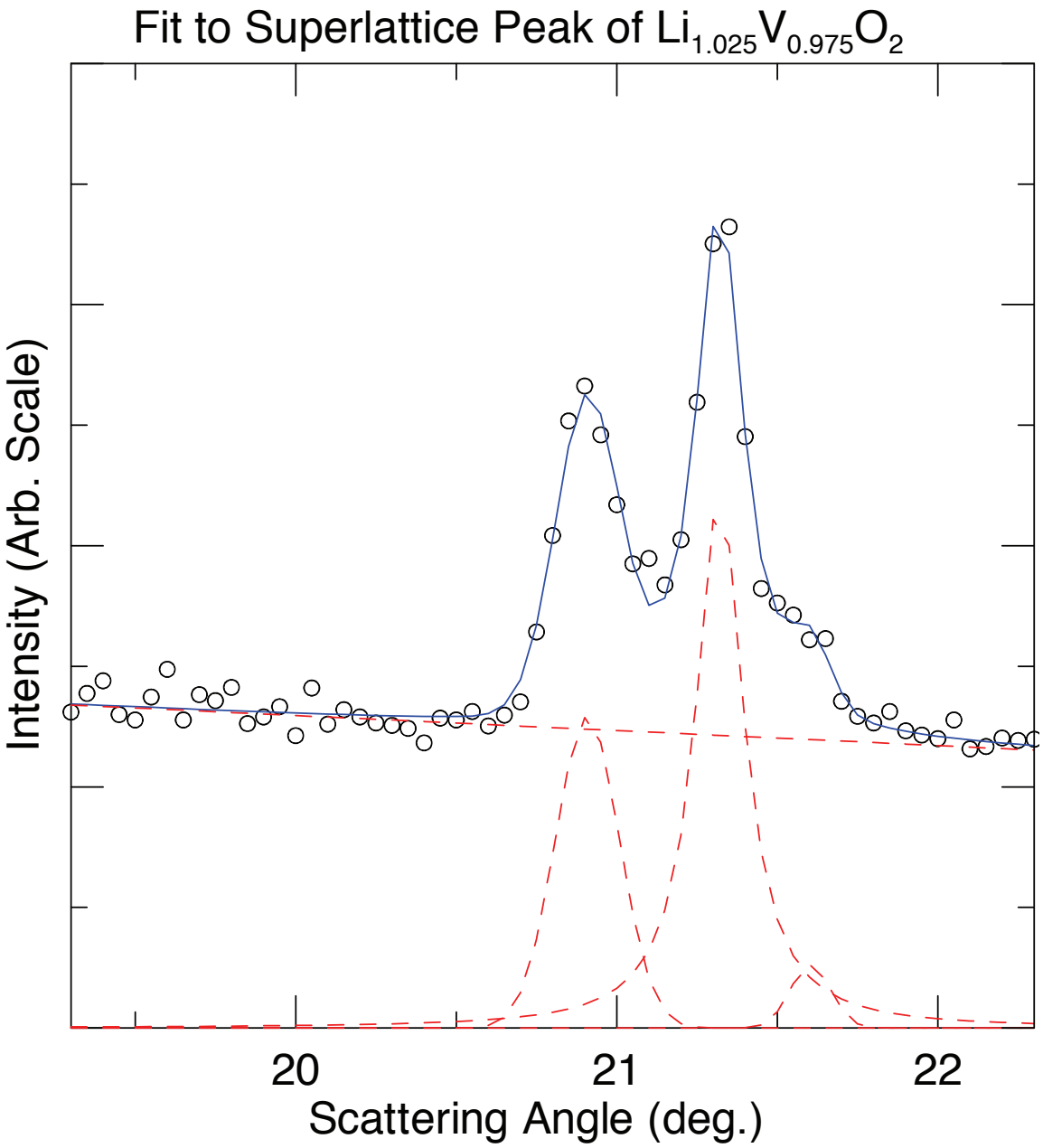

Figure 20
Example of fit to $Li_{1+x}V_{1-x}O_2$ superlattice peak using Fityk [49] nonlinear fitting software. Data is shown as small circles. Total fit and components are shown in solid and dashed lines, respectively.

Figure 21 shows the areas of the superlattice peaks as a function of x. The subsets for the two $Li_{1+x}V_{1-x}O_2$ series are plotted separately to emphasize the offset between them for $x < 0.05$.

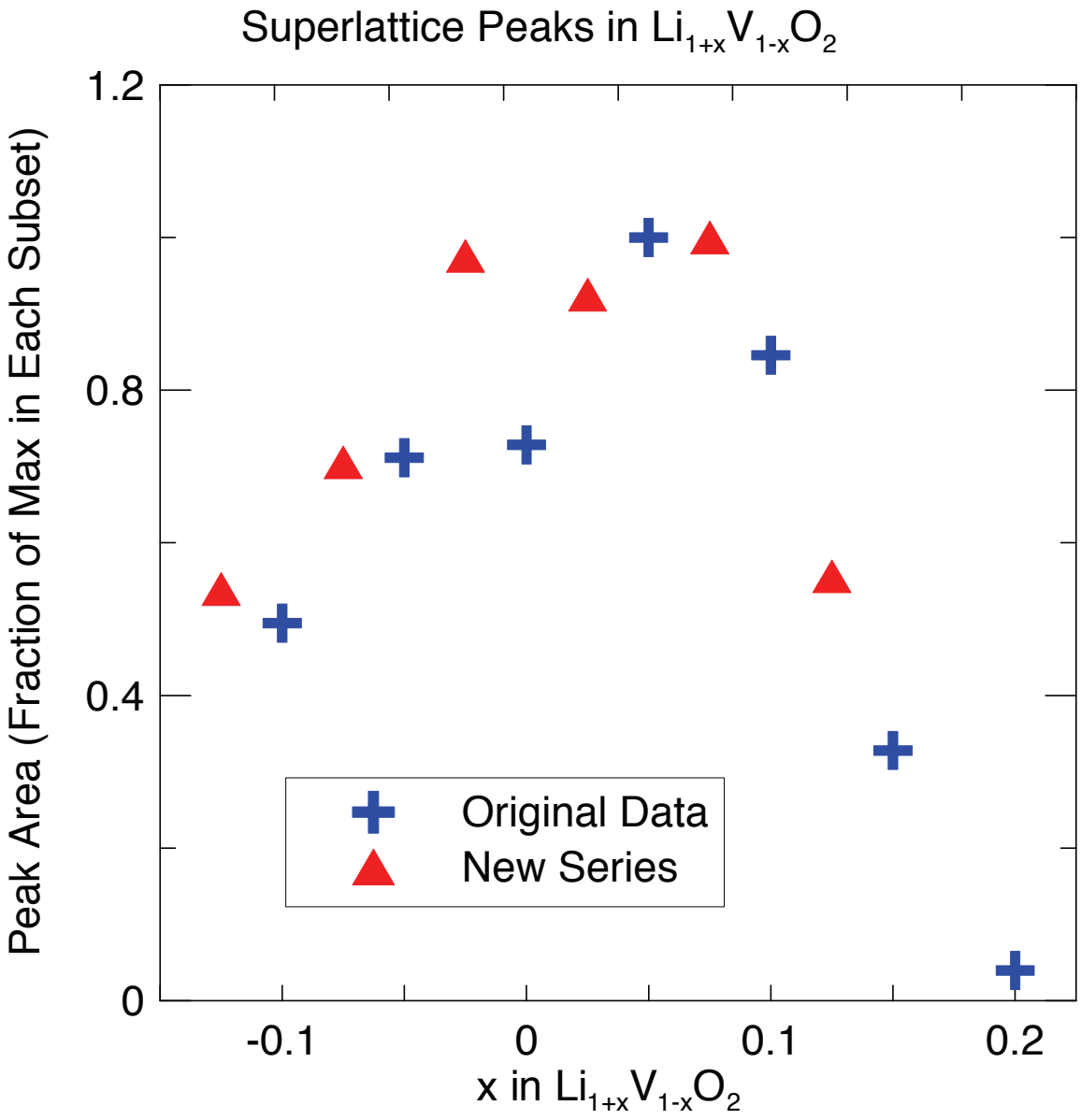

Figure 21
Fitted areas of superlattice peak of the $Li_{1+x}V_{1-x}O_2$ system. The maximum seems to occur somewhere between 0.04 and 0.07.

The peaks of the newer subset are consistently above the trend of those of the original subset in this range. The areas for each subset are scaled to a fraction of the largest value within that subset. There are strong correlations between Figure 17 and Figure 21. Drawing a smooth curve through the points in Figure 21 shows a maximum near x = 0.04

± 0.02. This is relatively close to x = 0.00 where the lattice parameter anomaly is most strong. As x deviates from zero, there is a linear decrease in both the superlattice peak area in Figure 21 and the lattice parameter anomaly in Figure 17. Both these phenomena dissappear at a value between x = 0.125 and x = 0.2. This provides compelling evidence for the claim that the lattice parameter anomaly is caused by trimer formation.

AIR AND WATER EXPOSURE OF $Li_{1+x}V_{1-x}O_2$

There is a tendency for $LiVO_2$ to undergo a small degree of bulk delithiation when exposed to air and this is associated with the formation of Li_2O, LiOH or Li_2CO_3 on the surface. Figure 22 shows the results of the repeated weighing of a small portion of two samples of the $Li_{1+x}V_{1-x}O_2$ series put aside immediately after synthesis The data shows an initially rapid gain in weight that slowed considerably by the time their weight had increased by 1%. This corresponds to a loss of about 3-6% of the lithium in the bulk depending on what forms on the surface.

Figure 23 shows lattice parameters for most members of the second subset of the $Li_{1+x}V_{1-x}O_2$ series from XRD patterns taken at regular intervals following synthesis to see if the structure changed over time. There is significant drift in these parameters which is on the order of the differences between adjacent compositions.

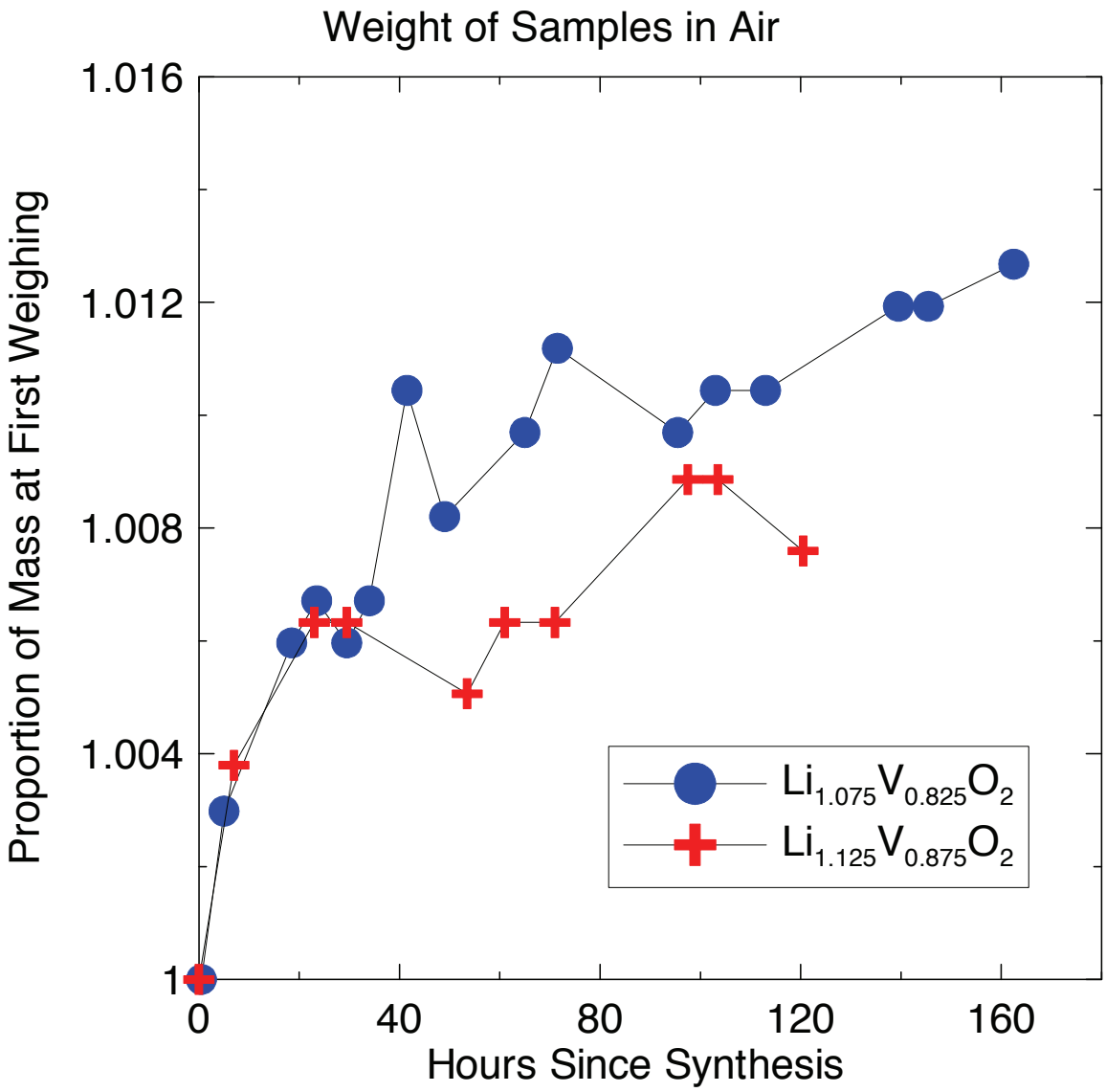

Figure 22
Change in weight of two $Li_{1+x}V_{1-x}O_2$ samples left in open air. High lithium mobility and reactivity in the layered structure allows for small amount of bulk delithiation to form Li_2O, LiOH or Li_2CO_3.

In $LiVO_2$, a loss of lithium results in a reduction of trimers. This means that the integrated intensity of the superlattice peak could vary quite rapidly with time. It is possible that this variation is systematic with x in the $Li_{1+x}V_{1-x}O_2$ series which may explain why peak area was greatest for x = 0.04 in Figure 21.

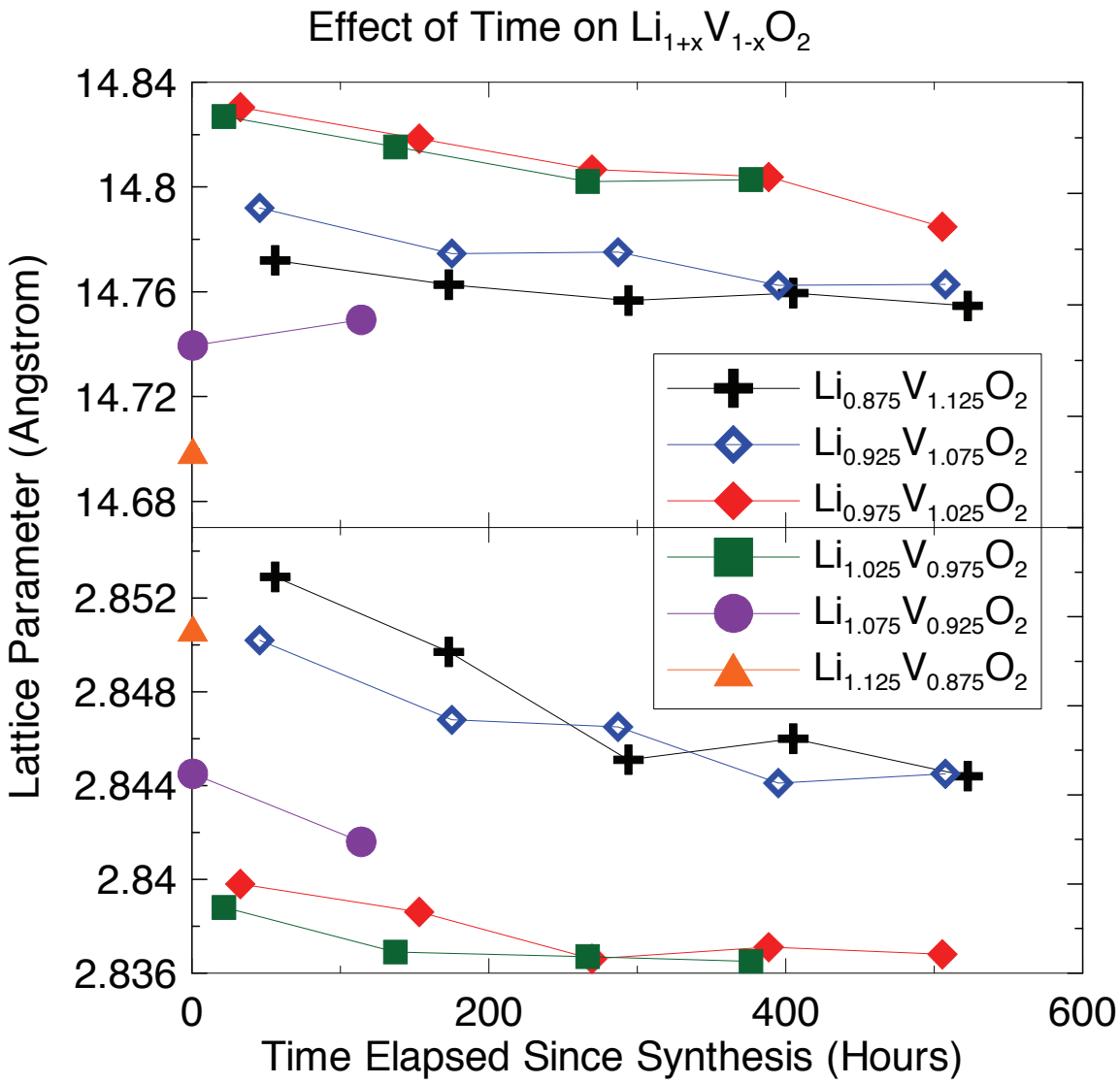

Figure 23
Repeated XRD analysis showed a tendency of the lattice parameters of $Li_{1+x}V_{1-x}O_2$ to drift over time. The "c" lattice parameter is shown on top, the "a" parameter on bottom.

A rigorous time observation study was not conducted on the superlattice structure. However the elapsed time between synthesis and measurement of the superlattice peak was recorded and this data was used to try to elucidate some of the variability in the data in Figure 21. Furthermore, the superlattice peak of one sample of the stoichiometric

composition $LiVO_2$ was measured at two different periods of time. Figure 24 shows both these plots.

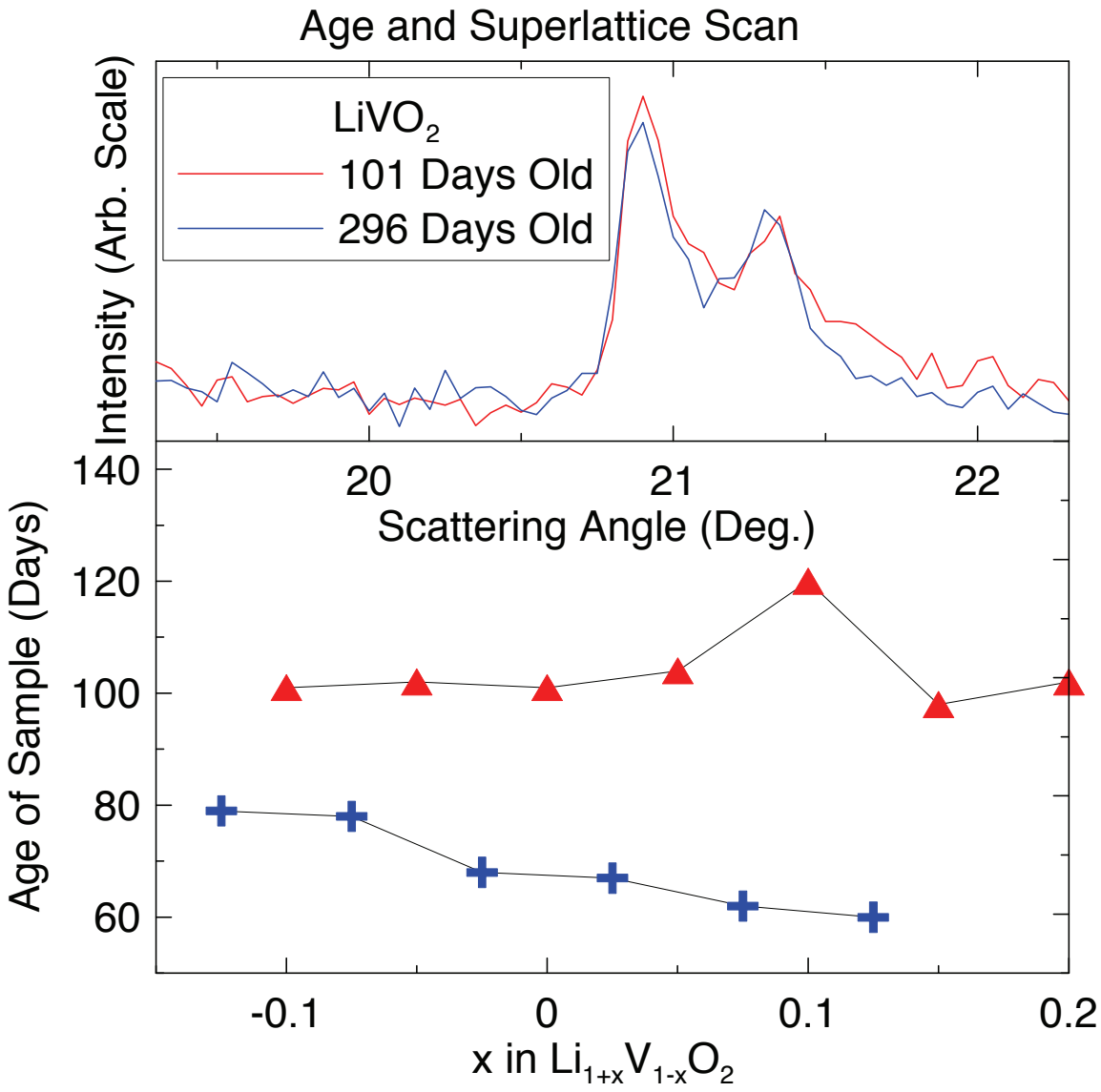

Figure 24
Two superlattice patterns of one $LiVO_2$ sample taken at different times are shown in the top panel. There is little difference between them but it is possible that after 100 days the relevant change has already occurred. The bottom panel shows the amount of time elapsed between synthesis and measurement of the original (crosses) and later subset (triangles).

The data show that there was no change of the superlattice peak between 100 and 300 days after synthesis. This allows the conclusion that it has reached steady state after 100 days but unfortunately does not say anything about what could occur during the first 100. The second panel shows that this condition should apply to the original subset at the time where superlattice patterns were collected. The later samples were an average of about a month younger when the superlattice was investigated so it is possible that they were experiencing delithiation at this time. Since there were no superlattice XRD patterns taken directly after synthesis it is ultimately difficult to draw conclusion about the effect of time on the superlattice peak.

To investigate the effect on $Li_{1+x}V_{1-x}O_2$ of immersion in water two identical samples of $Li_{1.1}V_{0.9}O_2$ were synthesized. The test sample was placed in distilled water for three days whereupon it was filtered out and dried. The control sample was simply left exposed to air for this time. Figure 25 shows the XRD patterns of both samples before and after treatment. The data points of the initial XRD pattern are shown as crosses. The points of the pattern taken after water or air treatment are shown as a connected line. The inset in the upper panel shows an expanded view of the 003 peaks of the sample that was exposed to water.

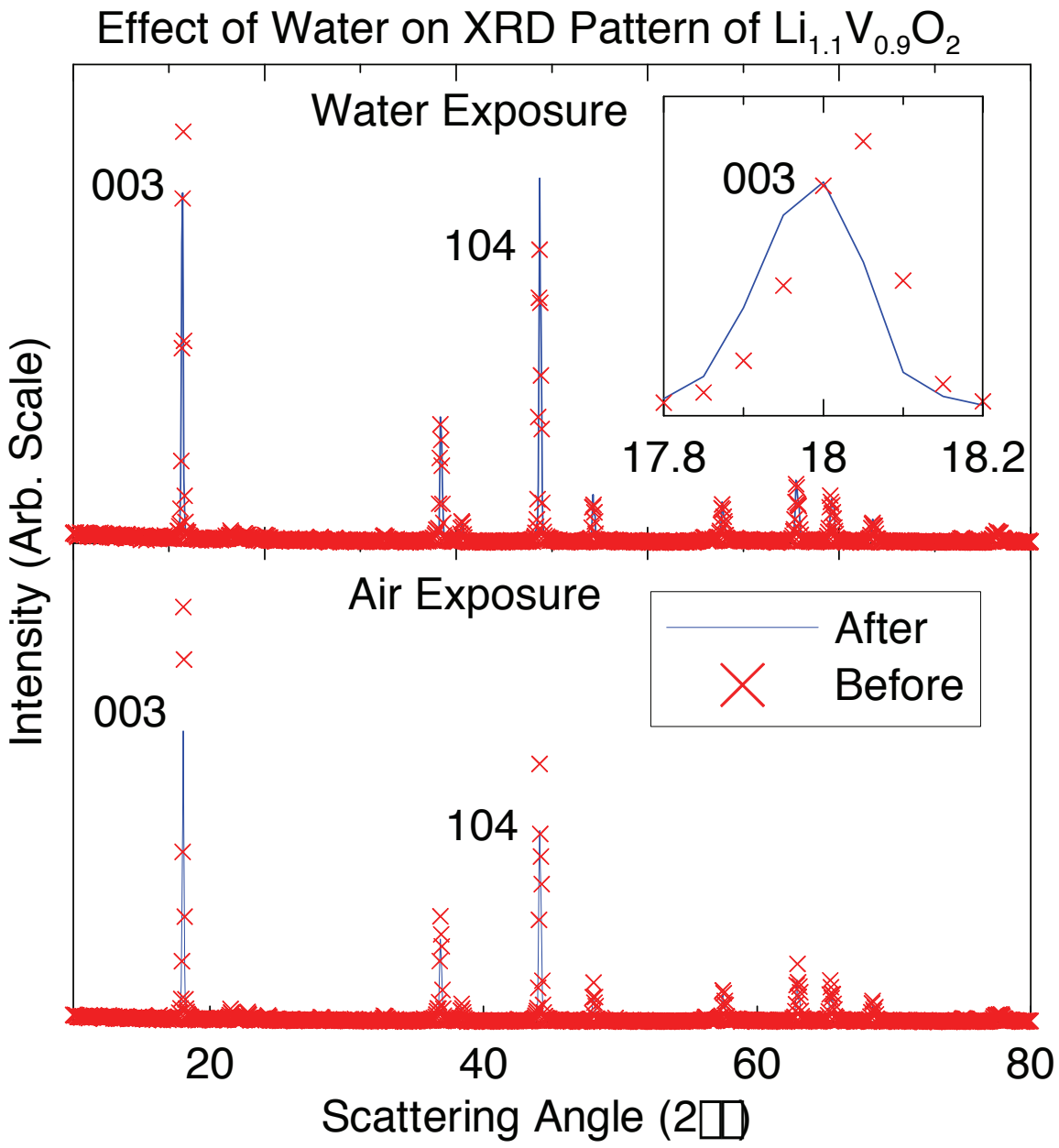

Figure 25
The XRD patterns of samples of $Li_{1.1}V_{0.9}O_2$ exposed to water (top) and air (bottom). Patterns from before exposure are shown as crosses, those from after as solid lines. Inset shows an expanded view of the 003 peak of the water exposed sample before and after exposure.

The sample which was exposed to air showed no change between the two scans. The later scan had lower intensity but this seem to be equally true of all peaks. The sample exposed to water showed visible change. The 003 peak became less intense while the 104 peak

gained intensity. This may be indicative of cationic diorder due to invasion of the Li-layer by V cations. Attempts to perform Rietveld refinement failed for all patterns, yet the inset demonstrates that the peaks are well represented and one is unambiguously larger.

ELECTROCHEMICAL PROPERTIES OF $Li_{1+x}V_{1-x}O_2$

Negative electrodes were made of the $Li_{1+x}V_{1-x}O_2$ series using a recipe of 80/12/8 weight percent active material, Super-S carbon black and lithium polyacrylic acid (Li-PAA) binder. These were mixed using water as a solvent then spread in a layer 0.0015" thick on abraded copper foil before drying. Figures 26 through 28 show the electrochemical properties of the resulting coin cells. Figure 26 shows the charge/discharge curves for $Li/Li_{1+x}V_{1-x}O_2$ cells with x = -0.10, -0.05, 0.00, 0.05, 0.10, 0.15 and 0.20.

These results are very different from those seen in Figures 12-15. There is no low voltage plateau associated with the conversion from $R\bar{3}m$ to 1T. Instead, the sloping region is greatly extended showing a large degree of both reversible and irreversible capacity. These both increase with x from x = -0.10, which has an initial discharge capacity of about 150 mAh/g and a reversible capacity between 50 and 75 mAh/g, to x = 0.20 with an initial discharge of 350 mAh/g and a reversible capacity of almost 200 mAh/g. There is a sharp jump in capacity as the composition passes from $x < 0$ to $x > 0$. From this point on the capacity seems to increase smoothly. There is an appreciable tendency for the curves to drift toward higher capacity with each cycle. The exception to this rule is $Li_{1.1}V_{0.9}O_2$ which does not pass the value of about 375 mAh/g although irreversible capacity is seen in each cycle as the charge curve gets shorter.

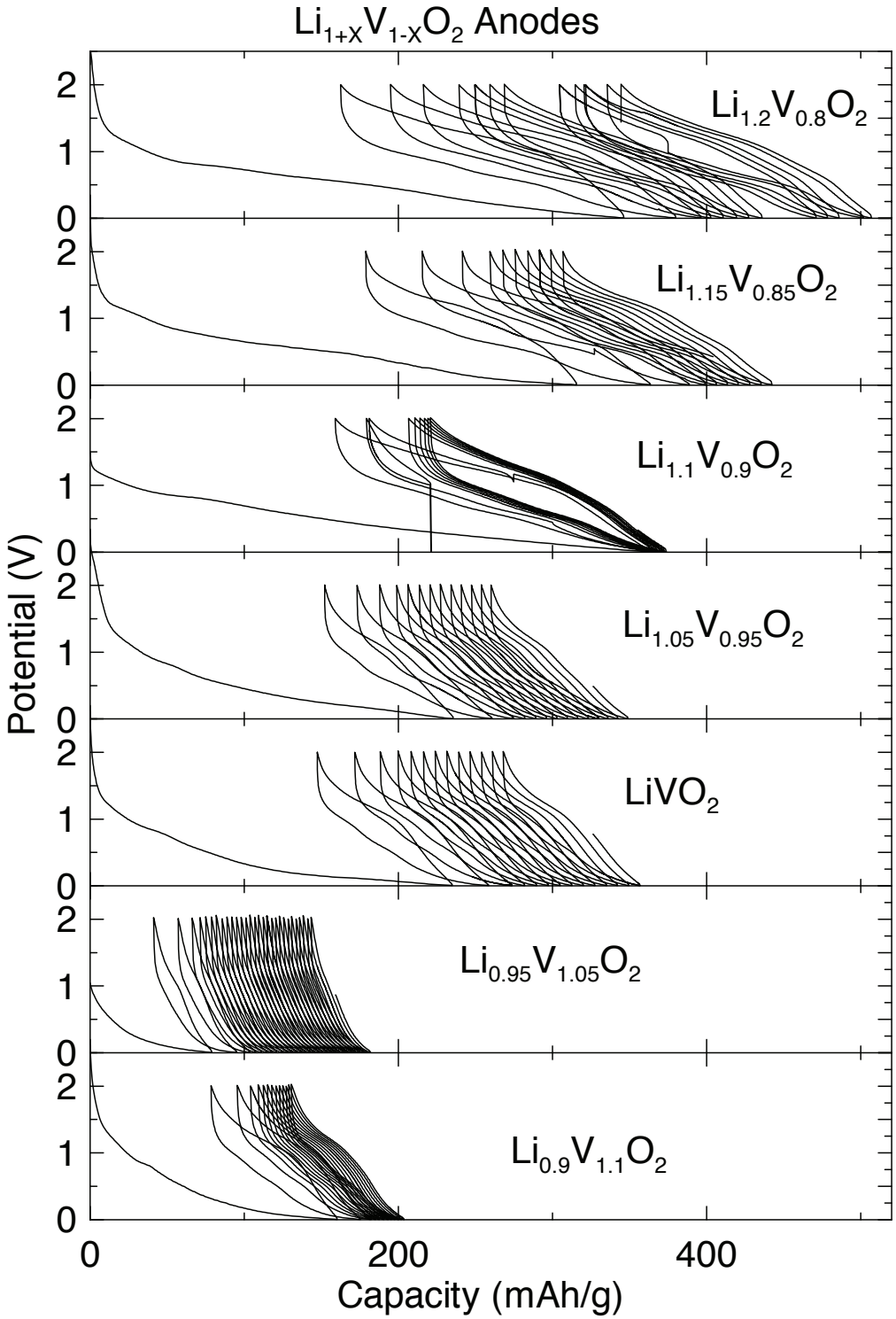

Figure 26

These cells were made from $Li_{1+x}V_{1-x}O_2$ using a recipe of 80/8/12 (weight percent) of active material, Li-PAA binder and Super-S carbon black. The sloping region is elongated relative to results seen in the literature and there is a conspicuous lack of a low voltage plateau.

Figure 27 shows the charge and discharge capacities for about ten cycles of the $Li_{1+x}V_{1-x}O_2$ series. After five cycles the capacity has largely leveled out and seems to increase with x.

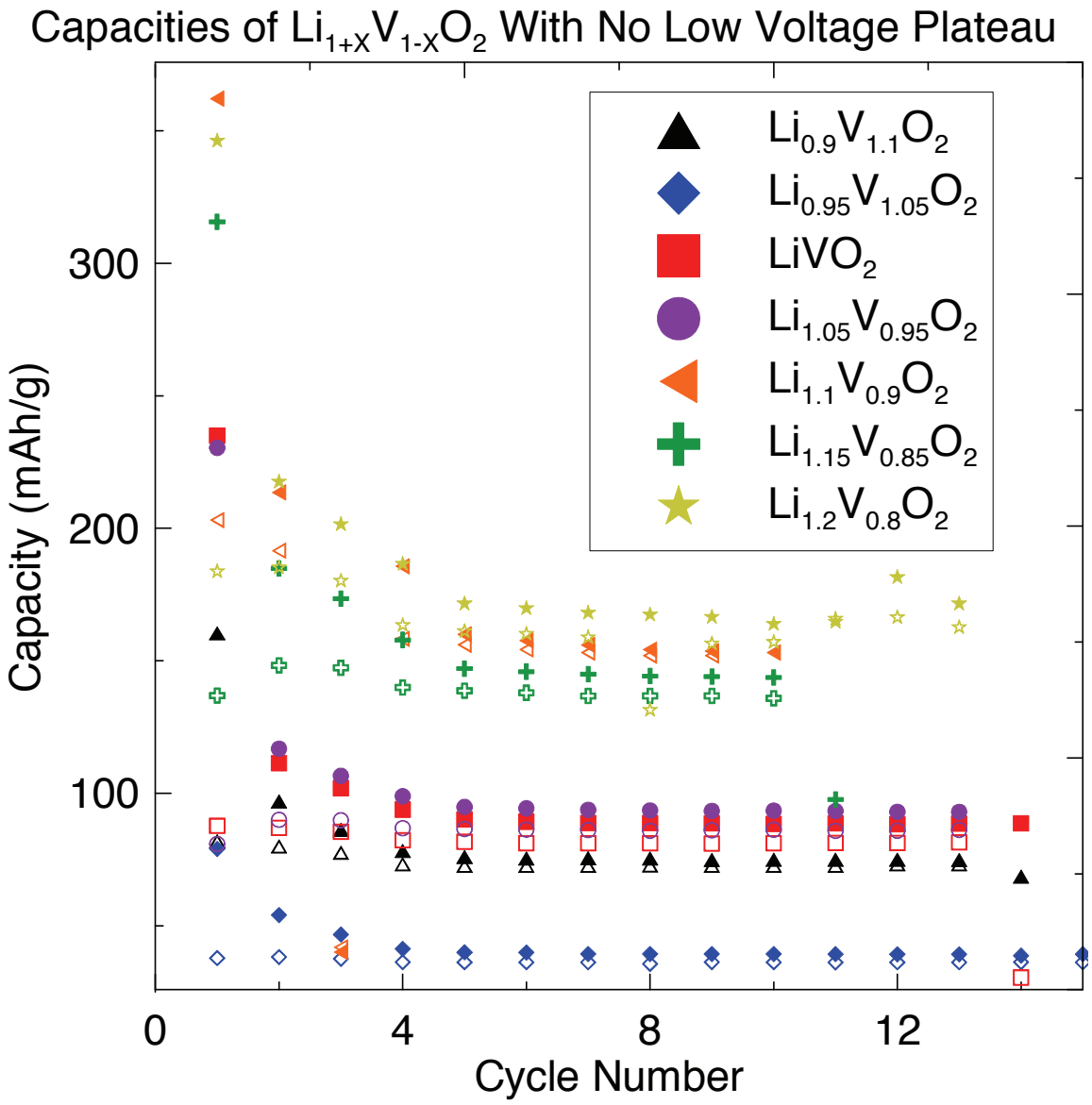

Figure 27
Capacity and cycling performance of $Li_{1+x}V_{1-x}O_2$ anodes made with Li-PAA. Solid shapes denote discharge (Li inserted into layered material), hollow ones denote charge. Capacity seems to increase with x across the entire composition range.

Figure 28 shows the discharge capacity of the ninth cycle plotted against x. This data showed a linear trend and regression quantified the relationship between reversible capacity and x as capacity = 368.85 x + 82.672 mAh/g.

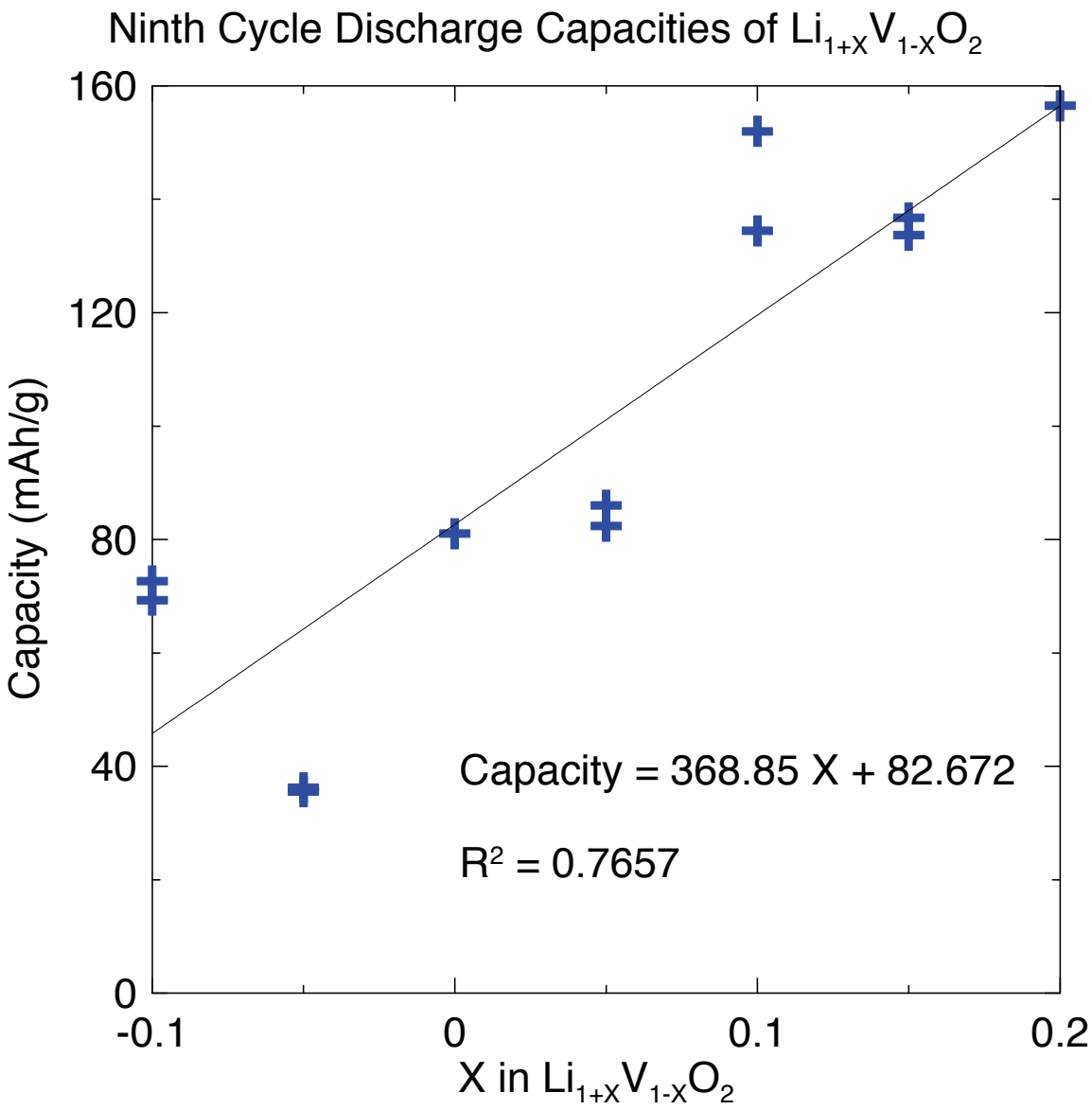

Figure 28
Relationship between x and capacity of the ninth discharge in $Li_{1+x}V_{1-x}O_2$.

Reference [3] describes how $x > 0$ is a necessary condition for 1T phase formation upon Li intercalation. Li in the V layer makes Li-layer tetrahedral sites (see Figure 9) accessible and their occupation during the first stages of intercalation helps the structure shear to the 1T phase. Calculations (reference [3]) predict a potential of 0.58V for intercalation into tetrahedral sites. The majority of the capacity in the $Li_{1+x}V_{1-x}O_2$ results of the present study occurs between 0.5 and 1.5 V. It may be the case that tetrahedral site occupation accounts for this capacity. This would beg the question of what prevents the shearing to the 1T structure in these samples.

Later samples of $Li_{1.1}V_{0.9}O_2$ were used to create coin cells using polyvinyldiene fluoride (PVDF) as an electrode binder. Figure 29 shows a comparison of cells made using the two binders.

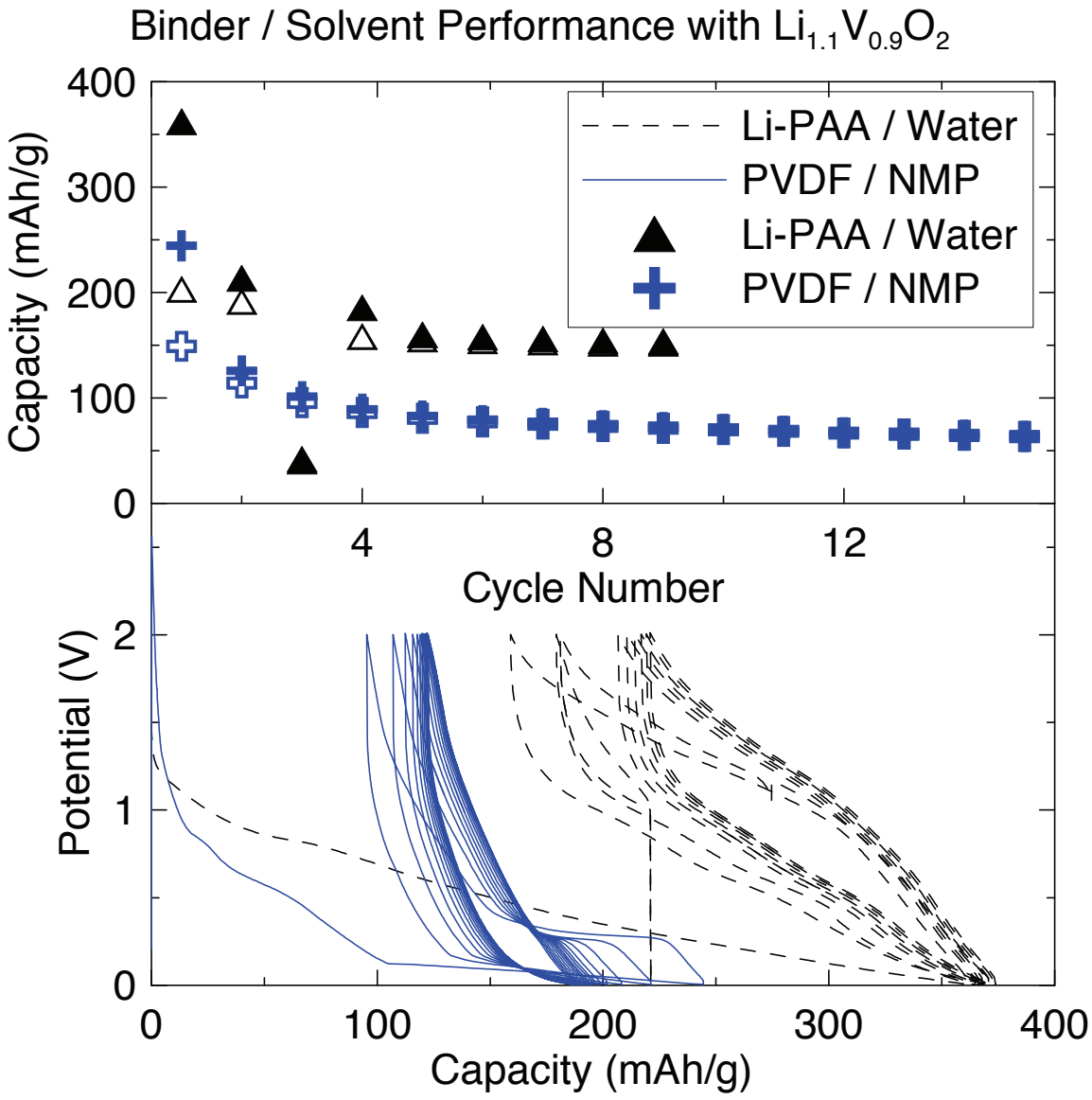

Figure 29
Negative electrodes made with two samples of the same composition, $Li_{1.1}V_{0.9}O_2$, and different choices of binder and solvent. The choice of PVDF leads to results similar to literature results but with smaller reversable capacity. Solid/hollow symbols are discharge/charge capacity.

The behaviour of cells made with PVDF is reminiscent of those seen in Figure 10. The one shown in Figure 29 has a low voltage plateau but exhibits lower initial capacity and lower reversible capacity than that made with Li-PAA. Li-PAA uses water as a solvent and this can be expected to affect the active material it self. According to reference [42]

$LiVO_2$ which has been exposed to air for several days and then immersed in water can lose up to 0.2 Li. The fact that the Li-PAA anode is immersed in water, spread into a thin layer (thus giving it more air exposure) and subjected to moderately high temperature (≈100°C in electrode oven) makes it reasonable to expect that there is some delithiation. If the higher temperature and greater surface area can increase this proportion to 0.33 there could be cationic disorder as this was shown to be the value for which the migration of V into the Li-layer to create cationic disorder commences [37]. It is believed [3] that if V is present in the Li-layer, it can cause a pinning of the anion sheets to prevent the shear associated with the transition to 1T phase. This was not realized until long after the fact and caused great difficulty during attempts to reproduce the results of others. The comparison of the two negative electrode characteristics shown in Figure 27 is reminiscent of the positive electrodes whose behaviour is seen in Figure 10. In both cases a near stoichiometric sample of $Li_{1+x}V_{1-x}O_2$ exhibits a long flat plateau while a potentially disordered sample displays a larger reversible capacity over a broader voltage range.

Figure 30 shows a comparison of the electrochemical behaviour of the two samples of $Li_{1.1}V_{0.9}O_2$ used for the water exposure study and one of $LiVO_2$ that was not exposed to water. These cells were prepared in the same manner and with the same recipe as those using PVDF binder discussed above.

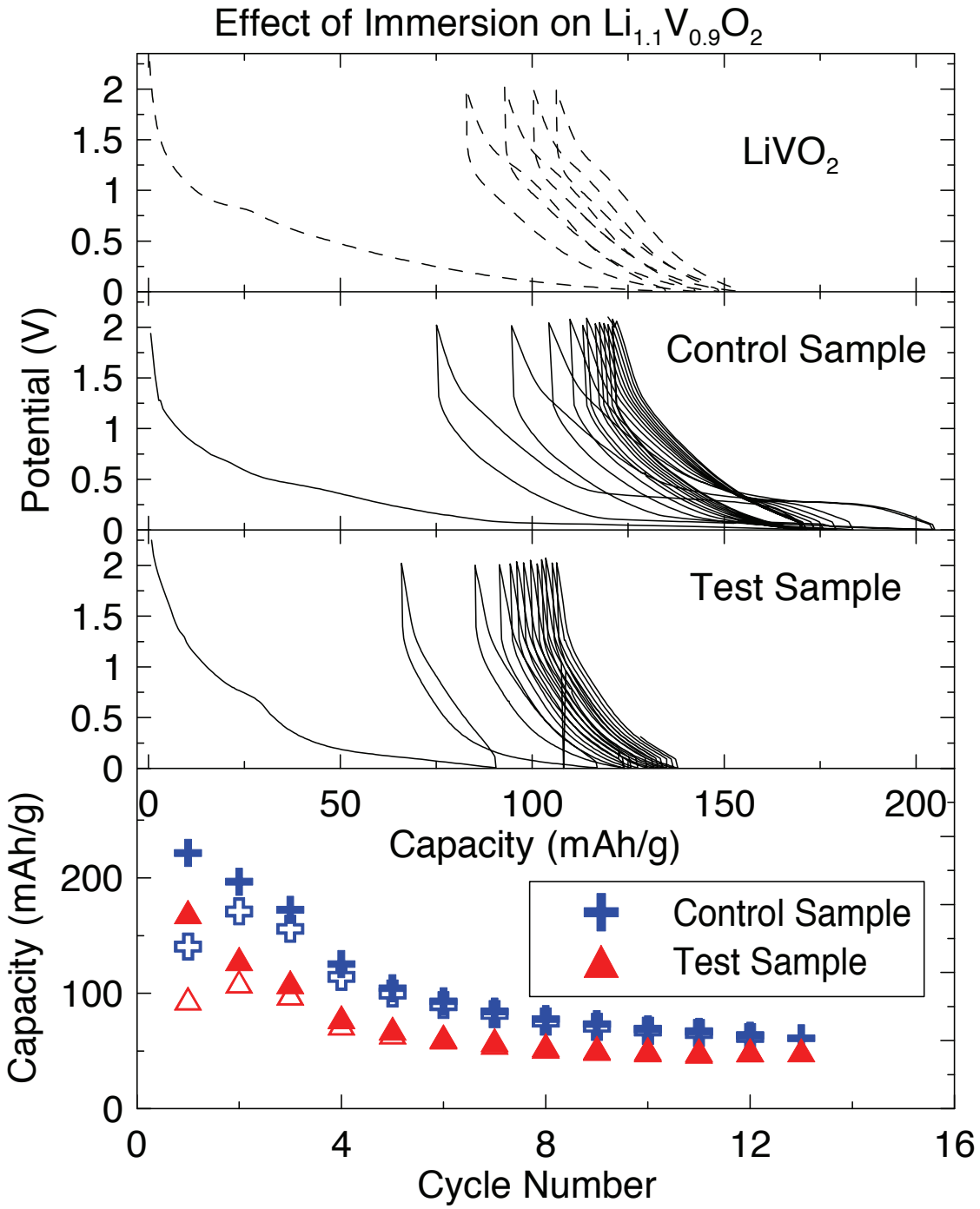

Figure 30
Electrochemical cycling curves and capacities of two $Li_{1.1}V_{0.9}O_2$ samples from the water exposure study. The sample that was immersed in water shows lower capacity in the cycling curves and lacks the low voltage plateau. The capacity in the sloping region decreases on every cycle. Both seem to be converging to the same value but the control sample has the low voltage plateau and larger capacity for all cycles. Electrochemical curves of the $LiVO_2$ cell made with PVDF have been added for comparison.

The sample exposed to water clearly lacks the low voltage plateau associated with conversion to the 1T phase. Both samples were synthesized with 0.9 V in the vanadium layer so it is unlikely that the tetrahedral site occupation that is claimed [3] to trigger the phase change becomes unfeasible during immersion. The XRD patterns shown in Figure 25, though inconclusive, suggest cationic disorder and this is a likely inhibitor of the shearing of the crystal planes. The behaviour displayed in Figure 30 differs greatly from that in Figure 26 where the reversible capacity of about 100 mAh/g between 0.5 V and 1.5 V is believed to be due to tetrahedral site occupation. It did bear remarkable resemblance to the $LiVO_2$ sample shown in the top panel. There is now a question of why the water treated sample did not intercalate Li into the tetrahedral sites (as we suspect happened in Figure 26). There are several possible differences between the samples in Figure 26 and Figure 30. Filtering of the water treated sample preserved larger particles preferentially while discarding smaller ones. Electrodes prepared with Li-PAA and water were spread thinner than those with PVDF causing more of the bulk to be within reach of the surface. These electrodes were dried in an oven at $\approx 100°C$ while containing water. They were also left in air for a number of days after drying before cells were assembled. The sample treated in water experienced this at room temperature then went into the oven with NMP, not water before heading immediately to the glovebox. At the same time, it must be noted that NMP is not anhydrous and may contain a certain amount of water. This quantity was not determined so the contrast between cells prepared using NMP and those using Li-PAA may not be a perfect representation of the effect of water exposure.

$\underline{Li_{1.1}Mo_xV_{0.9-x}O_2}$

The variety of electrochemical behaviour seen in Figures 12-15 led to the decision to create the $Li_{1.1}Mo_xV_{0.9-x}O_2$ series. These samples were created using solid state synthesis with powdered Li_2CO_3, V_2O_3 and MoO_3 for values of x = 0.01, 0.03 and 0.05. Figure 31 shows an expanded view of the low intensity region of the XRD patterns of $Li_{1.1}V_{0.9}O_2$ and $Li_{1.1}Mo_{0.05}V_{0.85}O_2$ overlaid with an offset for easier viewing.

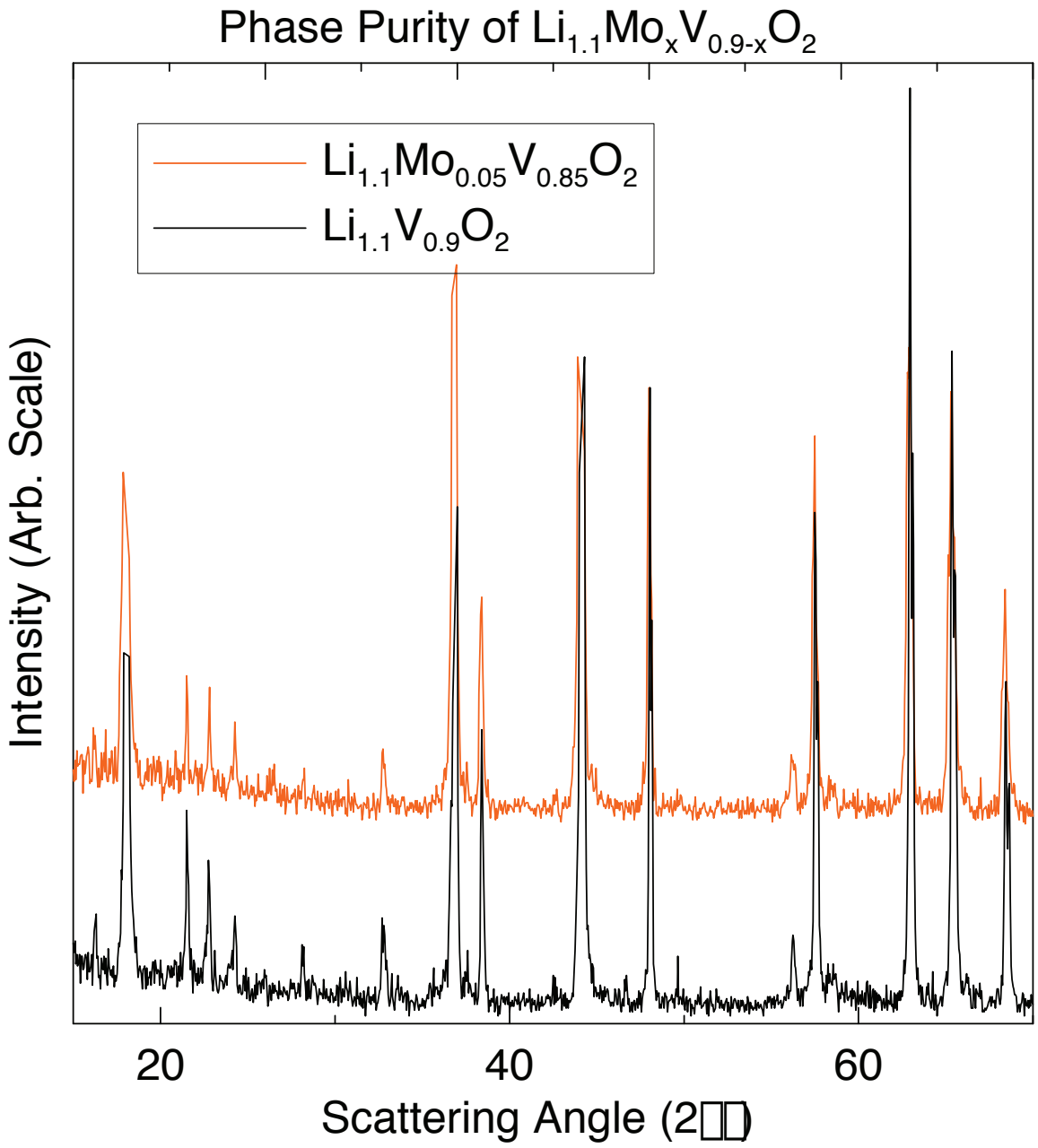

Figure 31
XRD patterns of Mo doped sample $Li_{1.1}Mo_{0.05}V_{0.9}O_2$ and $Li_{1.1}V_{0.9}O_2$ expanded near intensity of zero. There is virtually no difference between them, suggesting that Mo does not react with $LiVO_2$.

The samples are very similar with the only apparent impurity peaks being those of Li_3VO_4. MoO_3 is not observed with the other components. Figure 32 shows how the lattice parameters do not increase with x. Composition dependence of the lattice

parameters is expected as the Mo^{3+} ion has a larger radius than the V^{3+} ion suggesting that Mo is not incorporated into the lattice.

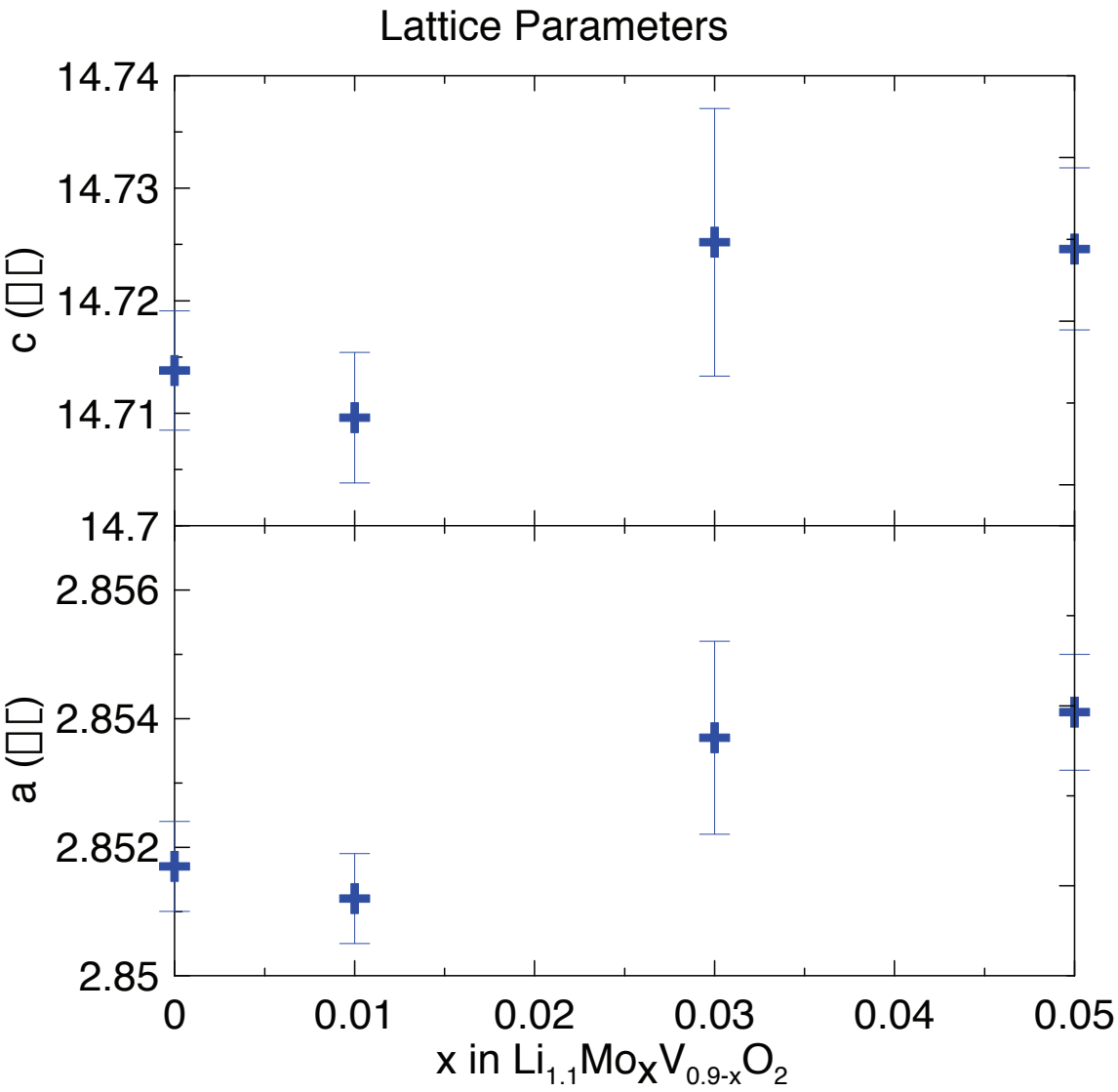

Figure 32
Lattice parameters of $Li_{1.1}Mo_xV_{0.9-x}O_2$ do not show a convincing increasing trend with x, which would be consistent with the substitution of a larger atom.

Figure 33 shows electrochemical data from Li/$Li_{1.1}Mo_xV_{0.9-x}O_2$ cells made using PVDF. These materials were not subject to water or prolonged air exposure. MoO_3 included in synthesis tends to increase both initial discharge capacity and reversible capacity. The

MoO_3 included samples also show a tendency to drift toward higher capacity. Another strange feature is the fact that the sloping region is spread over a higher voltage range.

As an example of what this means $Li_{1.1}V_{0.9}O_2$ has an almost vertical charge curve once it has been recharged to about 1.5V while that of $Li_{1.1}Mo_{0.05}V_{0.85}O_2$ is still very sloped at this point. Figure 34 shows capacity retention is very much improved by even a small amount of Mo and for $x \geq 0.03$ capacity is almost 200 mAh/g.

As MoO_3 is known to melt at 795°C and evaporate at 1155°C under high pressure; at lower pressures it undergoes sublimation between these temperatures [53]. There is no indication of MoO_3 in the XRD data or a trend in the lattice parameter, it is likely that there is no Mo in the prepared samples. Improved electrochemical performance may still be a result of the presence of MoO_3 during synthesis, before it evaporated.

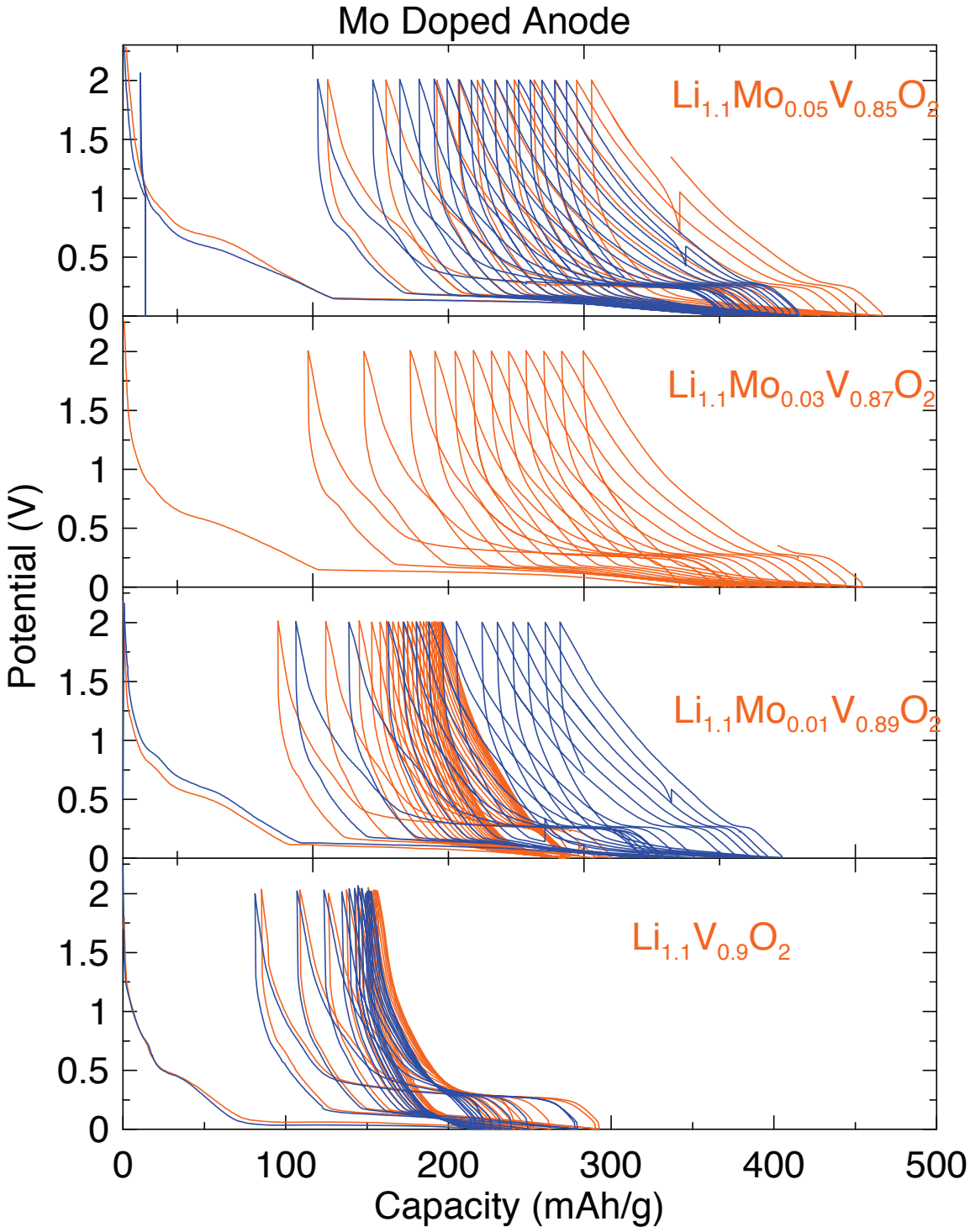

Figure 33
Electrochemical curves of $Li_{1.1}Mo_xV_{0.9-x}O_2$ series of anodes.

.

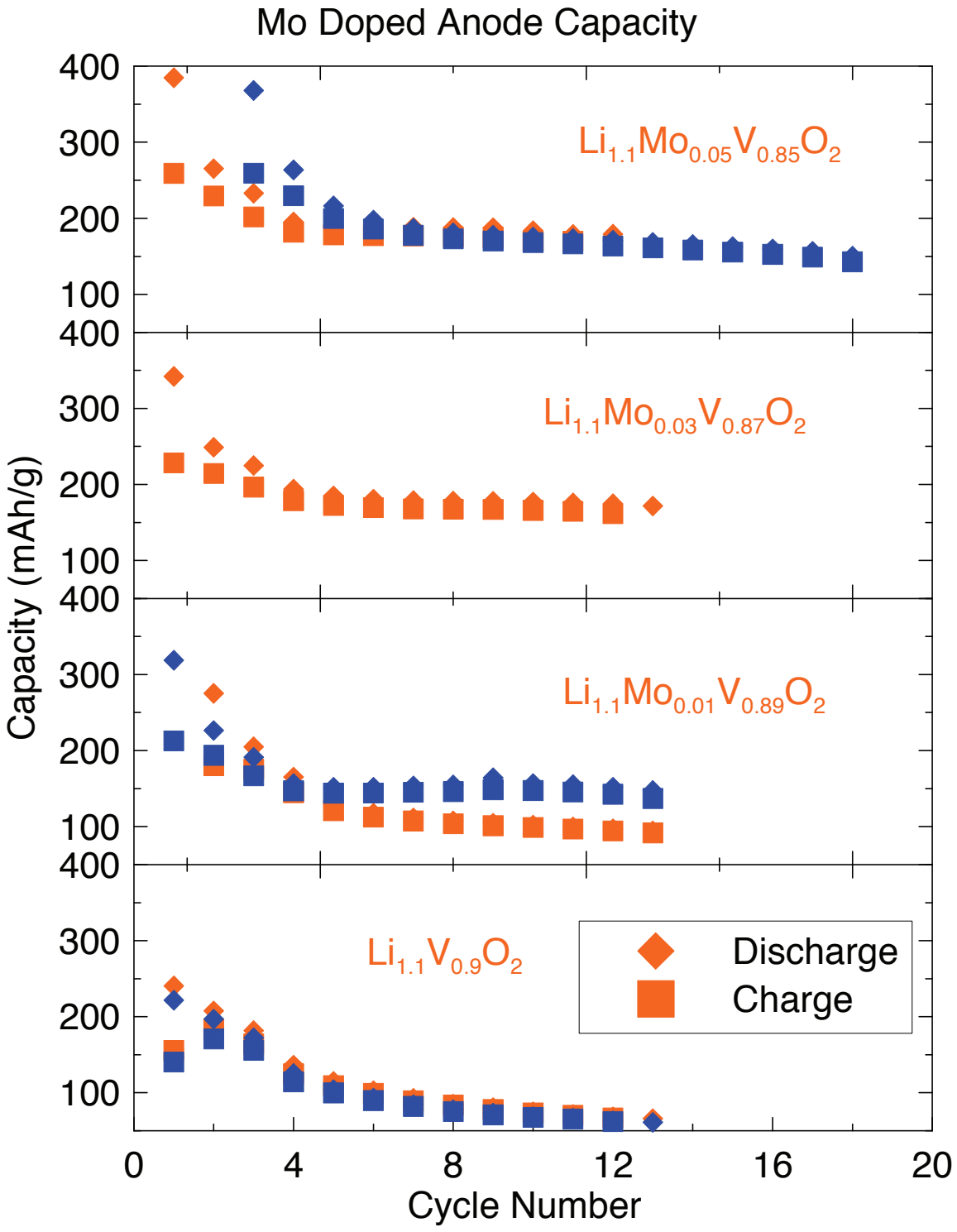

Figure 34
Capacity and cycling performance of $Li_{1.1}Mo_xV_{0.9-x}O_2$ series of anodes.

CHAPTER 5 CONCLUSIONS

SUPERLATTICE STRUCTURE

The dominant theory in the literature regarding the anomaly in structure, magnetic, electrical and thermal properties of $LiVO_2$ seems to be that of orbital ordering. In a triangular layer of V^{3+} cations there are two valence d-electrons at each cation. To avoid magnetic frustration caused by the overlap and antiferromagnetic interaction of these valence electrons it is evident that the orbitals become ordered in their orientation. This happens in such a way that each directs its occupied t_{2g} orbitals toward those of two of its nearest neighbors and toward unoccupied orbitals of all other nearest neighbors. These two neighbors reciprocate to form quasi-isolated triangles of magnetically interacting vanadium cations. These "trimers" cause the constituent cations to be displaced toward the centre of the formation. This displacement is periodic throughout the whole crystal (Figure 8).

The 3+ state is essential in this mechanism as a valence shell that has more or fewer d-electrons will not be able to orient itself in a way that causes this large degree of overlap with its trimer partners and small degree of overlap with others. Replacing V with another element, such as Li, in this layer will also decrease trimer formation in its own right as well as change the oxidation state of the vanadium cations (Figure 18).

Since the displacement is periodic, the resulting spacing between ions in the crystalline solid should diffract x-rays resulting in a peak in the XRD pattern corresponding to the

spacing of the superlattice. This was observed several times in the literature. In particular, the integrated intensity of this peak was plotted as a function of temperature which showed that trimer formation was disrupted upon passing through the transition temperature of the anomalies in lattice parameter, conductivity and paramagnetic susceptibility.

The lattice parameters of the $LiCr_yV_{1-y}O_2$ system for temperatures above and below the transition temperature converged to similar values as y increased to about 0.3 (Figure 7). For larger values of y both seemed to follow the same linear trend. The value y = 0.3 is the smallest that could result in a complete disruption of superlattice formation.

The present work describes the lattice parameters of $Li_{1+x}V_{1-x}O_2$ and shows for the first time in Figure 17 how they vary as a function of x. This correlates very well with the expected V^{3+} abundance in Figure 18. The superlattice peak patterns displayed in Figure 19 also appear to the eye to fit this trend and this is more rigorously confirmed by fits to the superlattice peak areas in Figure 21.

This data, in conjunction with the reviewed literature, nicely illustrates a causal relationship flowing from composition through oxidation state and valence orbital occupation to the magnetic, thermal and structural properties controlled by orbital ordering. From the point of view of Li ion battery research there is little left to explain regarding orbital ordering in compounds related to $LiVO_2$. If anything, superlattice peak trends will be used as a sensitive indicator of composition, oxidation state or disorder.

ELECTROCHEMICAL BEHAVIOUR AND AIR/WATER EXPOSURE

In the time that this research was conducted, work by other groups fulfilled its original intent. That is, they explained the Li storage mechanism of $LiVO_2$-related negative electrodes. The long, low voltage plateau as seen in Figures 12-15 was shown by ex-situ x-ray diffraction to be caused by a transformation to the 1T Li_2VO_2 phase where Li abandon octahedrally coordinated sites and occupy tetrahedrally coordinated ones, of which there are twice as many (Figure 11). The sloping region which occupies the first 50 to 150 mAh/g of capacity is irreversable and appears to be due to some form of SEI formation.

The fact that 1T Li_2VO_2 forms from $Li_{1.1}V_{0.9}O_2$ but not $LiVO_2$ was cleverly elucidated as being due to the presence of Li in the V layer. This causes a small number of tetrahedral sites of $Li_{1.1}V_{0.9}O_2$ to become accessible and their occupation results in a shearing of the anion sheets to form Li_2VO_2 and allow all tetrahedral sites to be occupied. The efficacy of this mechanism is maximal when 0.07 of the V sites are occupied with Li.

The electrochemical data of $Li/Li_{1+x}V_{1-x}O_2$ cells presented (Figure 26) herein shows a large reversible capacity at a much larger voltage than the transformation to 1T. These cells were made using Li-PAA binder in water. Water has been shown to delithiate and even cause cationic disorder in $LiVO_2$ which can cause pinning to stop the transformation to 1T phase.

The results herein show that $Li_{1+x}V_{1-x}O_2$ is affected by air (Figures 22-24) and that water may result in cationic disorder (Figure 24). Electrochemical data from two $Li_{1.1}V_{0.9}O_2$ samples, one of which was exposed to water, were shown in Figure 30. The water exposed sample of $Li_{1.1}V_{0.9}O_2$ behaved in a manner very similar to $LiVO_2$. The cells made using Li-PAA thus are not simply the result of water exposure of this type. There is work left to be done here.

Changes to the crystal structure of $Li_{1+x}V_{1-x}O_2$ during lithiation and delithiation of the samples shown in Figure 26 may give an indication of the origin of that capacity. In-situ XRD should be performed on one such sample to observe the effect of lithiation on structure.

The lithium insertion process in the material that does not adopt the 1T phase does not require a phase change. The 1T phase change results in a volume expansion of 26%. In the introduction of this work a brief survey of negative electrode materials suggested that there was a tradeoff between cycle life and capacity of materials. If the change in unit cell volume associated with lithium occupation of a large proportion of the tetrahedral sites is much less than the 26% associated with the 1T phase change then it may not be too optimistic to expect that this mechanism will show greater cycle life upon repeated charge and discharge..

Mo SUBSTITUTION

Samples of the $Li_{1.1}Mo_xV_{0.9-x}O_2$ series were attempted for x = 0.01, 0.03 and 0.05. MoO_3 included during synthesis increased both initial and reversible capacity up to a point as seen in Figures 33 and 34. There was little difference between 0.03 and 0.05. XRD patterns did not show an increase of lattice parameter with x (Figure 32) that would indicate Mo was being incorporated in $Li_{1.1}V_{0.9}O_2$, but there were no diffraction peaks visible (Figure 31) which could not be accounted for by $LiVO_2$. It would be best to repeat the scan with a longer count time of 30 to 50 seconds, though it is likely that the MoO_3 evaporated.

Figures 12 through 14 suggest that synthesizing $Li_{1.1}V_{0.9}O_2$ in the presence of another transition metal oxide can have a profound effect upon the performance of the electrode, particularly with regard to the sloping region of the curve. The middle panel in Figure 14 shows that this is largely reversible, in contrast to the conclusion that the sloping region of $Li_{1.1}V_{0.9}O_2$ is due to SEI formation.

REFERENCES

[1] J. T. Vaughey, A. M. Geyer, N. Fackler, C. S. Johnson, K. Edstrom, H. Bryngelsson, R. Benedek and M. M. Thackeray, J. Power Sources **174**, pp. 1052-1056 (2007).

[2] K. Momma and F. Izumi, "VESTA: a three-dimensional visualization system for electronic and structural analysis." J. Appl. Crystallogr., 41:653-658, 2008.

[3] A. R. Armstrong, C. Lyness, P. Panchmatia, M. S. Islam and P. G. Bruce, Awaiting Publication.

[4] J. R. Dahn and G. M. Ehrlich, Handbook of Batteries 4e, T. B. Reddy, Editor, McGraw Hill, New York, 2011. 26.17-26.25.

[5] N-S. Choi, J-S. Kim, R-Z. Yin and S-S. Kim, Mat. Chem. Phys. **116**, pp. 603-606 (2009).

[6] P. P. Ferguson, PhD dissertation. Dalhousie University, Halifax, Canada, 2009.

[7] Y. Tian, M.Sc. dissertation. Dalhousie University, Halifax, Canada, (2008).

[8] C. T. Lynch, Editor, CRC Handbook of Materials Science Vol. 1. CRC Press, Cleveland Ohio, 1974. 62.

[9] M. N. Obrovac and L. J. Krause, J. Electrochem. Soc. **154**, A103-A108 (2007).

[10] M. A. Al-Maghrabi, N. van der Bosch, R. J. Sanderson, D. A. Stevens, R. A. Dunlap and J. R. Dahn, Awaiting Publication.

[11] S. Xun, X. Song, H. Zheng, V. S. Battaglia, G. Liu, N. Vukmirovic, Awaiting publication.

[12] K. M. Colbow, M.Sc. dissertation. University of British Columbia, Vancouver, Canada, (1988).

[13] M. Imazaki, K. Ariyoshi and T. Ohzuku, J. Electrochem. Soc. **156**, A780-A786 (2009).

[14] J. B. Goodenough and Y. Kim, Chem. Mat. **22**, 587-603 (2009).

[15] T. Zheng, J. N. Reimers and J. R. Dahn, Phys. Rev. B **51**, 734-741 (1995).

[16] Sung-Soo Kim, Kyou-Yoon Sheem, Sang-Min Lee, Sang-Jin Kim, Joon-Sup Kim, Bok-Hwan Jung and Goo-Jin Jeong, European Patent Application Publication EP 1 511 101 A2, March 02 2005.

[17] K. Kobayashi, K. Kosuge and S. Kachi, Mat. Res. Bull. **4**, 95-106 (1969).

[18] T. A. Hewston and B. L. Chamberland, J. Solid State Chem. **59**, 168-173 (1985).

[19] T. A. Hewston and B. L. Chamberland, J. Solid State Chem. **65**, 100-110 (1986).

[20] L. P. Cardoso, D. E. Cox, T. A. Hewston and B. L. Chamberland, J. Solid State Chem. **72**, 234-243 (1988).

[21] T. A. Hewston and B. L. Chamberland, J. Phys. Chem. Solids **48**, 97-108 (1987).

[22] H. Takei, M. Koike, K. Imai, H. Sawa, H. Kadowaki, Y. Iye, Mat. Res. Bull. **27**, 555-562 (1992).

[23] F. Du, A. Li, D. Liu, S. Zhan, F. Hu, C. Wang, Y. Chen, S. Feng, G. Chen, J. Mag. Mag. Mat. **321**, 1975-1979 (2009).

[24] W. Tian, M. F. Chisholm, P. G. Khalifah, R. Jin, B. C. Sales, S. E. Nagler, D. Mandrus, Mat. Res. Bull. **39,** 1319-1328 (2004).

[25] J. B. Goodenough, Phys. Rev. **117**, 1442-1451 (1960).

[26] J. B. Goodenough, Magnetism and the Chemical Bond. Interscience and John Wiley, New York, NY. 1963. p. 270.

[27] J. B. Goodenough, G. Dutta, A. Manthiram, Phys. Rev. B **43**, 10170-10178 (1991).

[28] J. Kikuchi, S. Kambe, H. Yasuoka, Y. Ueda, K. Tomimoto and J. Akimitsu, J. Phys. Soc. Jpn. **60**, 3620-3624 (1991).

[29] M. Onada, T. Naka and H. Nagasawa, J. Phys. Soc. Jpn. **60**, 2550-2553 (1991).

[30] M. Onada and T. Inabe, J. Phys. Soc. Jpn. **62**, 2216-2219 (1993).

[31] R. A. Dunlap, The Physics of Nuclei and Particles. Thomson Brooks/Cole, Belmont, CA. 2004. 67-70.

[32] K. Imai, H. Sawa, M. Koike, M. Hasegawa and H. Takei, J. Solid State Chem. **114**, 184-189 (1995).

[33] W. Tian, M. B. Stone, D. G. Mandrus, B. C. Sales, R. Jin, D. T. Adroja and S. E. Nagler, Physica B **385-386**, 50-52 (2006).

[34] T. Naka, M. Onada and H. Nagasawa, Solid State Comm. **87**, 679-683 (1993).

[35] H. F. Pen, J. van den Brink, D. I. Khomskii and G. A. Sawatzky, Phys. Rev. Lett. **78**, 1323-1326 (1997).

[36] H. F. Pen, L. H. Tjeng, E. Pellegrin, F. M. F. de Groot and G. A. Sawatzky, Phys. Rev. B **55**, 15500-15505 (1997).

[37] L. A. de Picciotto, M. M. Thackeray, W. I. F. David, P. G. Bruce and J. B. Goodenough, Mat. Res. Bull. **19**, 1497-1506 (1984).

[38] L. A. de Picciotto and M. M. Thackeray, Mat. Res. Bull. **20**, 187-195 (1985).

[39] L. A. de Picciotto and M. M. Thackeray, Solid State Ionics **18&19**, 773-777 (1986).

[40] M. M. Thackeray, L. A. Picciotto, W. I. F. David, P. G. Bruce and J. B. Goodenough, J. Solid State Chem. **67**, 285-290 (1987).

[41] L. A. de Picciotto, M. M. Thackeray and G. Pistoia, Solid State Ionics, **28-30**, 1364-1370 (1988).

[42] A. Manthiram and J. B. Goodenough, Can. J. Phys. **65**, 1309-1317 (1987).

[43] K. Ozawa, L. Wang, H. Fujii, M. Eguchi, M. Hase and H. Yamaguchi, JES **153**, A117-A121 (2006).

[44] K. Ozawa, Y. Nakao, L. Wang, Z. Cheng, H. Fujii, M. Hase and M. Eguchi, J. Power Sources, **174**, 469-472 (2007).

[45] J. R. Dahn, U. von Sacken and C. A. Michal, Solid State Ionics **44**, 87-97 (1990).

[46] I. Davidson, J. E. Greedan, U. von Sacken, C. A. Michal and J. R. Dahn, Solid State Ionics **46**, 243-247 (1991).

[47] S. Kang, S. Park, C. S. Johnson and K. Amine, J. Electrochem. Soc. **154**, A268-A274 (2007).

[48] J. Barker, M. Y. Saidi and J. L. Swoyer, J. Electrochem. Soc. **150**, A1267-A1272 (2003).

[49] M. Wojdyr, J. Appl. Cryst. 43, 1126-1128 (2010).

[50] T. Marks, S. Trussler, A. J. Smith, D. Xiong and J. R. Dahn, J. Electrochem. Soc. **158**, A51-A57 (2011).

[51] J-P. Payan, D. Beydon, J-P Fabry, I. Boudry, B. Cossec and E. Ferrari, Drug Metab. Dispos. **30**, 1418-1424 (2002).

[52] A. M. Wilson and J. R. Dahn, J. Electrochem. Soc. **142**, 326-332 (1995).

[53] R. C. Weast, editor in chief, CRC Handbook of Chemistry and Physics 70th edition. CRC Press, Inc. Boca Raton, Florida. 1989.